UNIVERSITY OF CALIFORNIA, SAN DIEGO

Microfabricated platforms for the characterization of single and collective cell migration mechanics

A dissertation submitted in partial satisfaction of the
requirements for the degree
Doctor of Philosophy

in

Engineering Sciences with a Specialization in Multi-Scale Biology

by

Ernesto Criado-Hidalgo

Committee in charge:

Professor Juan Carlos del Álamo, Chair
Professor Juan C. Lasheras, Co-Chair
Professor Elena Koslover
Professor David Saintillan
Professor Yingxiao Wang

2020

The dissertation of Ernesto Criado-Hidalgo is approved, and it is acceptable in quality and form for publication on microfilm or electronically:

_____

_____

_____

_____
Co-Chair

_____
Chair

University of California, San Diego

2020

EPIGRAPH

Estos dias azules,

y este sol de la infancia...

— Antonio Machado

TABLE OF CONTENTS

Signature Page . . . iii

Epigraph . . . iv

Table of Contents . . . v

List of Figures . . . vii

List of Tables . . . ix

Acknowledgements . . . x

Vita . . . xiii

Abstract of the Dissertation . . . xv

Chapter 1 Introduction . . . 1

Chapter 2 Collective Cell Migration of Epithelial Monolayers in the Presence of Obstacles . . . 3

2.1 Introduction . . . 3

2.2 Materials and Methods . . . 5

2.2.1 Cell culture . . . 5

2.2.2 PolyAcrylamide Gels Preparation . . . 6

2.2.3 Microfabrication of bicompatible slender elastic micro-rods . . . 8

2.2.4 Fabrication of PDMS stencils . . . 11

2.2.5 Microscopy and Imaging . . . 14

2.2.6 Immunofluorescence microscopy . . . 15

2.2.7 Image Processing . . . 16

2.3 Results . . . 17

2.3.1 Mechanical phenotyping of epithelial cell lines . . . 21

2.3.2 Epithelial monolayers are able to climb obstacles through integrin adhesion with preserved front-rear polarity . . . 28

2.3.3 Epithelial monolayers maintain tissue integrity in three dimensional environments . . . 28

2.3.4 Piezo1 may regulate Contact Inhibition of Proliferation (CIP) through YAP/TAZ signaling . . . 31

2.4 Discussion and Conclusions . . . 36

2.5 Acknowledgements . . . 40

Chapter 3 Fabricating biocompatible polyacrylamide microbeads for cell-generated mechanical force quantification via photoinitiated polymerization 41
3.1 Introduction 41
3.2 Materials and Methods 43
3.2.1 Microfluidic devices design and fabrication 43
3.2.2 PolyAcrylamide microdroplets generation 46
3.2.3 Planar PolyAcrylamide Gels Fabrication 49
3.2.4 Cell Culture 50
3.2.5 Microscopy and Imaging 52
3.2.6 Image Processing 55
3.2.7 Atomic Force Microscopy quantification of mechanical properties of hydrogels 55
3.3 Results 57
3.3.1 Operation of the flow focusing microfluidic device and generation of pre-gel liquid microdroplets 57
3.3.2 Size distribution of generated microdroplets inside the flow focusing microfluidic device 59
3.3.3 Photoinitiated polymerization of pre-gel Acrylamide solution droplets 59
3.3.4 Microbeads functionalization and protein conjugation 62
3.3.5 Mechanical characterization of microbeads 64
3.3.6 Spatial distribution of fluorescent nanobeads inside PAAm Hydrogels 69
3.3.7 Quantification of encapsulation mechanical forces exerted by vascular endothelial cells on schistosoma mansoni egss of varying stiffness 73
3.4 Discussion 75
3.5 Conclusions 88
3.6 Acknowledgements 91

Chapter 4 A capillary controlled hydrogel micro-channel for isotropic compressive stress quantification 92
4.1 Introduction 92
4.2 Materials and Methods 95
4.2.1 Microfluidic devices design and fabrication 95
4.2.2 PolyAcrylamide microchannel generation 97
4.2.3 Cell Culture 99
4.2.4 Microscopy and Imaging 99
4.2.5 Image Processing 100

4.3 Results . . . 100
4.3.1 Controlling the position of the pre-gel liquid interface . . . 101
4.3.2 Local curvature distribution and mean curvature radius of the pre-gel liquid interface . . . 101
4.3.3 Reconstructed geometries of the nozzle of proposed liquid interfaces . . . 103
4.3.4 Photopolymerized microchannels . . . 105
4.4 Discussion . . . 106
4.5 Conclusions . . . 110
4.6 Appendix . . . 111
4.6.1 Photo-activated polymerization of polyacrylamide hydrogels at the micron scale inside PDMS microfluidic devices . . . 111
4.7 Acknowledgements . . . 118

Chapter 5 Concluding Remarks . . . 119

Bibliography . . . 122

LIST OF FIGURES

Figure 2.1: Scanning Electron Micrographs (SEM) of microfabricated PDMS flexible rods . . . 10
Figure 2.2: Phase contrast images of a migrating epithelial monolayer of MDCK cells over 50h. . . . 18
Figure 2.3: Local density maps of a migrating epithelial monolayer of MDCK cells over 50h. . . . 19
Figure 2.4: Statistical analysis of local density maps distributions in an epithelial monolayer. . . . 20
Figure 2.5: Quality control of the purity of transfected cell lines via imaging methods, statistical analysis and estimation of out-of-sample prediction error. . . . 23
Figure 2.6: Selection of optimal fluorescent strains via quantification of the parameters of statistical analysis of the distribution of intensities for every strain. 24
Figure 2.7: Mechanical phenotyping of transfected cell lines. Strain proliferation analysis. . . . 25
Figure 2.8: Mechanical phenotyping of transfected cell lines. Piezo1 overexpressed cell lines proliferation assay results. . . . 26
Figure 2.9: Mechanical phenotyping of transfected cell lines. Migration assays and Traction Force (TFM) quantification. . . . 27
Figure 2.10: Interaction of epithelial monolayers with three dimensional Collagen-coated PDMS pillars. . . . 29
Figure 2.11: SEM images of the interaction of epithelial monolayers with collagen-coated flexible PDMS microrods. . . . 30
Figure 2.12: Fluorescent confocal images of PDMS pillars coated with: a-b) Collagen type I, c-d) PLL-PEG and e-f) ECadherin:Fc protein, and interacting with ECad-GFP expressing MDCK cells. . . . 32
Figure 2.13: Fluorescent confocal images of PDMS pillars coated with ECadherin:Fc protein, and interacting with H2B-mCherry expressing MDCK cells. . . . 33
Figure 2.14: Scanning Electron MIcrographs (SEM) of MDCK cells climbing over non-adherent PLL-PEG coated microrods. . . . 34
Figure 2.15: MDCK monolayer cell area dynamic evolution over a time course of 25 hours until reaching full confluency. . . . 36
Figure 2.16: Piezo1 may regulate Contact Inhibition of Proliferation (CIP) through YAP/TAZ signaling. . . . 37
Figure 2.17: YAP immunostaining in MDCK monolayers. . . . 38

Figure 3.1: Microfluidic device schematic for PAAm microspheres . . . 44

Figure 3.2: Flow focusing microfluidic device used to produce pre-gel microdroplets showing passive breakup at T junctions and homogeneous droplet distribution . . . 58
Figure 3.3: Size distribution of pre-gel droplets produced with a flow focusing microfluidic device VS droplets produced through inverse emulsification via vortex mixing. . . . 60
Figure 3.4: Photopolymerization of pre-gel solution microdroplets. . . . 63
Figure 3.5: Schematic diagrams of the coupling reactions between PolyAcrylamide (PAAm) gels and ECM proteins. . . . 65
Figure 3.6: PAAm microbeads functionalization and protein conjugation. . . . 66
Figure 3.7: PolyAcrylamide gels elasticity analysis by AFM indentation. . . . 68
Figure 3.8: Spatial distribution of fluorescent nanobeads inside planar PolyAcrylamide gels. . . . 71
Figure 3.9: Spatial distribution of fluorescent nanobeads inside spherical PolyAcrylamide microbeads generated with our flow focusing device. . . . 72
Figure 3.10: Comparison between nanobeads density distribution for each z plane for planar PAAm gels VS photoinitiated polymerized PAAm microspheres. . 73
Figure 3.11: Three-dimensional view of a photoactivated polymerized PAAm microsphere functionalized with FN and completely engulfed by vascular endothelial cells (HUVEC) . . . 76
Figure 3.12: SEM captures of different size fibronectin coated PAAm microbeads interacting with vascular endothelial cells . . . 77
Figure 3.13: Schistosoma mansoni eggs induce vascular endothelial cells (VECs) to exert 3-D forces for egg encapsulation. . . . 78
Figure 3.14: Cleavage of I2959 and LAP into substituent radicals following photon absorption. . . . 85

Figure 4.1: Venous sinuses in the red pulp of the spleen . . . 93
Figure 4.2: Microfluidic device to study the mechanics of RBC inter-endothelial splenic transmigration . . . 94
Figure 4.3: Microfluidic device schematic for PAAm microchannels . . . 96
Figure 4.4: Timelapse representation of the microfluidic channel operation and interface controllability. . . . 102
Figure 4.5: Local curvature analysis of the free surface of the pre-gel solution inside the microfluidic device while operating. . . . 103
Figure 4.6: Analysis of mean radius of curvature for the different interfaces inside the microfluidic device while operating in the liquid phase. . . . 104
Figure 4.7: Photopolymerized microchannels inside our microfluidic device. . . . 105
Figure 4.8: Bright-field images of neutrophil transendothelial migration (TEM) 5 h after neutrophil injection under single chemoattractant gradients. . . . 108

Figure 4.9: Effect of oxygen concentration on photopolymerization 112
Figure 4.10: UV photopolymerization of PolyAcrylamide (PAAm) solutions on top of different substrates 114
Figure 4.11: Gradient-induced migration of Pluronic and resulting microchannel polymerization with Pluronic PDMS formulation 116

LIST OF TABLES

Table 4.1: UV photopolymerization of PolyAcrylamide samples 117

ACKNOWLEDGEMENTS

There are so many individuals I would like to thank for their key contributions to the success of my Ph.D. that I would probably need a separate document to be minimally fair to them. I am grateful to say that, after all the difficulties and obstacles encountered in this period of my life, it has been such an amazing adventure mostly due to the amount of extraordinary people that I have encountered during this ride.

I would like to start thanking my primary and high school teachers. So many of them I would quickly run out of space. However, the capital importance of their teaching style and inspiration towards us students deserves so much credit I wouldn't even know where to begin. Thank you so much. It was definitely at that time and thanks to the incredible environment that you created, that I started developing my passion for math, physics and science in general.

I would also like to thank my instructors and my academic mentors back in the School of Aeronautics in Madrid. The academic stature of the faculty in our beloved "Escuela" was underlooked at the time and only with the perspective that living in a different country gives one, could I begin to appreciate the incredible technical education I acquired. Professors Luis Conde, Jose Manuel Donoso and Ezequiel del Rio gave me the opportunity to work at the PlasmaLab and without me even realizing it, started my academic career between vacuum chambers and ion sources. Without their work ethics, sense of humor, support and encouragement I would probably not be writing these lines today.

At this point, I need to give a special acknowledgment to Professor Juan de la Mora at Yale University. He gave me the amazing opportunity of joining his laboratory at the Mechanical Engineering department of one of the most prestigious institutions in the world, to conduct research in the fascinating field of electrospray ionization and the combined techniques of ion mobility and mass spectrometry. Professor de la Mora has been, without a doubt, a model of integrity, hard work, fairness and passion for science that I will forever be thankful for.

I need to dedicate a special moment as well for my doctoral advisors, Juan Carlos del

Alamo and Juan Lasheras. Thanks to them I have been able to study and conduct research in an incredibly vast amount of exciting bioengineering problems of huge relevance. Their passion for science and research is incredibly contagious and I will be forever thankful for helping me pursuing my passion of contributing to biomedical research from an engineering perspective. The exceptional environment that constitutes UC San Diego and all the related research institutes and medical centers in the area, combined with their expertise in multi-scale biophysical problems created the perfect research environment for someone like me.

Thanks to all the members of my doctoral committee and the rest of Professors in the Biomechanics area for their support, for their suggestions and for their time. Padmini, David, James, Alison were always a big inspiration to me and academic figures to look up to.

Thanks to all the amazing and talented people of our research group: to Lorenzo, Ricardo, Shun, Stephanie, Cathleen for being such great friends, and for always giving a good reason to be at work; to Marissa, Kristen, Ashish, Josh, Yi-Ting, Ruedi, Alex, Effie, Manu, Bego for their smiles, their invaluable insight and for being great labmates in general.

Thanks to all the other students and post docs in the Biomechanics wing of SME and in the Mechanical and Aerospace Engineering department, present and past, for making the workplace the perfect place to spend my days: Maxime, Morgan, Deba, Hari, Barath, Abhay, Justin, Mahdi, Miriam, Brato, Roberto, Gopesh, Jennifer, Andrea, Achal, Houssein, Lucas.

To all my friends in San Diego... You have made my time here so incredible and special. Nerea, Talesa, Aimee, Crystal, Alex, Andre, Javier, Andreas, Kostas, Ryan, Augusta, Matt, Jessie, Gerrit, Simone, Ana, Blanca, Martina, Ayheza, Raul, Andrei, Amalia, etc. Only these lines of names deserve 6 years of PhD.

I would also like to thank my friends in Spain, because without all the support and friendship thorough different countries and several decades I don't even know where I would be. Oscar, Graci, Lourdes, Gonzalo, Irene, Ricardo, Luis, etc. Thank you for everything.

To Liz, because this past year and a half has been incredibly amazing by your side and because your patience and love are unmatched. Thank you for being there all the time.

And finally and foremost I would like to thank my parents Antonio and Prado, my sister Maria and also Juanma and Estrella, because all this is because of them and for them and I couldn't even have thought of all the incredible adventures I would live in the US if it wasn't for their continuous support, encouragement and love. I love you all very much.

Chapter 2, in part, is currently being prepared for submission for publication of the material. Criado-Hidalgo, Ernesto; Yeh, Yi-Ting; del Álamo, Juan C.; Lasheras, Juan C. The dissertation author was the primary author of this paper.

Chapter 3, in part is currently being prepared for submission for publication of the material. Criado-Hidalgo, Ernesto; Garcia-Herreros, Antoni; Yeh, Yi-Ting; Lasheras, Juan C.; del Álamo, Juan C. The dissertation author was the primary investigator and author of this material.

Chapter 3, in part is also currently being prepared for submission for publication of the material. Yeh, Yi-Ting; Skinner, Danielle; Suzuki, Brian; Youjeong, Na; McKerrow, James; Criado-Hidalgo, Ernesto; Zhang, Shun; del Álamo, Juan C.; Caffrey, Connor. The dissertation author was a co-author of this material.

Chapter 4, in part is currently being prepared for submission for publication of the material. Criado-Hidalgo, Ernesto; Garcia-Herreros, Antoni; Yeh, Yi-Ting; Lasheras, Juan C.; del Álamo, Juan C. The dissertation author was the primary investigator and author of this material.

VITA

2008	Ingeniero Aeronáutico (B.S.| M.S.), Universidad Politécnica de Madrid (Spain)
2008-2011	R&D Staff Engineer, SEADM S.L. (Spain)
2011-2013	Visiting Assistant in Research, Yale University
2013-2015	"la Caixa fellow. Graduate Student", University of California San Diego
2014	M.S. in Engineering Sciences (Applied Mechanics), University of California San Diego
2015 - 2019	Graduate Student Researcher, University of California San Diego
2017 - 2018	Teaching Assistant, University of California San Diego
2020	Ph.D. in Engineering Sciences with Specialization in Multi-Scale Biology, University of California San Diego

PUBLICATIONS

Coenen W, C, Gutierrez-Montes C, Sincomb S, Criado-Hidalgo E, Wei Ke, King K, Haughton V, Martinez-Bazan, Sanchez A L, Lasheras J C. "Subject-specific evaluation of CSF bulk flow in the spinal canal: recirculating flow patterns and implications for ITTD drug dispersion". *American Journal of Neuroradiology* (2019).

Zhang S, Skinner D, Joshi P, Criado-Hidalgo E, Yeh Y, Lasheras JC, Caffrey C, del Álamo, Juan C.. Quantifying the mechanics of locomotion by the schistosome pathogen to changes in its physical environment. *Journal of The Royal Society Interface*. **16** 2019.

Sánchez AL, Martínez-Bazán C, Gutiérrez-Montes C, Criado-Hidalgo E, Pawlak G, Bradley W, Haughton V, Lasheras JC. On the bulk motion of the cerebrospinal fluid in the spinal canal. *Journal of Fluid Mechanics* **841** (2018): 203-227

Yeh Y., Skinner D.E., Suzuki B.M., Youjeong N., McKerrow J.H., Criado-Hidalgo, E., Zhang S., del Álamo J.C., Caffrey C.R. "Biomechanical interactions of Schistosoma mansoni eggs with vascular endothelial cells". (In preparation)

Criado-Hidalgo, Ernesto; Yeh, Yi-Ting; del Álamo, Juan C.; Lasheras Juan C. "Piezo1 regulates Contact Inhibition of Proliferation (CIP) via YAP/TAZ signaling", (In preparation)

Criado-Hidalgo, Ernesto; Garcia-Herreros, Antoni; Yeh, Yi-Ting; Lasheras Juan C.; del Álamo, Juan C. "Fabricating biocompatible polyacrylamide microbeads for cell-generated mechanical force quantification via photoinitiated polymerization", (In preparation)

Criado-Hidalgo, Ernesto; Garcia-Herreros, Antoni; Yeh, Yi-Ting; Lasheras Juan C.; del Álamo, Juan C. "A capillary controlled hydrogel microchannel for isotropic compressive stress quantification", (In preparation)

ABSTRACT OF THE DISSERTATION

Microfabricated platforms for the characterization of single and collective cell migration mechanics

by

Ernesto Criado-Hidalgo
Doctor of Philosophy in Engineering Sciences with a Specialization in Multi-Scale Biology
University of California San Diego, 2020
Professor Juan Carlos del Álamo, Chair
Professor Juan C. Lasheras, Co-Chair

The specific way in which individual cells coordinate their migratory behaviors during various physiological processes including morphogenesis, cancer progression or epithelial self-healing, largely depends on the mechanical properties and topology of the surrounding external environment. Collective cell migration has been traditionally studied in flat substrates ignoring tissue heterogeneity that is found in physiological conditions. In addition to this, existing literature has been mostly focused on contractile forces at the cell-ECM interface while leaving cell-cell force measurement under-looked as well as neglecting compressive or pushing forces. This dissertation addresses some of these limitations proposing a novel methodology to characterize collective cell migration when physical obstacles are present and provides a framework to quantitatively study the complex dynamics observed in developing tissues.

Force exertion is an integral part of cellular phenotype regulating important cell func-

tions and fate. In order to quantify mechanical forces at the cellular scale, traction force microscopy has traditionally been considered a standard when quantification of forces at the cell-substrate interface are required. However, quantification of compressive and shear stresses in three dimensions have been elusive due to the lack of experimental and computational techniques appropriate for this sizable challenge. This dissertation presents a novel methodology to produce photo-initiated elastic round microgels that can be functionalized and embedded in three dimensional tissues for force quantification.

We also present a novel family of PDMS microfluidic devices with ∼1-micron narrow constrictions intended to characterize and quantify mechanical forces experimented by cells when they squeeze through narrow gaps in extracellular matrices, as observed in neutrophil migration or even cellular structures, as red blood cells squeezing through interendothelial slits in the spleen. At the cusp of each constriction, we harnessed capillary phenomena to embed photopolymerizable hydrogels of tunable geometry and mechanical properties, seeded with fluorescent ∼0.1-micron particles. As cells squeeze through the constrictions, the hydrogel deforms leading to motion of the fluorescent particles. This motion can be recorded with a microscope and analyzed to calculate stresses using traction force microscopy.

Chapter 1

Introduction

During three-dimensional tissue development, the cells of many embryonic tissues actively narrow in one dimension and lengthen in the perpendicular dimension (convergence and extension). These two mechanisms seem to be ubiquitous in metazoan morphogenesis [1, 2]. During these movements, poilaryzed cells intercalate between one another in intricate ways that are yet not fully understood.

The way cells coordinate their behaviors and life cycles depends greatly on the mechanical properties of the external environment, specifically described as the extracellular matrix (ECM) [3]. Collective cell migration is a highly regulated process involved in a vast variety of situations, such as wound healing, development, cancer progression and metastasis. Mechanical and biochemical cues provide important regulatory cues that allows collective coordination of cell movements and force exertion [4].

In particular, epithelial monolayers have been widely studied as a proxy for developing tissues and also due to their rich dynamics that has allowed researchers to learn a huge amount of information about self-healing [5], long range mechanical patterns induced by cell division [6] or even the origin, transmission and implications of mechanical waves travelling through epithelial layers [7, 8, 8–10]. A vast amount of research has also been devoted to elucidate some of the mechanisms that regulate wound healing in adherent and non-adherent environments as well as reallistic configurations that reseemble the innner and outer part of blood vessels [11–14].

However, three-dimensional platforms have been less explored in part for the inherent difficulty of jumping to a full 3D setup that requires specialized assays and imaging techniques. In particular, the study of epithelial monolayers interaction with obstacles with a diverse range of mechanical properties and protein coatings has been largely unexplored. We tried to address some of these issues in the context of this dissertation.

In addition to epithelial monolayers, there has been significant effort over the past fifteen years to try and come up with tools to directly quantify cellular force exertion in vivo. Liquid droplets and soft round hydrogels have been proposed as force probes to directly quantify three-dimensional traction forces, however, all the methodologies proposed so far still exhibit significant limitations, ranging from the inability to quantify compressive forces [15] to heterogeneous mechanical properties [16] of the micrometric gels or the need of complicated setups and superresolution imaging techniques [17]. The development of force quantification platforms in 3D and in vivo still need significant effort in order to achieve standardized protocols that make three-dimensional force quantification routinely available in mechanobiology labs.

Despite all these efforts, some of the molecular mechanisms that underlie the biochemical response of living cells to mechanical forces are largely elusive. In our opinion, one of the reasons for this limited understanding has been the lack of suitable methods to measure accurately forces in three-dimensional, developing living tissues with high spatial and temporal resolution. Thus, the main objective of this dissertation was to develop novel experimental and computational methodologies and platforms to measure the spatial and temporal evolution of the intercellular forces during three-dimensional tissue development while simultaneously monitoring the dynamics of the resulting proliferation, differentiation, and migration of the cells within the tissue.

Chapter 2

Collective Cell Migration of Epithelial Monolayers in the Presence of Obstacles

2.1 Introduction

During three-dimensional tissue development, cell-cell confinement, cell-cell traction forces, and the resulting intracellular tension play a key role in regulating not only cell proliferation (cell division), but more importantly, cell differentiation, cell migration, and apoptosis (death). Yet, the molecular mechanisms that underlie the biochemical response of living cells to these mechanical forces are largely elusive. One of the reasons for this limited understanding has been the lack of suitable methods to measure accurately the intercellular forces in three-dimensional, developing living tissues with high spatial and temporal resolution.

Cell proliferation, differentiation and migration is regulated by biochemical signals, growth factors, hormones, and cytokines through a complex array of intracellular signaling molecules. However, it has also been known for some time that extrinsic factors such as cell-matrix and intercellular cell-cell traction forces also regulate cell's behavior. In living biological tissues, these intercellular and intracellular forces are essential to maintaining the tissue structure and function and play a determinant role in controlling homeostasis [18]. The ability of cells to integrate this mechanical information (mechanotransduction) is also known to be central to a wide range of biological processes and has been shown to have

important implications during tissue development as well as in the onset and progression of many diseases [19, 20] However, the molecular mechanisms that underlie the biochemical response of living cells to these mechanical forces are largely elusive due to the lack of accurate methods to measure the intercellular forces in living tissues.

The formation of tissues with specific function and predetermined 3D spatial organization has been the subject of a very large body of research in the field of developmental biology. Single cells maintain and change their shape by stiffening and remodeling their cytoskeleton, while cells in 3D tissues and organs also develop intercellular and intracellular three-dimensional internal forces that are transmitted throughout the tissue by cell-cell adhesions and cell adhesions to the extracellular matrix (ECM). Thus, from a mechanical point of view, it is widely accepted that the action of these inter- and intracellular forces must play a relevant role in the 3D shape and function of living tissues [21].

While some developmental studies in the 1970's pursued these mechanotranduction ideas, the investigation of the role of the mechanical effects during tissue development was pushed aside by advances in cell and molecular biology, and genetics. Consequently, the majority of past and current work on tissue patterning has focused primarily on genetic programming and chemical signaling, and far less interest has been devoted to explore the role of mechanical forces in developmental control.

Increasing numbers of investigators have begun to test these mechanotransduction ideas through rigorous experimentation, and this has led to the discovery of fundamental links between mechanical forces, molecular biochemistry, gene expression and tissue patterning. However, their progress has been slowed down by the lack of reliable techniques to measure the spatial and temporal distribution of intercellular forces in living 3D tissue. The development of this type of methodologies is the main objective of this chapter.

2.2 Materials and Methods

2.2.1 Cell culture

Madin-Darby canine kidney (MDCK) strain II cells, a gift from Prof. Shu Chien's laboratory (UC San Diego, San Diego, CA), and in-house transfected stable MDCK cell lines expressing ECadherin-GFP or H2B-mCherry or mPiezo1-IRES-eGFP or IRES-eGFP were used. Cells were cultured in Dulbecco's Modified Eagle Medium (DMEM, Thermo Fisher Scientific, Waltham, MA) supplemented with 10% FBS (MilliporeSigma,Burlington, MA), 100 U/mL penicillin, and 100 μg/mL streptomycin (Sigma-Aldrich, St. Louis, MO) and maintained at 37°C in a humidified atmosphere with 5% CO2. For transfected MDCK cells, the selection antibody geneticin (G418, Sigma-Aldrich, St. Louis, MO)) was added to the medium at concentrations ranging from 0.5-1 mg/mL.

Plasmids

Lentivirus plasmid for stable expression of the mCherry-tagged histone H2B, PGK-H2BmCherry, was a gift from Mark Mercola (Addgene plasmid # 21217) [22]. E-cadherin-GFP was a gift from Jennifer Stow (Addgene plasmid # 28009) [23]. mPiezo1-IRES-eGFP was a gift from Ardem Patapoutian (Addgene plasmid # 80925) [24].

Cellular transfection

We used E. Coli DH5a (Thermo Fisher Scientific, Waltham, MA) as competent cells and usual protocols for bacterial transformation to introduce the plasmid into the cells [25]. After that step, we purified and extracted DNA through a QIAprep® Miniprep (Qiagen, Hilden, Germany).

Viral particles were then generated using standard protocols. Lipofectamine 2000 (Thermo Fisher Scientific, Waltham, MA) was used to transfect HEK293FT cells. Briefly, the lentiviral constructs pLenti6-H2B-mCherry were transfected into HEK293FT cells that had been previously grown to 95 % confluency in a 10cm petri dish. Cell culture media with viral particles was collected 48 and 72 hours after transfection, and the viral titer was

determined by cell cytometry. Viral stocks contained at least $6{\cdot}10^6$ transducing units per mL titrated on HEK293FT cells. The lentiviruses with polybrene (10mg/mL) were applied to MDCK cells for 24h and then the medium was replaced by fresh DMEM supplemented with 10% FBS.

Stable transfection with Lipofectamine 3000 and posterior selection via G418 was used for the rest of plasmids used in this thesis. Cell lines generated were selected posteriorly via cloning cyliders of Fluorescence-Activated Cell Sorting (FACS).

Molecular cloning

To generate a control vector for our Piezo1 transfection, we cut the mPiezo1 section out by using NotI/PacI restriction enzymes (New England BioLabs, Ipswich, MA) using a double digestion protocol [26]. We later filled in receded 3' ends of DNA fragments to make 5' overhang blunt and ligated the two ends for generating the IRES-eGFP vector.

Fluorescence-Activated Cell Sorting (FACS)

Transfected MDCK samples were sorted using an Aria 2 Sorter (Becton, Dickinson and Company, Franklin Lakes, NJ) from the Human Embryonic Stem Cell Core Facility at UC San Diego. Briefly, cells were trypsinized (Trypsin-EDTA 0.25%, Sigma-Aldrich, St. Louis, MO) and resuspended and FACS buffer (PBS, 1mM EDTA, 1% FBS). Samples containing approximately 1e6 cells were prepared in Falcon™ Test Tubes with Cell Strainer Snap Cap (Thermo Fisher Scientific, Waltham, MA) and maintained at 4°C before sampling.

2.2.2 PolyAcrylamide Gels Preparation

Collagen-coated PAAm gels of $\simeq 20$ μm thickness and 12 mm in diameter were prepared as cellular substrates as previously described by our group [27, 28]. Basically we initially we prepared squared 25 mm coverslips by activating them inside a UV ozone lamp (Model 30, Jelight Co. Irvine, CA) for 10 min and then coating them with a 1M solution of NaOH in deionized (DI) water for 5 min. After this step, we washed out the NaOH solution, rinsed the coverslip with DI water twice and completely dry it using a vacuum

line. We then totally covered the surface of the coverslip with a solution of 3% (v/v) (3-Aminopropyl)triethoxysilane (APTES, Sigma-Aldrich, St. Louis, MO) in ethanol for 20 min at room temperature. After this step, we carefully washed the surface of the coverslip with pure ethanol and soft baked the coverslip for 5 min at 37 °C. The amino-silanated coverslips remain usable typically for a 48 hours period. In case a stronger bond between the coverslip and the PAAm gel is required, this can be achieved by including an extra step consisting of covering the amino-silanated coverslips with 0.5% (v/v) Glutaraldehyde (Sigma-Aldrich, St. Louis, MO) in Phosphate Buffered Saline (PBS) for 30 min at room temperature. This mild and relatively fast reaction (Schiff base reaction) between compounds containing aldehydes (or ketones) and amino groups, result in covalent, and hence stronger, imine groups (Schiff base) that will bind the PolyAcrylamide gel in a stronger manner [29, 30].

Once the coverslips were ready, we prepared the pre-gel solution with a mixture of 5% Acrylamide and 0.3% Bisacrylamide (8.7 kPa, [30]) and seeded them with 0.03% carboxilated FluoSpheres (Invitrogen, Carlsbad, CA). We then mixed the solution with 1% (v/v) of 10% (w/v) Ammonium Persulfate (APS, Sigma-Aldrich, St. Louis, MO) in DI water and N,N,N',N'-Tetramethyl ethylenediamine (TEMED, Sigma-Aldrich, St. Louis, MO) to initiate the polymerization reaction. We then pipetted 3 μL of the pre-gel solution on top of the silanized coverslips, placed a round 12mm coverslip on top, and immediately inverted the mixture and let the gel polymerize for 30 min. During polymerization, the microspheres migrated to the bottom (i.e., the free surface of the gel). We posteriorly used a 0.15 mg/mL Sulfo-SANPAH (Thermo Fisher Scientific, Waltham, MA) solution in DI water to cover the gels, followed by UV activation to facilitate the cross-linking of 125 μg/mL of rat tail Collagen Type I (Dow Corning Inc. Midland, MI) to the surface of the polyacrylamide gels. The gels were incubated for 1 hour at 37 °C and then equilibrated with medium for at least 3 hours. We measured the thickness of the substrates by locating the top and bottom planes of the gel and subtracting their vertical positions as previously described [28]. The Poisson's ratio of the gel was measured to be 0.46, following an elastographic traction force microscopy method previously developed by our group [31].

2.2.3 Microfabrication of bicompatible slender elastic micro-rods

Design

The initial design to generate the mask for the device used to produce slender rods of high aspect ratio in the micrometric range was generated using AutoCAD (Autodesk Software Company, San Rafael, CA).

Photolitography

Microfabricated devices were manufactured using soft lithography [32, 33]. The master device for the micro-rod device was fabricated in a sequential manner initiated by a through cleaning of the 100mm P(100) 1-100 ohm-cm 500um SSP silicon wafer (University Wafer, Inc. Boston, MA) that serves as substrate. Briefly, we baked the wafer at 150 °C for 5 minutes. After that step, we further cleaned the silicon wafer exposing it to a monatomic oxygen plasma inside a PVA Tepla PS100 microwave plasma system (PVA TePla, Wettenberg, Germany) for 5 min at 200W. After this step, a layer of negative photoresist NR9-3000PY (Futurrex Inc. Franklin, NJ) was also spin coated on top of the primed silicon wafer at 4000rpm accelerating at 500rpm/s for 40 seconds. Profilometry measurements using a Filmetrics Profilm3D Optical Profiler (KLA Corp. Milpitas, CA) confirmed the expected thickness of 2.42μm of photoresist. After this step, another postbake at 150°C for 1 min was applied to the coated silicon wafer.

After a short soft bake at 150°C for 1 min, we exposed (250mJ/cm2) the sample under a UV Karl Suss MA6 Mask Aligner (Suss MikroTec Garching, Germany) for 10 seconds, fed with a quartz photomask (Advance Reproduction Corp. North Andover, MA) printed with drawings of our device. A post-exposure bake of 1 min at 100°C was performed and the features were revealed on the wafer by developing the sample for 6 seconds using RD6 Resist Developer (Futurrex Inc. Franklin, NJ). Two 1 min steps of deionized water rinsing were performed to clear the sample from residues. Afterwards and before proceeding to the Deep Reactive Ion (DRI) etching process, the wafer was further cleaned inside the plasma chamber for 3 additional minutes.

In order to etch the desired features on the silicon wafer, the developed 1cm silicon wafer with the exposed desing was cut into a smaller square of $\sim$ 5x5cm and carefully attached to a carrier wafer through a thin homogeneous layer of Fomblin (Solvay Chemicals, Brussels, Belgium) applied to the sample wafer with a Flat Paddle Head Microdenier Cleanroom Swab (Texwipe, Kernersville, NC).

The sample wafer, mounted on top of the carrier wafer (4 inches), was then introduced into the Oxford Plasmalab 100 RIE/ICP deep silicon etcher (Oxford Instruments, Abingdon, United Kingdom), where the B2 standard recipe was ran for 150 cycles with Helium pressures of $\sim$ 10 torr. After this step, sonication with acetone removed any photoresist residue. Profilometry measurements using a Dektak 150 surface profiler (Veeco Instruments Inc. Plainview, NY) confirmed the expected thickness of 20μm.

The etched wafer was finally passivated with tridecafluoro-1,1,2,2-tetra-hydrooctyl-1–1trichlorosilane (Gelest, Morrisville, PA) for 15 min inside a vacuum chamber to prevent PDMS adhesion to the wafer in the casting phase of the manufacturing process.

PDMS casting

PDMS replicas of the micro-rods were made by carefully injecting a thin liquid PDMS solution on the passivated silicon wafer using 18 gauge blunt needles (Becton, Dickinson and Company, Franklin Lakes, NJ). This thin PDMS solution was prepared by mixing a previously degassed (during 30 min) mixture of the PDMS oligomer and crosslinking agent (Sylgard® 184, Dow Corning Inc. Midland, MI) in a 10:1 (w/w) proportion directly with Hexane (Sigma-Aldrich, St. Louis, MO) on a 1:1 volume ratio. Hexane is a well known solvent for PDMS [34, 35] and while it swells cured PDMS, it evaporates fast enough during the curing process so that the mechanical properties of PDMS remain intact [36, 37].

The sample was then cured at 65^{o}C overnight. The next day the master was carefully peeled off the wafer by using a pair of Dumont #5 Fine Forceps (Fine Science Tools, Foster City, CA) and placed on top of a squared 22mm glass coverslip (Thermo Fisher Scientific, Waltham, MA) for storage or activation of PDMS.

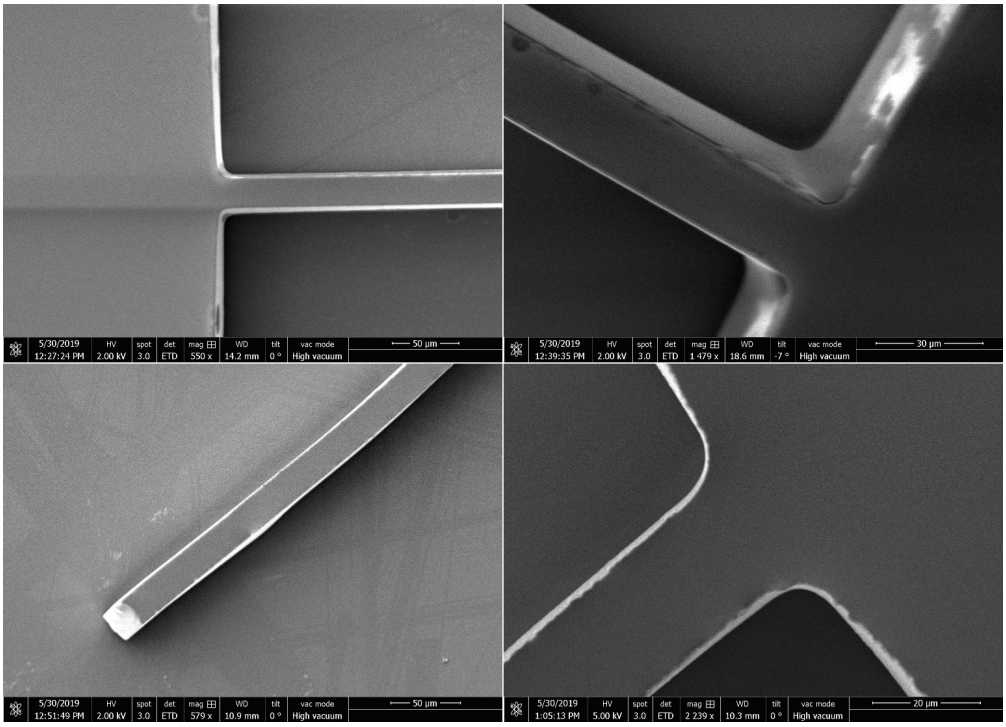

Figure 2.1: SME image of microfabricated PDMS rod casted on the etched silicon wafer. The four different insets show different spatial points of view illustrating the homogeneity of the elastomeric obstacle generated with the methodology described.

Activation and coating with protein or polymer of interest

We activated the surface of the PDMS micro-rods by exposing the samples under a UV ozone lamp (Model 30, Jelight Co. Irvine, CA) for 5 min with an oxygen inflow of 0.2 lpm. This hydroxy groups generated in the PDMS allow for protein adhesion on the activated surface.

For the micro-rods coated with Collagen type I, we basically incubated the recently activated rod with a solution of Collagen I (Corning, Inc. Corning, NY) of 100 μg/mL in PBS for 1h at 37 °C.

To coat the activated micro-rods with the cell adhesion protein E-Cadherin, oriented in the right direction [5], we incubated the activated rods overnight with a solution of 350 μg/mL recombinant protein A/G (Thermo Fisher Scientific, Waltham, MA) in deionized water. After that we washed the sample three times with PBS and a weak detergent to prevent non-specific binding, followed by incubation of the sample with a solution of 350 μg/mL E-Cadherin/Fc Chimera recombinant protein (Sigma-Aldrich, St. Louis, MO) for 3 hours at 37°C. After that we washed again 3 times with PBS and incubated with a 1% (w/v) blocking solution of BSA in PBS for 1 hour at room temperature to block. The last phase consisted of another three washes of the sample with PBS.

To prevent cell adhesion, the micro-rods were incubated with a solution of 0.5mg/mL of PLL-PEG (Nanosoft Polymers Inc. Winston-Salem, NC) in deionized water for 40 minutes at room temperature. This co-polymer presents a dense network of PEG branches that yields the micro-rods non fouling, hence preventing cell adhesion.

2.2.4 Fabrication of PDMS stencils

Rectangular stencils for large wounds

To pattern gaps in the cell culture, we used rectangular PDMS stencils of 10x1mm. The microfabrication of the stencils was similar to that used to fabricate the micro-rods. Briefly, motifs printed on a negative mask were transferred to a silicon wafer by photolithography, followed by a deep reactive ion etching process to obtain rectangles down to the

desired depth in the wafer. The silicon wafer was then silanized to facilitate the release of the PDMS and allow reusing the master multiple times. After this step, the mixture of PDMS:Hexane 1:1 (v/v) previously described was carefully injected on every well using 18 gauge blunt needles.

The wafer containend the injected stamps was then cured at 65^{o}C overnight. The next day the stamps were carefully peeled off the wafer by using a pair of Dumont #5 Fine Forceps (Fine Science Tools, Foster City, CA) and placed on top of a squared 22mm glass coverslip (Thermo Fisher Scientific, Waltham, MA) for storage or activation of PDMS.

Cylindrical stencils

Cylindrical stencils for the experiments of MDCK monolayers interacting with protein coated rigid objects were manufactured in PDMS. Briefly, a large enough volume (sim5mL) of a previously degassed (during 30 min) mixture of the PDMS oligomer and crosslinking agent (Sylgard® 184, Dow Corning Inc. Midland, MI) in a 10:1 (w/w) proportion was prepared and casted on a 100mm untreated culture dish (Thermo Fisher Scientific, Waltham, MA), stored under vacumm for 3h to remove bubbles and cured overnight at 65°C, creating a layer of cured PDMS of several milimiters of thickness.

Stencils were made by carefully punching holes of different diameters (typically sim1, 2 and 2.5 mm) on the PDMS sheet with a biopsy puncher (Miltex, Integra Lifesciences, Plainsboro Township, NJ). After this step, PDMS cylindrical stencils were carefully handled with tweezers and stored for posterior activation and protein coating as described earlier.

Migration assays

In order to perform migration experiments on glass substrates we punched a hole of $\sim$ 16mm of diameter on the bottom of a polystyrene 50x9mm petri dish (Corning Inc. Corning, NY). After that we activated the surface of 22mm squared coverslips (Thermo Fisher Scientific, Waltham, MA) by exposing them under a UV ozone lamp (Model 30, Jelight Co. Irvine, CA) for 10 min with an oxygen inflow of 0.2 lpm. We then proceeded to coat the coverslips with the protein of interest. We covered the coverslips with 200 μL of a

solution of 100 μg/mL of rat tail Collagen Type I (Dow Corning Inc. Midland, MI) in PBS and incubated for 1h at 37°C. After this step, we carefully wahsed out the collagen solution and washed the collagen-coated substrate 3 times with deionized water. Subsequently, we removed the liquid solution with vacuum suction and soft baked the coverslips in the oven for 1h at 40°C before stencil adhesion. This step is crucial when using non-magnetized stencils to facilitate adhesion of the stencil to the substrate.

After this step, we carefully placed the stencils (typically passivated with PLL-PEG) on top of the, now dry, stencils and soft baked the sandwich for 30 more minutes in the oven at 40°C.

We finally glued together the coverslip and the polysterene petri dish using vacuum grease (Corning, Inc. Corning, NY) on the edges of the punched hole, leaving a circular pocket of $\sim$ 16mm in diameter that would serve as the substrate for our cell cultures.

We then seeded 300 thousand MDCK cells suspended on 200 μL of our culture medium (DMEM, 10% FBS, 1%P/S) and incubated for 3-5 hours to facilitate cell attachment in confluent configuration. A careful washing step with warm medium solution at t=1h from the start of incubation facilitates the removal of unattached excess cells in the assay.

After this step, we can carefully remove the attached stencils with tweezers and trigger migration of the epithelial monolayers.

Soft adhesion of PDMS stencils to protein-coated substrates

In order to facilitate the adhesion of the PDMS stencils on top of the protein-coated substrates [38] and prevent undesired dettachment of stencils ahead of time, we introduced a soft baking step in two phases that helped dry the assay just enough to allow the PDMS stencil to adhere sufficiently to the protein-coated glass substrate and stay in place when liquid medium is introduced when we seeded the cells.

Typically some other authors have used in the past magnetized stencils [7] and rare-earth magnets to maintain stencils in place when seeding cells on migration assays, however, in our case, the need to have movable and deformable micro-rods attached to the base stencils made us opt for the soft adhesion option instead.

Basically, a two-phase soft bake process at 40°C that does not damage the protein functionality, is added to protocol allowing, as explained before, the stencil to stay in place while cells are attaching and reaching confluency.

2.2.5 Microscopy and Imaging

Phase contrast microscopy

A Leica DMI 6000B inverted phase contrast microscope (Leica Camera, Wetzlar, Germany) controlled by a dedicated workstation running the open source μ-Manager software (Vale lab, UCSF) was used for image acquisition. The microscope was equiped with a Zyla 3-Tap Enclosed C-mount 16 bit camera (Andor Technology, Belfast, UK) and a Mercury Short-Arc Discharge Lamp with Reflector with emission filters to generate excitation light in the common DAPI, FITC, TRITC, and CY5 wavelengths.

Timelapse sequences were acquired every 120 seconds in bright field (BF) and fluorescent field (FLUO) under a 10x air lens and exposures ranging from 10-20 ms (BF) and 100-200 ms (FLUO).

A Primovert Inverted Microscope (Carl Zeiss AG, Oberkochen, Germany) was used to examine unstained cells in phase contrast under 10x, 20x and 40x objectives.

An Axio Observer Inverted Microscope (Carl Zeiss AG, Oberkochen, Germany) with bright field, dark field and differential interference contrast (DIC) capabilities, was used to examine etched silicon wafers under a 100x air objective.

Confocal microscopy

Three dimensional z-stack bright field and fluorescent images of samples were taken using an Olympus IX81 confocal microscope (Olympus Corp. Tokyo, Japan) with a cooled CCD camera (Hamamatsu Photonics, Shizuoka, Japan), using Metamorph software (Molecular Devices LLC. San Jose, CA) and a 40$\times$ N.A. 1.35 oil-immersion objective. Following the acquisition, the sequences of z-stack images were analyzed using the software suite Volocity (PerkinElmer, Waltham, MA), which rendered some of the optical sections into 3D models.

2.2.6 Immunofluorescence microscopy

Cells were fixed with 4% paraformaldehyde (Sigma) for 30 min, permeabilized with 0.25% Triton X-100 (Sigma-Aldrich, St. Louis, MO) in PBS (Sigma-Aldrich, St. Louis, MO) (vol/vol) for 5 min, and blocked in 1.5% BSA (Sigma-Aldrich, St. Louis, MO) in PBS for 30 min. Staining was performed with primary mouse monoclonal antibody against YAP antibody (Abcam, Cambridge, United Kingdom) provided at 100 μg/mL, diluted 1:50 in 2% BSA in PBS and detected with a monoclonal anti-mouse conjugated with 488 Alexa Fluor (Invitrogen, Carlsbad, CA) at 1:100 in PBS.

Samples were mounted in Mowiol mounting media (Biotium, Fremont, CA) and imaged with an Olympus IX81 confocal microscope (Olympus Corp. Tokyo, Japan) with a 60× or 100× 1.4 N.A. apochromat oil immersion objective lens.

Scanning Electron Microscopy

To prevent the presence of any organic contaminants inside the Scanning Electron Microscope (SEM), we fixed the samples using a fixative buffer composed of 4% Paraformaldehyde (PFA, Biotium, Freemont, CA) supplemented with 2.5% of Glutaraldehyde (Sigma-Aldrich, St. Louis, MO) in Phosphate Buffered Saline (PBS). We first aspirated the medium in our samples, covered them completely with the fixative buffer and incubate overnight at 4 °C.

After overnight fixation, we aspirated and stored the PFA solution and cover the samples with PBS prior to serial dehydration. We then prepared a series of ethanol concentrations in DI water for dehydration of our samples (50%, 60%, 70%, 80%, 90%). We continued rinsing our samples with fresh buffer (PBS) and replacing the buffer solution with the lowest concentration ethanol solution (50%) and left for 15-20 minutes. We continued the process with increasing ethanol concentrations until we reached 100%, and repeated twice the last step of the serial dehydration process. The samples were then dehydrated and ready for drying.

To prevent collapse of biological samples due to surface tension, Critical Point Drying

(CPD) was performed on all samples following dehydration using a Tousimis AutoSamdri 815A critical point dryer (Tousimis, Rockville, MD). Previously dehydrated samples were placed inside the CPD chamber with sufficient ethanol to completely cover the samples. The chamber was then sealed and cooled, as valves were opened letting liquid CO_2 in and venting ethanol out, until liquid CO_2 completely replaced ethanol. The chamber was then sealed again and slowly heated until the critical point was reached at about 1350psi and $\simeq$ 35 °C. The CO_2 was then slowly drained from the chamber as a gas, preventing surface tension damaging effects in the sample.

After CPD, the sample was ready for sputter coating. This process was performed on a Emitech K575X Iridium Sputter Coater. Basically the samples were introduced inside the sputtering chamber, vacuum was applied until the pressure reached $\simeq 10^{-2}$ mbar and the system was run at 85mA for 8 seconds yielding samples coated with a thin layer of iridium and ready for SEM imaging.

Imaging was thereafter performed using a FEI Quanta FEG 250 SEM with environmental capabilities. Images were acquired at 1kV and with magnifications ranging from 441X to 16.77kX.

2.2.7 Image Processing

Image processing was performed using Fiji and ImageJ [39] as well as in-house developed Matlab scripts. Initially images were imported to the workstation through Fiji's Bioformat plug-in, converted into separate 16-bit tiff images and stored back as individual tiff images for each channel and z level. These separate files were then imported into Matlab for further processing. Images were normalized, cleaned up applying median and gaussian filters and contrast was equalized when needed through Contrast Limited Adaptive Histogram Equalization (CLAHE), for visualization purposes only [40].

Velocity mapping and individual cells identification and tracking

Timelapse images of migrating monolayers were acquired every 2 minutes in bright field (BF) and fluorescent field (FLUO), using the TRITC channel (547/572 nm). We used

exposure times as low as 10ms for BF and 200ms for the FLUO channel. The high dynamic range in the bright field images allowed us to perform velocimetry via standard Particle Image Velocimetry (PIV) between consecutive pairs of images. Basically we used a low-pass dynamic filter based on finite differences to filter out fast moving debris and used an in-house developed PIV suite using window sizes of 32 pixels with 50% overlap [27].

In order to track individual cells within the epithilial monolayer, we took advantage of the histone labelling achieved on the H2B-mCherry transfected cell line. The high signal to noise ratio achieved with our transfected cell line allowed for efficient identification of individual cells. Briefly, segmentation on two-dimensional FLUO images was performed by statistical separation of the region of interest from the background through a Gaussian Mixture Model [41] aimed at fitting two distinct distributions of pixel intensities. Once the background region was identified and ruled out, specific positions of individual cells were computed using local maxima and weighted centroid approaches. Further refinement of the (x,y) position was achieved by using a radial-symmetry-based particle localization approach with subpixelar capabilities [42].

2.3 Results

In this section we show some preliminary results that illustrate the methodologies developed in this study. We show the characterization of the different epithelial cell lines developed in this thesis as well as a method purely based on fluorescent imaging to select specific clones in a quantitative manner and that also serves as the stepping stone for a full mechanical characterization of the clones of interest. We used fluorescent imaging techniques as well as traditional migration and proliferation assays, combined with Traction Force Microscopy measurements to asses the suitability of the selected cell lines as models for mechanobiology studies involving epithelial tissue development.

We also show preliminary results of the interaction of epithelial cell lines with obstacles in three dimensional assays coated with different proteins and also interacting with non-fouling obstacles.

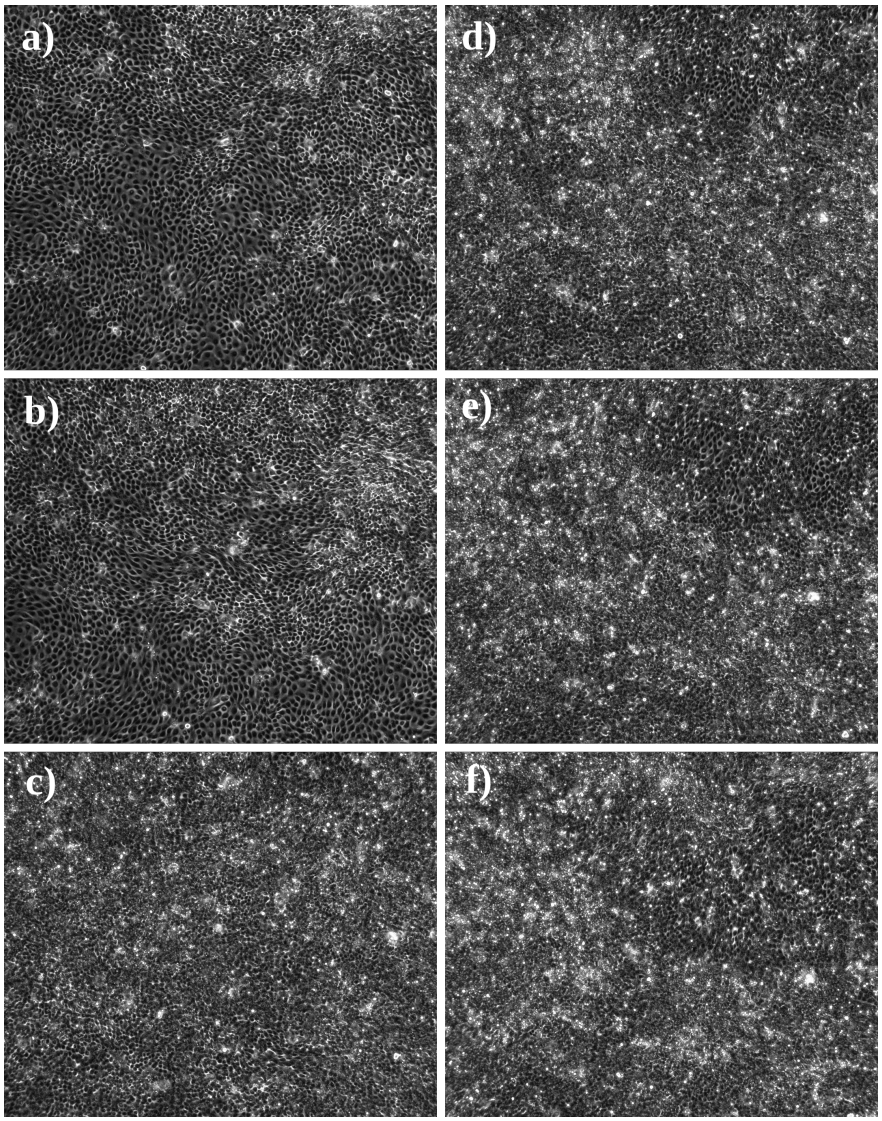

Figure 2.2: Phase contrast images of a migrating epithelial monolayer of MDCK cells over 50h. Inserts a-c) correspond to t=0h, t=8.3h and t=33.3h respectively. Inserts d-f) correspond to t=37.5h, t=40h and 42.2h respectively, where traveling compressive waves are observed

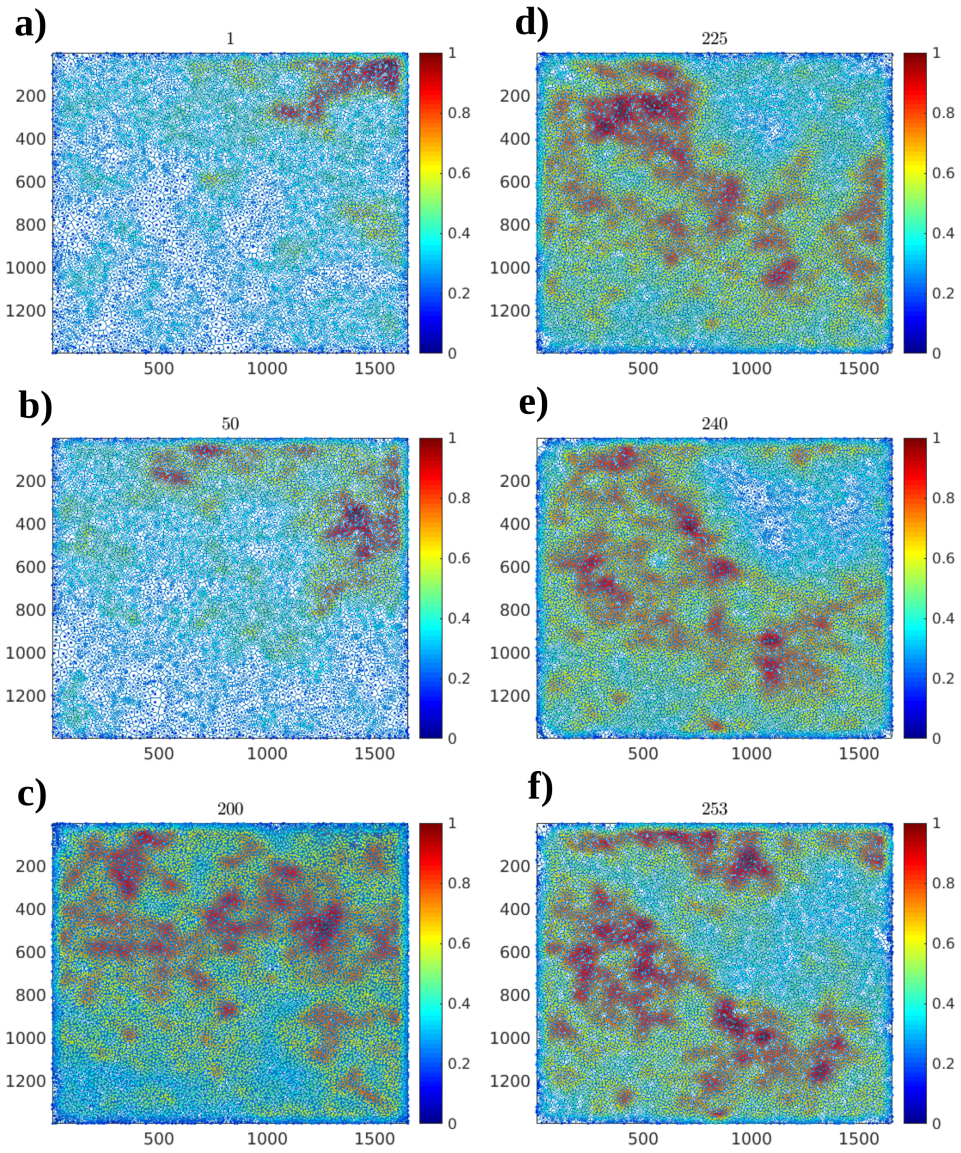

Figure 2.3: Local density maps of a migrating epithelial monolayer of MDCK cells over 50h. Inserts a-c) correspond to t=0h, t=8.3h and t=33.3h respectively. Inserts d-f) correspond to t=37.5h, t=40h and 42.2h respectively, where traveling compressive waves are observed by dynamic differences in tissue density

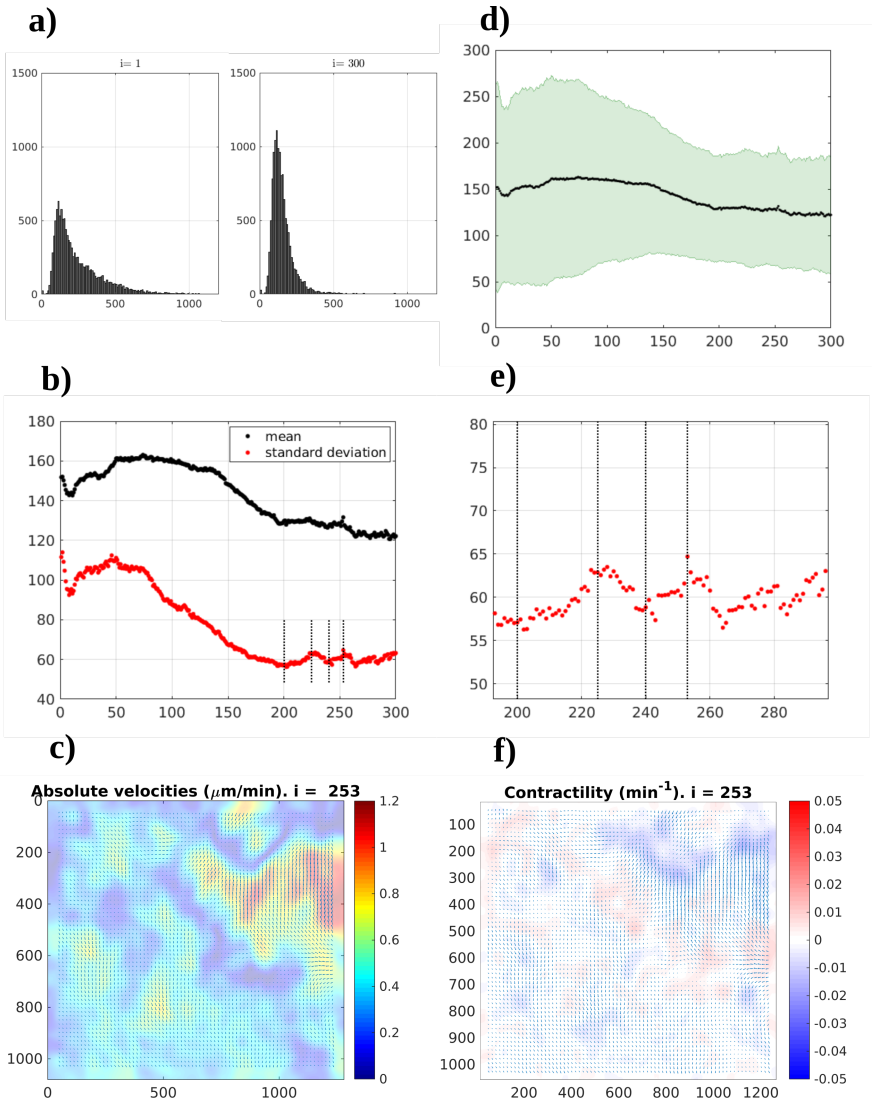

Figure 2.4: Statistical analysis of local density maps distributions in an epithelial monolayer. a) Density histograms for initial and final time points of the timelapse (50h). b) Mean and standard deviation of cell density over time. c)Absolute velocity map for t=42.2h. d) Mean and standard deviation shaded representation. e) Fluctuations in density standard deviation correlate with compressive waves in the tissue. f) Strain rate maps show mechanical waves in the tissue at t=42.2h.

We finally introduce some results that led us to hypothesize a mechanism that could potentially be responsible for controlling Contact Inhibition of Proliferation (CIP) on epithelial monolayers.

2.3.1 Mechanical phenotyping of epithelial cell lines

Cells derive their mechanical properties from the structure and dynamics of their intracellular components, including the cytoskeleton, cell membrane, nucleus, and other organelles. Identifying differences within a population of one cell type or different cells among heterogeneous populations, or trying to detect changes due to disease or environmental interactions all based on cellular mechanical properties has potentially important implications for cell and tissue biology and even clinical settings [43].

Standard techniques for mechanical characterization of cellular properties have been Atomic-force microscopy (AFM), micropipette aspiration, optical tweezers, microplate rheometry or even more microfluidics-based techniques such as hydrodynamic stretching cytometry, suspended microchannel resonators or real-time deformability cytometry (RT-DC) [44].

Since we were interested in a more dynamical aspect of the mechanical phenotype of MDCK cell monolayers, in this thesis we mostly used techniques that involve a temporal component, such as migration assays, cell proliferation assays and even Traction Force MIcroscopy (TFM).

Since all our transfections involved expression of fluorescent proteins, we developed an automated and fully stochastic imaging methodology to select individual cellular strains after transfection and sorting. This methodology only requires the input of a minimum level of fluorescent intensity for the region of interest and a threshold for the resolution of the intensity peak. This way, monodisperse cell lines with a sufficiently high level of fluorescence can be selected for downstream analysis and experimentation.

Strain selection via fluorescence imaging and statistical quantification

The first step of our proposed methodology consists of detecting the location of fluorescent peaks. We used fluorescently labelled nuclei as benchmark for our methodology.

However, any fluorescent marker could be also processed with the same pipeline. We initially separated background from the fluorescent objects using a Gaussian mixture model with two different distributions capable of separately fitting the population of fluorescent objects from the background (Fig. 2.5.a and 2.5.b)

After locating all fluorescent nuclei via locating local maxima or weighted centroid of gaussian filtered regions, we established a region of interest around the location of the peak, according to typical averaged size of the nuclei [45], and quantified the average intensity inside the box. Once we had this, we plotted the histograms of intensities for all cells in the field of view and trid to fit this time an undetermined number of Gaussian distributions (Fig. 2.5.d). The most probable model was selected using the Akaike information criterion [46]. We would obtain the best results for 1 or 2 Gaussian when the strain is pure and 2 and 4, when it is contaminated with a foreign clone and thus, allowing us to spot possible non-pure strains or clones and discard them.

Once we had statistical distributions of all pure clones, we defined ad hoc criteria for a mi.nimum and maximum mean intensity level and a minimum resolution (corresponding to the standard deviation of the statistical distribution of intensities) of the peak. This allowed us to short list the number of strains that would match our requirements in terms of imaging quality and homogeneity (Fig. 2.6).

Once the cell strains were shortlisted, a series of assays were performed to ensure the viability of the clones for mechanobiology experimentation. In particular, cell proliferation, migration and traction force microscopy assays were performed to ensure a benevolent mechanical behavior of the selected strains.

Cell Proliferation

Cell proliferation quantification over a period of 6 days was performed for the different strains. The results were fitted to a 4 parameter logistic model showing no significant differences between the transfected strains and the wild type (WT) control (MDCK strin II in this case). The results can be seen in Fig. 2.7.

For the mPiezo1 transfected strains, different levels of proliferation were observed

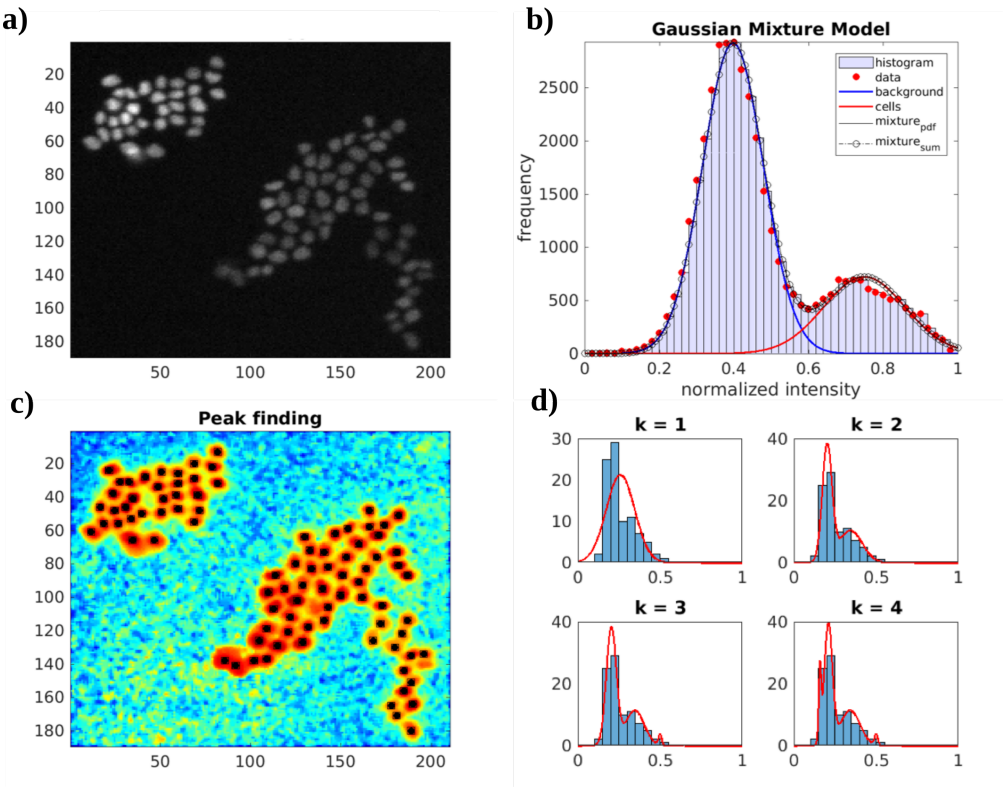

Figure 2.5: Quality control of the purity of transfected cell lines via imaging methods. After cloning, more than one clone could be present in the culture (a). A Gaussian Mixture Method (b) of the different possible strains found in the culture is performed from their identified peaks fluorescence intensities (c) and the Akaike Information Criterion is used to provide relative quality of statistical models for the possible number of strains poresent in the culture

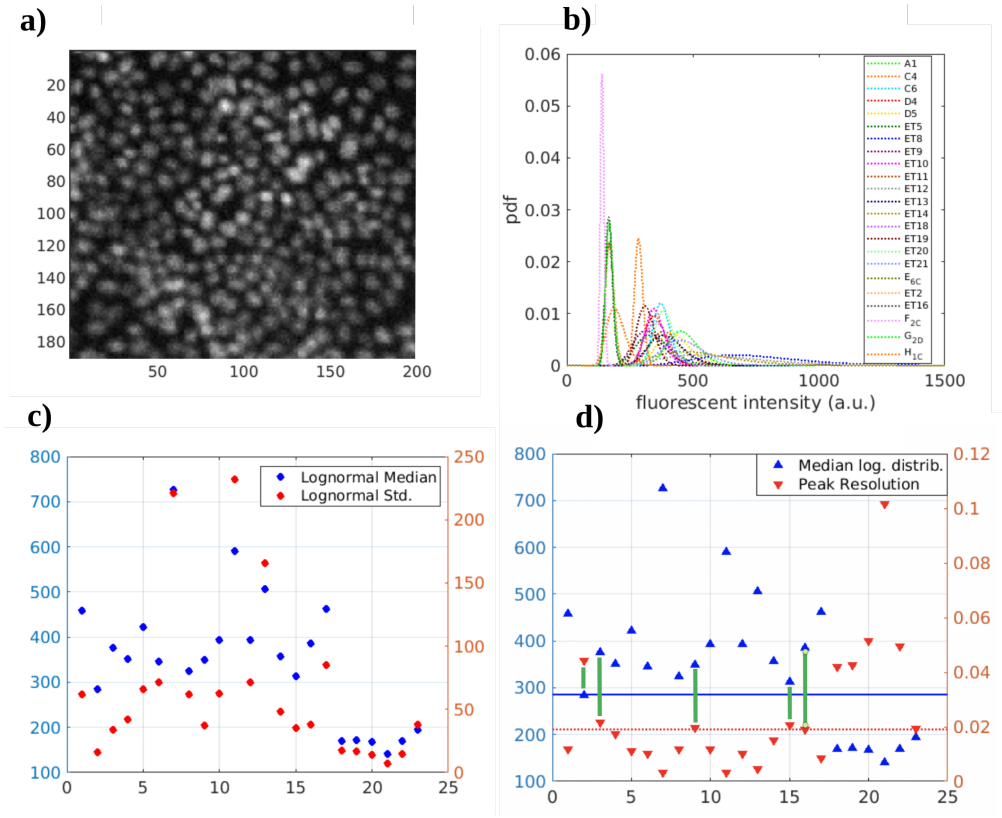

Figure 2.6: Selection of optimal fluorescent strains via quantification of the parameters of statistical analysis of the distribution of intensities for every strain. a) Fluorescent images for the H2B-mCherry transfected cell line. b) Probability density functions of the fluorescent cells for all the different clones. c) Evaluation of characteristic parameters of lognormal fitted distributions. d) Selection of strains with sufficient resolution and median intensity.

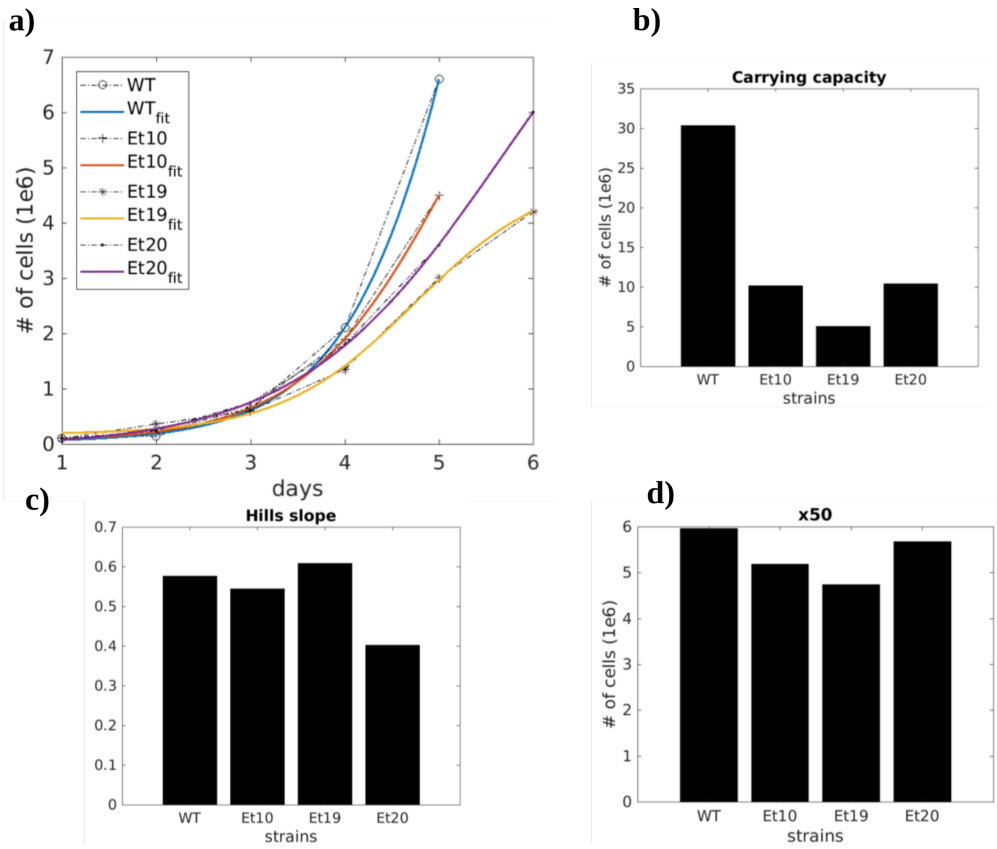

Figure 2.7: Mechanical phenotyping of transfected cell lines. Strain proliferation analysis via four parameter logistic models. a) Proliferation assay data for different strains and fitting to model. b) Carrying capacity. c) Hills slope. d) Point of inflection.

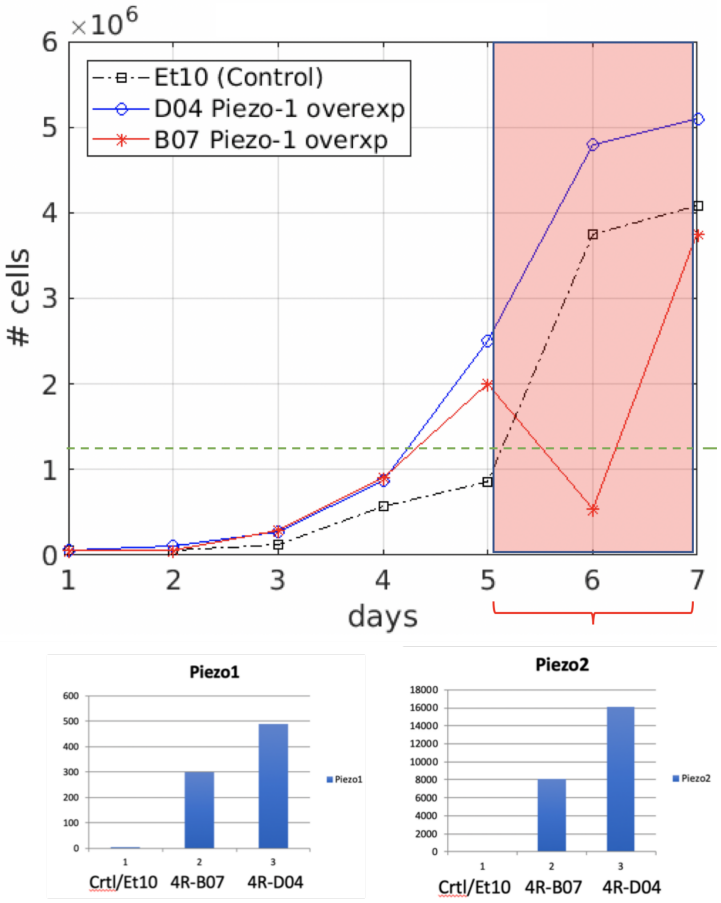

Figure 2.8: Piezo1 overexpressed cell lines proliferation assay results. Top figure shows proliferation for the different cell lines expressing different levels of Piezo1 and homologous Piezo2. Bottom part of figure show levels of expression ran in gels.

correlating with the level of protein expression (checked with gel electrophoresis).

Collective cell migration

Speed of migration in cell monolayers is also a very relevant mechanical paramater that needed to be quantified and checked in order to make sure the fluorescent transfection did not significantly alter mechanical parameters. The results shown in Fig. 2.9.a and Fig. 2.9.b showed no significant differences.

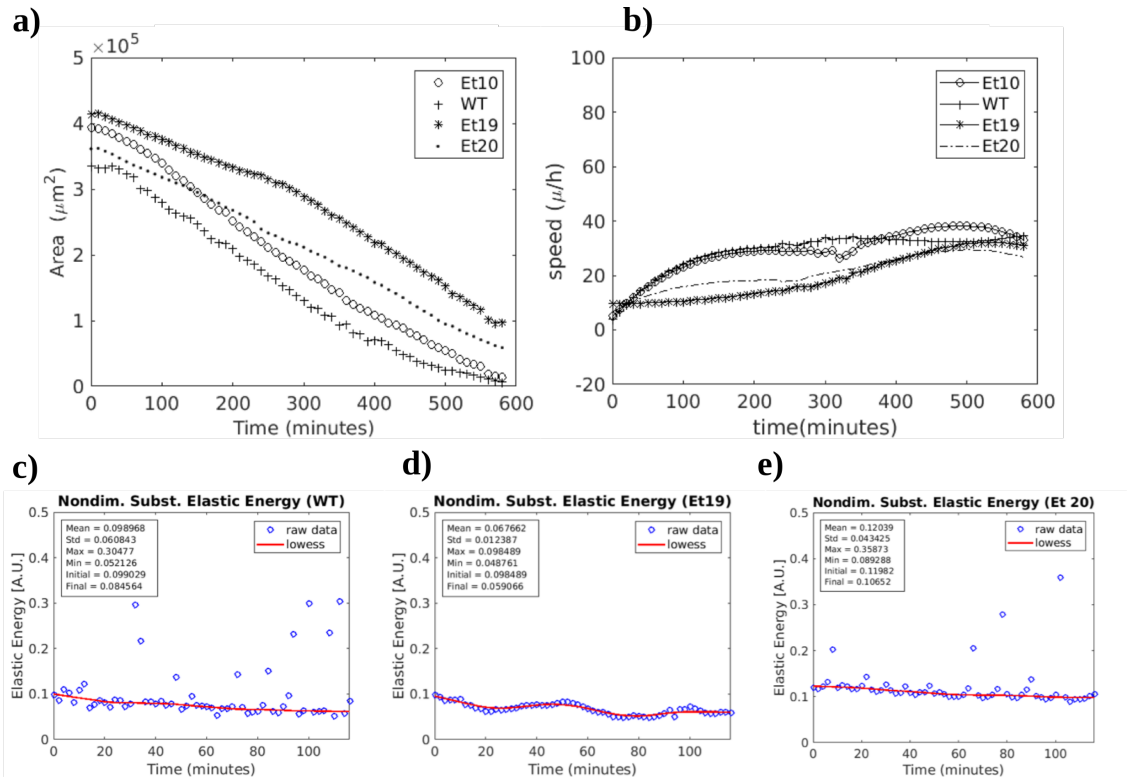

Figure 2.9: Migration assays and Traction Force (TFM) quantification for the transfected cell lines. a) Comparison of speed of gap closure for circular wounds of 1mm of diameter. b) Quantification of average speed of migration. c-e) Traction Force (TFM) quantification of strain energy exerted on the substrate by cell lines.

Traction force quantification

After migration assays showed no significant mechanical differenfes between strains, we decided to complete the mechanical phenotyping by conducting a series of Traction Force Microscopy (TFM) experiments in monolayers seeded on top of collagen-coated linearly elastic polyacrylamide gels and quantify the dynamics of the strain eenergy in the substrate as a proxy for the force exertion in each case [27].

As shown in Fig. 2.9.c-e, no significant differences were found between celllines contained in our short list.

2.3.2 Epithelial monolayers are able to climb obstacles through integrin adhesion with preserved front-rear polarity

In order to investigate the behavior of epithelial cells when they interact with obstacles in three dimensions we coated PDMS-fabricated pillars with different proteins or non-fouling polymers to engage certain proteins or prevent adhesion respectively.

We initially imaged a monolayer trying to self-heal [5] in a large circular wound assay, that contains a collagen-coated obstacle in the middle (Fig. 2.10.a). After the monolayer closed the wound, we observed the epithelial layer climbing in the vertical direction without an apparent change in polarity. Fig. 2.10.b-d shows a clear migratory phenotype preceded by an initial phase of crowding that results in several layers of epithelial cells.

We also performed SEM imaging on epithelial monolayers interacting with our microfabricated PDMS rods with dimensions of the order of 1mm length, $\sim$10 μm wide and $\sim$70 μm tall. Results shown in Fig. 2.11 confirmed that MDCK monolayers are able to climb flexible obstacles and descend them to close the monolayer again, as shown in inset 2.11.b. We also observed an increased density of microvilli when cells are located on top of the microrod versus a reduced density in cells migrating on top of the glass coverslip, which indicates a mechanosensitive feature of this cell line [47].

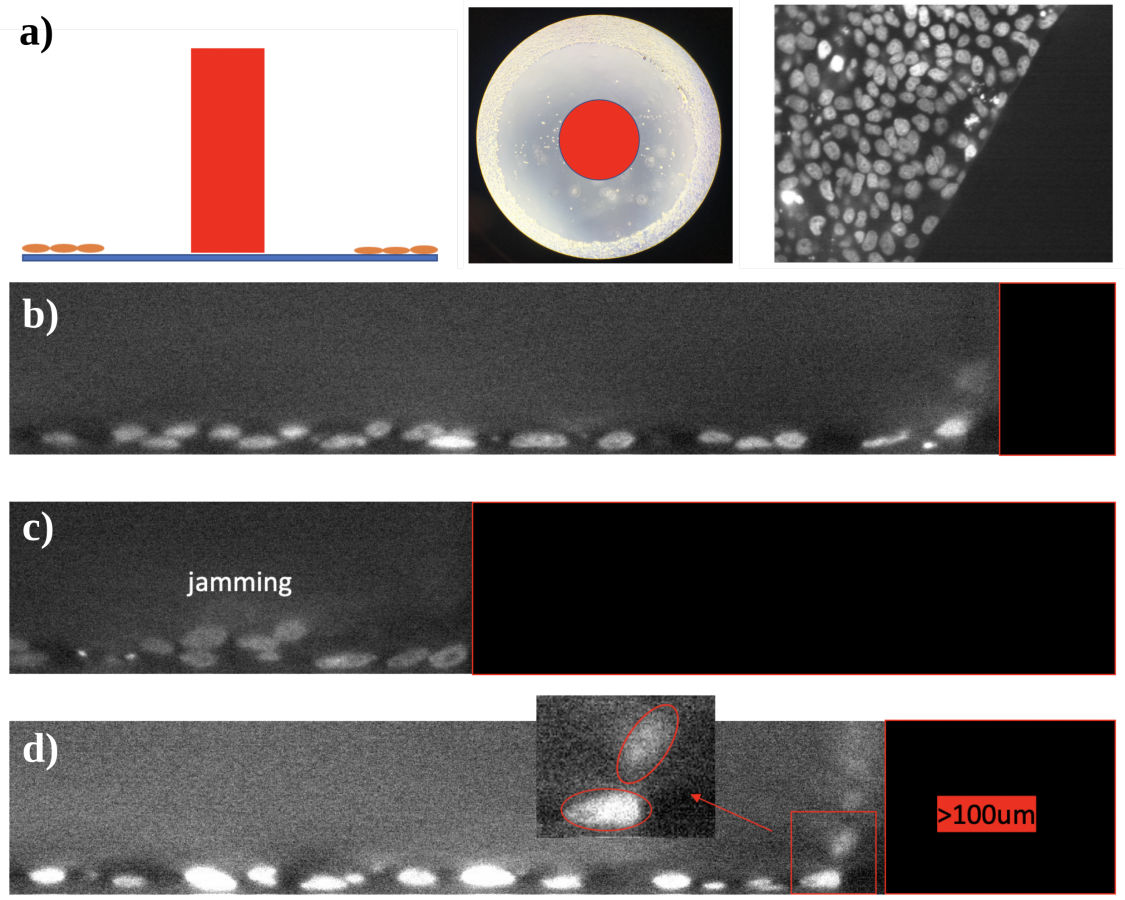

Figure 2.10: Interaction of epithelial monolayers with three dimensional Collagen coated PDMS pillars. a) Schematics of the assay with a circular wound and a PDMS pillar in the center leaving a sufficiently large gap for migration. b-d) Different reconstructed sections of the confocal 3D stack showing cell crowding and climbing through the pillar vertical distances over 100 μmm

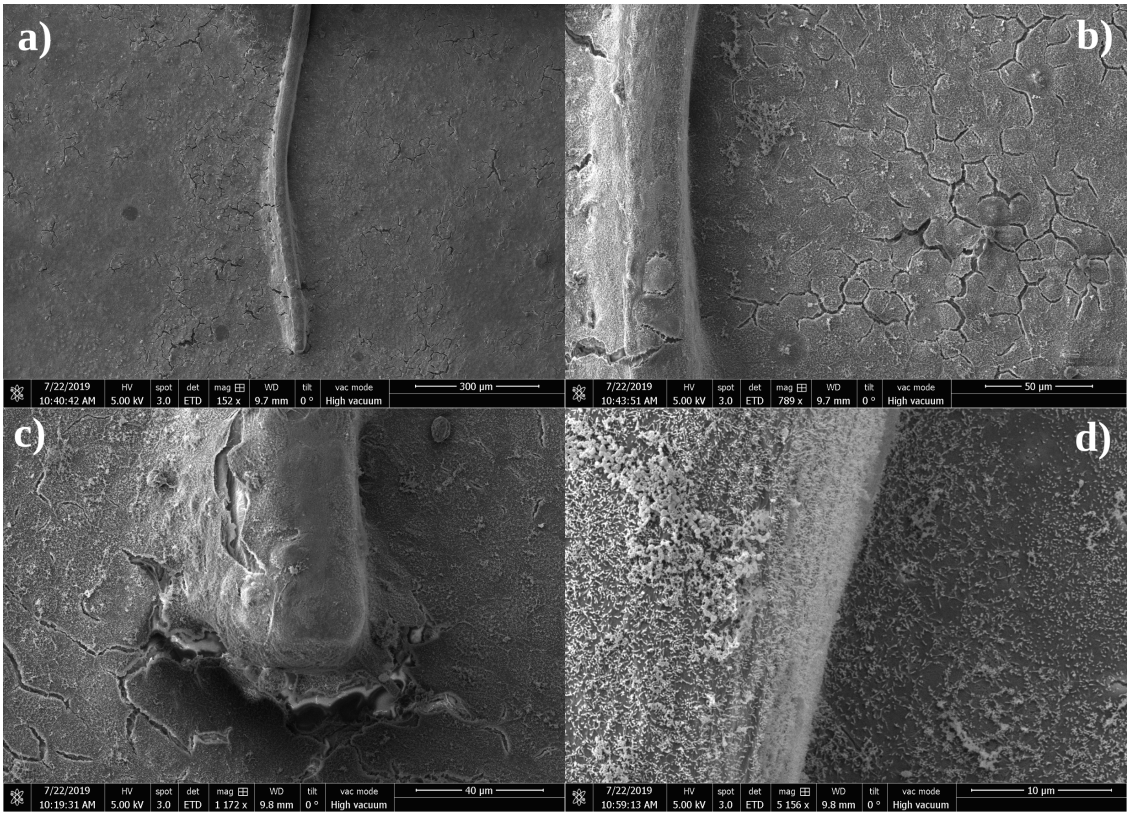

Figure 2.11: SEM images of the interaction of epithelial monolayers with collagen-coated flexible PDMS microrods. a) General view of the experiment with PDMS rod embedded inside the cell monolayer. c) Detail of directionality of migration (from left to right). c) Detail of the tip of the microrod. d) Detail of microvilli density on top of the rod and on the substrate.

2.3.3 Epithelial monolayers maintain tissue integrity in three dimensional environments

Further assays were investigated in which the coating was now based on the chimeric protein Fc:ECadherin, a cDNA sequence encoding the extracellular domain of mouse E-cadherin (amino acids 1-709) fused by means of a polypeptide linker to the Fc region of human IgG1 that is 6x histidine-tagged at the C-terminus and expressed in NSO cells [48, 49]. This way, a correct orientation of the protein is ensured via conjugation with a prior coating of protein A/G in the obstacle. We also investigated oiur three dimensional assay with non-fouling coatings, such as PLL-PEG, and the results are shonw in the las row of Fig. 2.13.

Fig. 2.12 shows a close-up view of our ECadherin-GFP expressing cell lines interaction with obstacles coated with collagen (a-b), PLL-PEG (c-d) and our ECadherin:Fc protein coating. Insets e and f in Fig. 2.12 show very clear how the coating engages endogenous expression of ECad-GFP in the cell line, meaning that the coating was successfully performed.

After that we went ahead and coated our three dimensional pillars with ECadherin and PLL-PEG (bottom row of Fig. 2.13), showing how, after several hours of experiment, the monolayer stops its migratory phenotype and prevents crowding as well, meaning that ECadherin is a necessary stop signal for epithelial cells to change from a migratory phenotype to a more homeostatic one [5].

When we examined the behavior of epithelial monolayers interacting with our flexible microrods we observed the shocking result of monolayers trying to maintain tissue integrity at all costs and forming non-adherent epithelial bridges [12, 13], even in three-dimensional configurations.

Figure 2.14.b shows how the epithelial monolayer is able to almost completely surrond the obstacle even when adhesions are prevented. However, the high level of tension resulting from these three-dimensional bridges, results in partial rupture of the monolayers.e

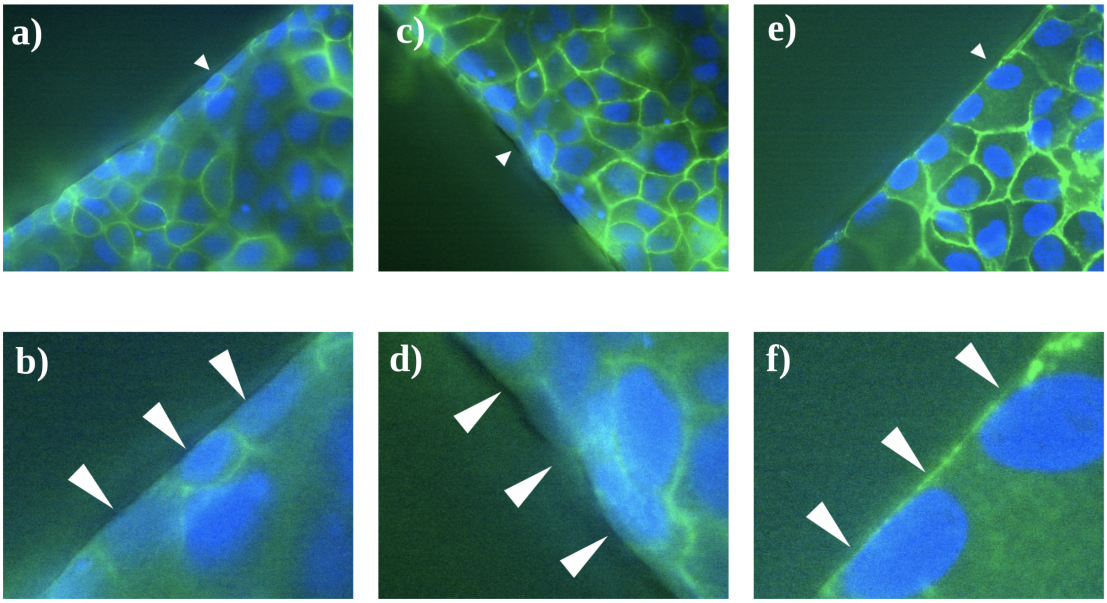

Figure 2.12: Fluorescent confocal images of PDMS pillars coated with: a-b) Collagen type I, c-d) PLL-PEG and e-f) ECadherin:Fc protein, and interacting with ECad-GFP expressing MDCK cells.

2.3.4 Piezo1 may regulate Contact Inhibition of Proliferation (CIP) through YAP/TAZ signaling

It has been long established that proliferation of many epithelial and endothelial cells is inhibited or slowed down at least by density, a phenomenon that has been traditionally attributed to cell-cell contact interactions [50]. However, even though several signaling pathways have been proposed to explain the process, the main mechanistic basis of Contact Inhibition of Proliferation (CIP) have been elusive so far and are still not clear.

Contact Inhibition of Proliferation and cell density

In order to investigate a possible mechanism to explain CIP, we started observing the natural process of crowding and stabilization of cell area in a confluemnt cell monolayer (Fig. 2.15). We seeded 150 thousand cells in a round coverslip and followed the process of mean area shrinkage with time for a period of 25h. After 20h is very clear that that the median cell area in the monolayer is not sginificantly changing and hence, proliferation is most likely

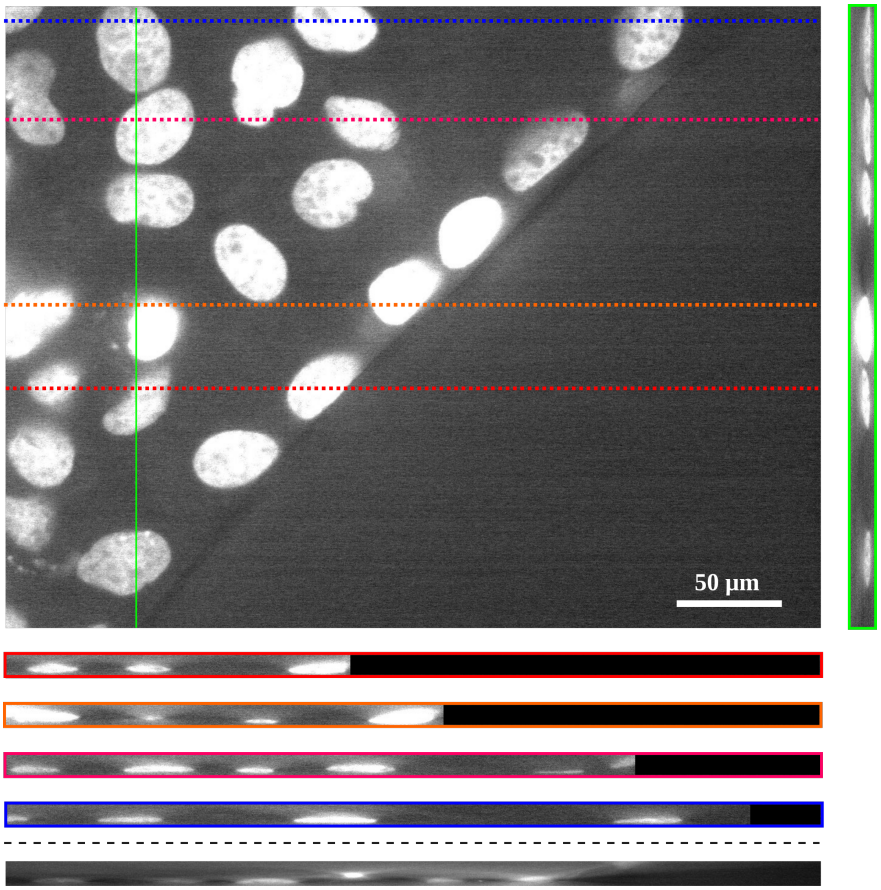

Figure 2.13: Fluorescent confocal images of PDMS pillars coated with ECadherin:Fc protein, and interacting with H2B-mCherry expressing MDCK cells. Last insert shows the same cells interacting with PLL-PEG coated pillars, exhibiting the same static and spread phenotype as when the pillar was coated with ECadherin:Fc protein

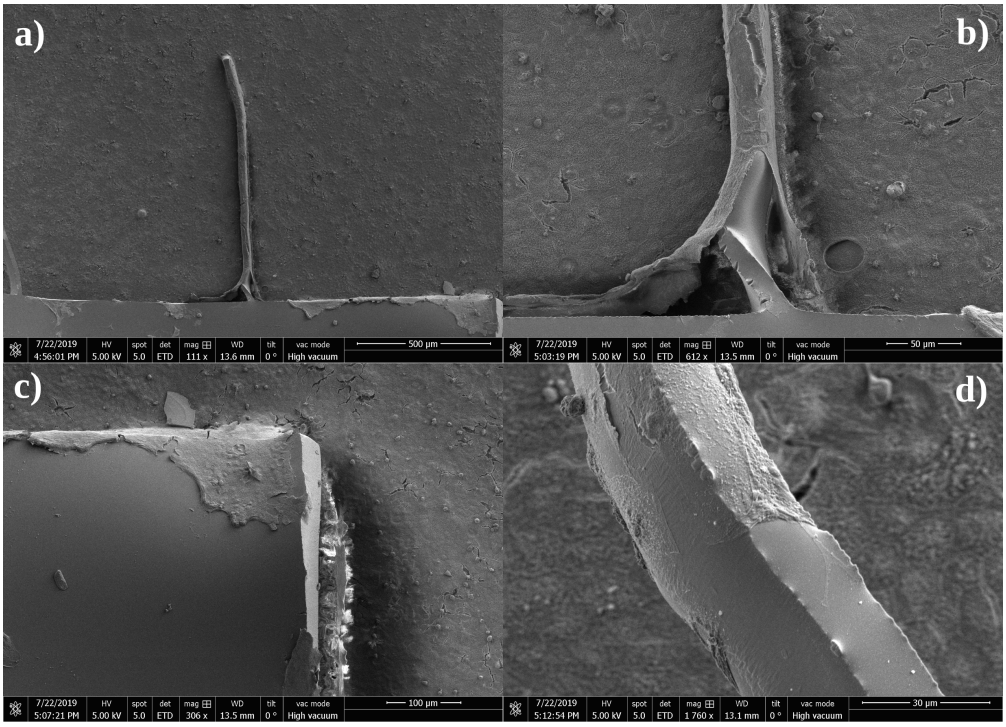

Figure 2.14: Scanning Electron MIcrographs (SEM) of MDCK cells climbing over non-adherent PLL-PEG coated microrods. a) General view of the assay. b) Detail of the high level of tension that originates when the cells climb three-dimensional obstacles and that results in monolayer fracture. c) Detail of the non-fouling base. d) Detail of the non-fouling micro-rod partially covered with MDCK cells.

inhibited or slowed down to maintain homeostasis within the tissue.

Since it has been previously reported that Piezo1 is intimately involved in cell proliferation under tension [51] and even apoptosis [52], we decided to investigatet he relation between the mechanosensitive ion channel Piezo1 and the Hippo pathway[53].

We performed migratory self-healing experiments with large wounds ($\sim$ 1x5mm) for our WT cells and our Piezo1 overexpressed cell lines and performed immunostaining for YAP de-localization from the nuclei [54].

Strikingly enough we observed a remarkably faster migratory behavior for Piezo1 overexpressed cell lines (Figs. 2.16.a and 2.16.d) along with a higher proliferative behavior, consistent with what was reported previously in [51].

Interestingly enough, when we performed immunostaining for YAP, we observed very different behaviors for our WT cell line and the ones with overexpressed levels of PIezo1, confirming the highly probable involvement of the mechanosensitive ion channel in CIP via the Hippo pathway.

We basically saw that in WT cell lines, the Hippo pathway is active, having YAP colocalize in the nuclei in sparse configurations and in the cytoplasm when the cells are in a dense configuration, slowing down proliferation in this latter case. However, in the case of overexpressed Piezo1 cell lines, we observed an abnormal behavior in the Hippo pathway, being YAP localized inside the nuclei at all times and consequently, not slowing down cell proliferation (Figs. 2.15 and 2.16).

2.4 Discussion and Conclusions

The methodology and preliminary results presented in this chapter opens the door to a mechanical characterization of the incredibly dynamical processes concerning epithelium development. The development of cell lines and mechanical phenotyping in a fully stochastic and automated way represents an incredible advantage paving the way for high throughput applications and screening.

A fully stochastic treatment of the fluorescent images facilitates adaptive thresholding,

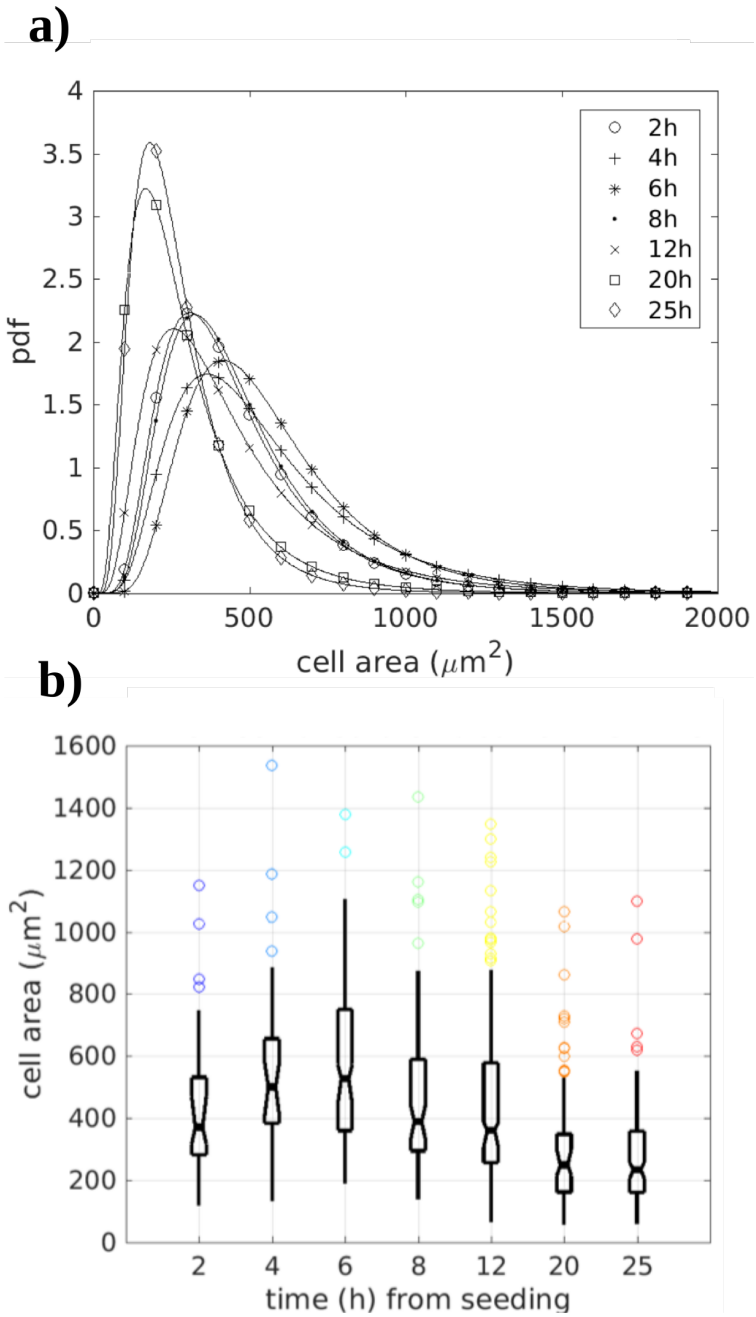

Figure 2.15: MDCK monolayer cell area dynamic evolution over a time course of 25 hours until reaching full confluency. a) Probability density function and its time evolution. b) Box plots and time evolution

efficient separation of background and in general, a more accurate description of the spatial dynamics occurring for every time point.

We have shown how epithelial cell lines are capable of preserving tissue integrity in

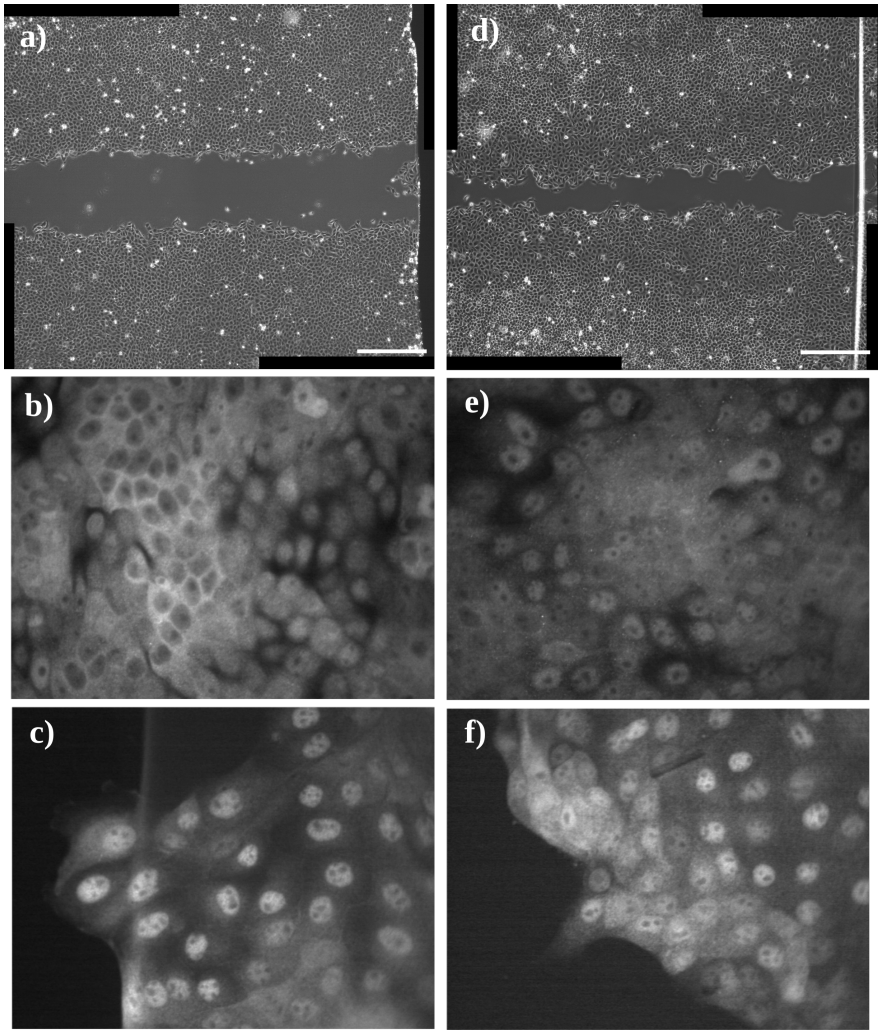

Figure 2.16: Piezo1 may regulate Contact Inhibition of Proliferation (CIP) through YAP/TAZ signaling. a) Bright field image of epithelial self-healing with H2B-mCherry MDCK cells. b) YAP immunostaining in H2B-mCherry MDCK cells in a dense configuration showing nuclear delocalization. c) YAP immunostaining in H2B-mCherry MDCK cells in a dense configuration showing nuclear colocalization. d) Bright field image of epithelial self-healing with H2B-mCherry+mPiezo1-IRES-eGFP MDCK cells. e) YAP immunostaining in H2B-mCherry+mPiezo1-IRES-eGFP MDCK cells in a dense configuration showing nuclear colocalization. f) YAP immunostaining in H2B-mCherry+mPiezo1-IRES-eGFP MDCK cells in a sparse configuration showing nuclear colocalization.

three-dimensions in extreme circumstances, withstanding high levels of intracellular tension that often results in rupture of the monolayer. The interaction of epithelial layers with rigid and flexible obstacles coated with ECM proteins represent a simple but efficient strategy to explore tissue dynamics in relevant scenarios, where interaction with different ECM proteins

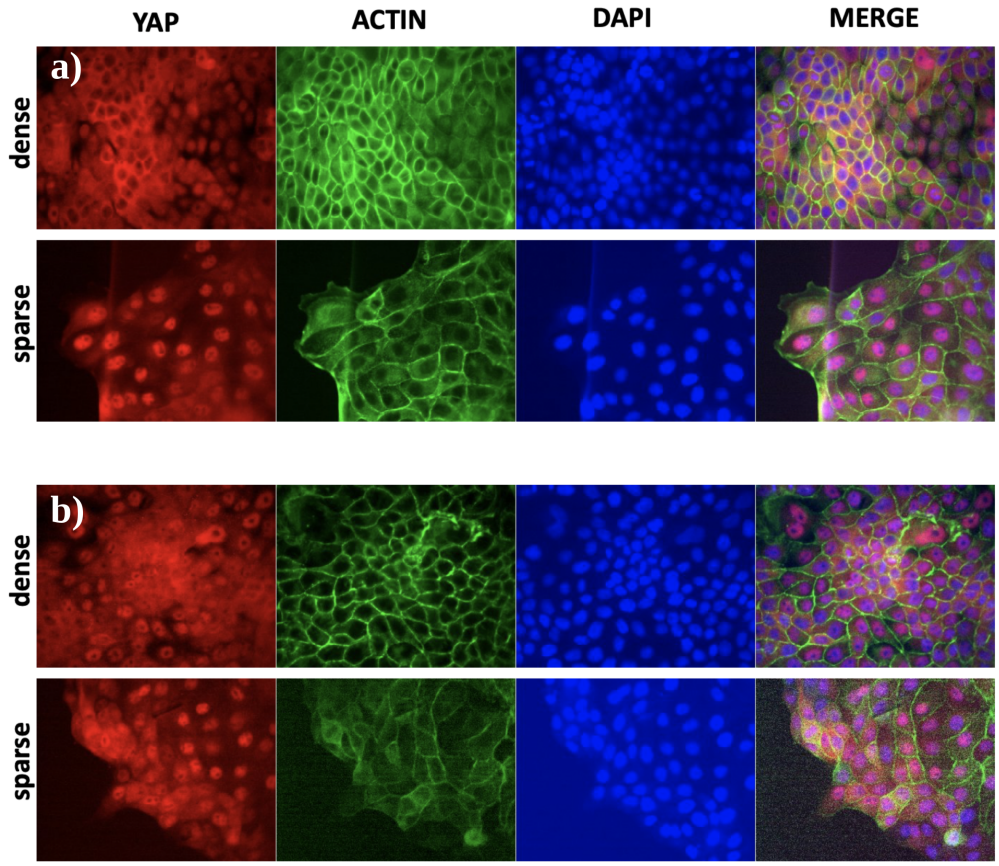

Figure 2.17: YAP immunostaining. a) MDCK H2B-mCherry cell line b) MDCK H2B-mCherry+mPiezo1-IRES-eGFP cell line

may occur. In particular, we have shown evidence of epithelial monolayers climbing obstacles through integrin adhesions and with preserved cell polarity.

The formation of three-dimensional bridges follows previous results introduced in two-dimensional stripes coated with ECM via microcontact printing and that showed how epithelium is able to withstand high levels of tension in order to preserve integrity [12].

We have also put forward the hypothesis of Piezo1 as a key regulator of Contact Inhibition of Proliferation via the Hippo pathway. Even though several mechanisms have been previously proposed to explain CIP [50] in a mechanistic way, there are still inconsistencies that have precluded a full explanation of the phenomenon. We have investigated the role of the mechanosensitive ion channel Piezo1 as a key regulator in the process.

2.5 Acknowledgements

Chapter 2, in part is currently being prepared for submission for publication of the material. Criado-Hidalgo, Ernesto; Yeh, Yi-Ting; del Álamo, Juan C.;Lasheras Juan C. The dissertation author was the primary investigator and author of this material.

Chapter 3

Fabricating biocompatible polyacrylamide microbeads for cell-generated mechanical force quantification via photoinitiated polymerization

3.1 Introduction

There is increasing evidence on the importance of force exertion as a part of cellular behavior as well as being a critical factor in a number of processes ranging from cell division, cell locomotion and normal and diseased physiological functions at the cell, tissue and organ level. Mechanical forces have been known to influence or even determine embryonic development [21], cancer progression [55] or even stem cell differentiation [56] for more than a decade now. However, the specific physical and molecular mechanisms by which these forces, exerted on surface-adhesion receptors [57], are able to trigger gene expression and affect cellular function is far from being completely understood.

Several studies have been published in the past few years to try and come up with a diverse set of strategies to quantify isotropic and anisotropic mechanical forces in living

tissues. One of the first systems used to quantify local traction variations in living embryonic tissues was based on tracking fluorocarbon oil droplet shape deformations [15, 58], whose physical properties are well known and characterized. With this method, anisotropic normal stresses can be measured and quantified by accurately determining the droplet shape and its separation from the zero-stress spherical shape, through the Young-Laplace's equation or balance [59]. However, this methodology can not measure or quantify isotropic normal stresses nor shear, due to the liquid nature of the force probes. It also requires a precise control of the surface chemistry of the droplets to prevent surrounding tissues from interacting with the highly deformable liquid interface to the point of rupture and posterior internalization of the surfactant or oil into the tissue.

Some other methodologies have tried to come up with elastic force probes typically based on quantifying the deformation of hydrogel micro-droplets with known mechanical properties [17, 44, 60]. However, they still show important limitations that prevents them from becoming a standardized methodology in the three dimensional arena of traction force quantification [30]. In particular, they either require complicated setups for the production of droplets and superresolution imaging techniques that prevent high-throughput implementation and usability in non-specialized laboratories or rely on materials with a limited range of mechanical properties, that limits their adaptability for a wide range of biological or physiologically relevant scenarios.

Consequently, there is still a significant lack of methodologies and techniques to fully characterize and properly quantify three dimensional stresses in living tissues, in an easy and reproducible manner and with a wide range of applications.

To address this lack of quantitative methods in the three dimensional setting we introduce in this chapter a strategy and workflow to generate photopolymerized hydrogel microdroplets with tunable mechanical properties and custom surface chemistry in a high throughput manner using in-house manufactured microfluidic devices. These hydrogel microdroplets can contain fluorescent particles or tracers to allow quantification of their deformation in 3D through three dimensional image correlation techniques such as particle image velocimetry (3D-PIV) [61].

Our preliminary results show feasibility of the proposed technology and pave the way to a new high-throughput pipeline and methodology of three dimensional force quantification in living tissues.

3.2 Materials and Methods

3.2.1 Microfluidic devices design and fabrication

A series of in-house designed and manufactured polydimethylsiloxane (PDMS) microfluidic devices were used to manufacture and collect the hydrogel microdroplets [62].

In order to produce monodisperse microdroplets of a PolyAcrylamide (PAAm) solution based hydrogel we relied on the very well characterized flow focusing microfluidic technology [63–66]. To further improve the monodispersity of the resulting droplets we used a series of consecutive T-shaped junctions to precisely break droplets into smaller sizes exploiting the Rayleigh-Plateau instability as suggested in [67]. A schematic of this device is depicted on Fig. 3.1.

Design

The initial design to generate the mask for the device used to produce spherical hydrogel particles in the micrometric range was generated using SolidWorks (Dassault Systèmes SolidWorks Corporation, Waltham, MA).

Photolitography

Microfluidic devices were manufactured using soft lithography [32]. The master device for the microchannel microfluidic device was fabricated in a sequential manner initiated by applying a coating of MCC Primer 80/20 (Microchemicals, Westborough, MA) spin coated at 3000rpm, accelerating at 1000rpm/s and with a duration of 30 seconds into a 4 inch single side polished silicon wafer (University Wafer, South Boston, MA). Shortly after, a first layer of positive photoresist AZ-12XT-20PL-10 (Microchemicals, Westborough, MA) was also spin coated on top of the primed silicon wafer at 500rpm accelerating at 100rpm/s for 10 seconds.

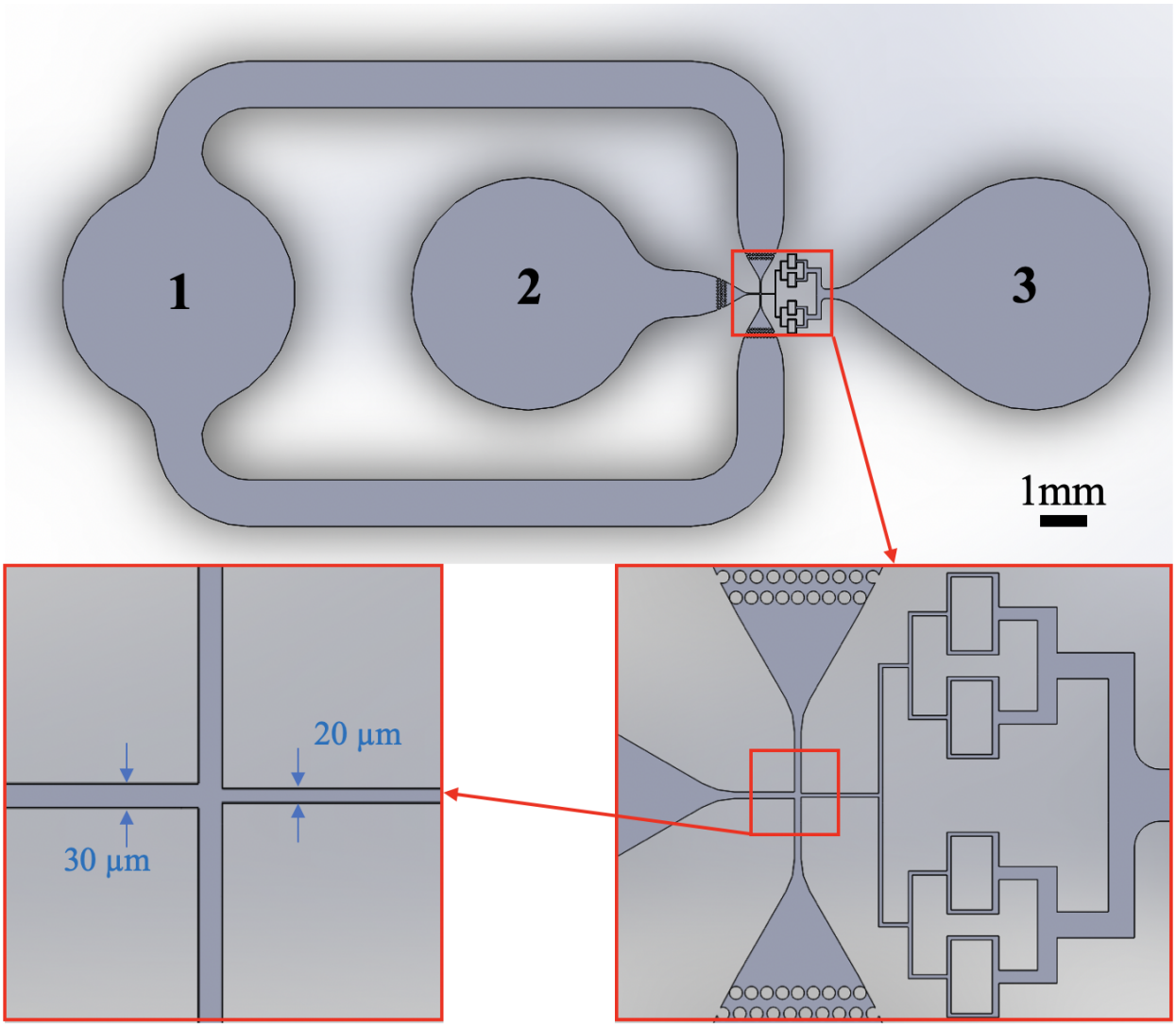

Figure 3.1: Schematic of the microfluidic device used to produce the microdroplets via emulsification of water-oil solutions. [1]: Inlet of the oil phase. [2]: Inlet of the water phase. [3]: Outlet of the device where the produced PAAm beads are recollected for further processing. The first inset depicts a detailed view of the consecutive T-shaped junctions for controlled droplet breakup. The inset on the lower left side of the figure shows a detail of the flow focusing region, where the water phase meets the oil phase and emulsification occurs.

A second layer was spin coated on top of the first one at 750rpm accelerating at 300rpm/s for 30 seconds this time. After a short soft bake at 110^{o}C for 2 min, we exposed (250mJ/cm2) the sample under a 375 nm laser using a MLA150 maskless aligner (Heidelberg Instruments Mikrotechnik GmbH, Germany) fed with the drawings of our device. A post-exposure bake of 1 min at 90^{o}C was performed and the features were obtained by developing the sample for 2 min using AZ-300MIF (Microchemicals, Westborough, MAs). Two 1 min steps of deionized water rinsing were performed to clear the sample from residues. Profilometry measurements using a Dektak 150 surface profiler (Veeco Instruments Inc. Plainview, NY) confirmed the expected thickness of 20μm. Afterwards, the wafer was passivated with tridecafluoro-1,1,2,2-tetra-hydrooctyl-1–1trichlorosilane (Gelest, Morrisville, PA) for 15 min inside a vacuum chamber to prevent PDMS adhesion to the wafer in the casting phase of the manufacturing process.

PDMS casting and bonding to substrate

PDMS replica of the device was made by carefully casting a previously degassed (during 30 min) mixture of the PDMS oligomer and crosslinking agent (Sylgard® 184, Dow Corning Inc. Midland, MI) in a 10:1 (w/w) proportion on the passivated silicon wafer. The sample was then cured at 65^{o}C overnight. The next day the master was peeled off the wafer, cut into several single devices and the inlet and outlet holes were punched (2.5 mm) with a biopsy puncher (Miltex, Integra Lifesciences, Plainsboro Township, NJ). Finally, we activated the surface of both the bottom coverslip (Corning, 24x60 mm and thickness 1.5 mm) and PDMS chip under a UV ozone lamp (Model 30, Jelight Co. Irvine, CA) for 4 min with an oxygen inflow of 0.2 lpm and bonded them together at 65^{o}C (to facilitate thermal bonding) for a minimum of 4 hours before they were ready to be used.

3.2.2 PolyAcrylamide microdroplets generation

PolyAcrylamide pre-gel solution and photoinitiator

The pre-gel solution was prepared by mixing 25 μL of 40 % Acrylamide (MilliporeSigma,Burlington, MA), 30 μL of 2% Bis-Acrylamide (MilliporeSigma,Burlington, MA), 3 μL of 2% 0.2 μm carboxilated FluoSpheres (Invitrogen, Carlsbad, CA), 20 μL of 20mM Lithium phenyl-2,4,6-trimethylbenzoylphosphinate (LAP, Sigma-Aldrich, St. Louis, MO), a water soluble, cytocompatible, Type I photoinitiator for use in the polymerization of hydrogels or other polymeric materials, and 122 μL of deionized water to a total volume of 200 μL that yielded gels of ∼9kPa. According to the desired hydrogel stiffness the proportion of Acrylamide to Bis-Acrylamide can be re-adjusted [30]. Afterwards, we kept the solution always cold (∼ 4^{o}C) inside an amber UV-protected 1.5 mL microcentrifuge tube (Eppendorf®, Hauppauge, NY), and degassed the pre-gel solution for one hour inside a vacuum chamber to prevent gelation inside the syringe while running the experiment.

Droplet production via inverse emulsification of water-oil mixtures inside the flow focusing microfluidic device

The oil phase was prepared by mixing the surfactant oil Krytox® 157 FSH (DuPont, Midland, MI) (10% w), a functionalized version of the DuPont series of Krytox® fluorinated oils that acts as a surfactant [68], into HFE 7500 Novec Engineered Fluid (3M, Maplewood, MN). Afterwards, both pre-gel and oil solutions were added to different 1 mL syringes and connected to their respective inlets in the microfluidic device using PTFE tubing (1/32" ID and 3/32"OD). Flows inside the device were controlled using two syringe pumps (NE-300 and NE-4000, New Era Syringe Pump). Flow rates were adjusted according to devices dimensions, desired droplet size and droplet generation frequency. For a typical droplet size of ∼35 μm, we used a channel width of 30μm and flowrates of 60/20 (Oil/Pre-gel) μL/h. The steady state was typically achieved after 15 min and the device was left running for a minimum of 3 hours while droplets were being collected in a 1.5 mL microcentrifuge tube (Eppendorf®, Hauppauge, NY).

Droplets collection and polymerization

After the device was running for a few hours, a sufficient amount of droplets were generated and collected directly from the outlet of the microfluidic device inside an amber UV-protected 1.5 mL microcentrifuge tube (Eppendorf®, Hauppauge, NY) filled halfway with Phosphate Buffered Saline (PBS, Sigma-Aldrich, St. Louis, MO). We then transferred the solution containing the droplets into a regular transparent microcentrifuge tube and polymerized them by exposing the tube to UV (302nm) light with a benchtop transilluminator (UVP, Analytik Jena US LLC, Upland CA) for 15 minutes.

Polymerized hydrogel microbeads recollection

Since the HFE 7500 fluid has a density of 1614 kg/m^3 [69], the oil phase tends to accumulate in the upper part of the microcentrifuge tube, which facilitates removal of supernatant oil phase from the PBS solution, while the polymerized droplets accumulate at the bottom of the microcentrifuge tube. Once polymerization was completed, the supernatant oil phase was carefully removed with a pipette tip and the remaining solution containing microbeads was supplemented with 1 ml of 20% v/v of PFO (1H,1H,2H,2H-perfluoro-1-octanol 97 %, Sigma-Aldrich) in Novec 7500 oil was added for 3 h to remove the surfactant from the droplets. Right after, the solution was centrifuged at 3500 rpm (Sorvall Legend RT, Beckman Coulter Inc. Indianapolis, IN), the supernatant oil phase was carefully removed and the beads were resuspended in PBS and stored at 4C. The centrifugation-resuspension step was repeated 3 times for improved purity of the resulting beads solution in PBS. Some other technologies [70] have been proposed to efficiently extract the oil phase from the generated droplets and could potentially be incorporated into this protocol.

Surface activation and coating with protein of interest

Surface activation of hydrogel beads for protein conjugation was done following the standard procedure for planar PolyAcrylamide gels [30] . First beads were pelleted by centrifugation at 3500rpm and then 1 mL of 0.2mg/ml Sulfo SANPAH (Thermo Fisher Scientific,

Waltham, MA), a heterobifunctional protein cross-linker used to covalently bind proteins to polyacrylamide substrates, was added to the microcentrifuge tube. We exposed the sample under UV light (254nm) for 7 minutes followed by a centrifugation step and posterior wash with PBS 1X. This process was repeated twice. The N-hydroxysuccinimide ester in sulfo-SANPAH can then react with the primary amines of proteins to complete the attachment of proteins to the surface of the gel.

We then proceeded to label Fibronectin (FN, Sigma-Aldrich, St. Louis, MO) with Fluorescein Isothiocyanate (FITC, Sigma-Aldrich, St. Louis, MO). We first prepared a solution of 1 mg/ml of FN in 0.1 M sodium carbonate buffer, pH 9. We then dissolved the FITC in anhydrous Dimethyl Sulfoxide (DMSO, Sigma-Aldrich, St. Louis, MO) at 1 mg/ml. For 1 ml of protein solution, we added 50 μL of FITC solution, very slowly in 5 μL aliquots while gently and continuously stirring the protein solution and incubated the reaction in the dark for at least 8h at 4 °C. In order to separate the conjugated FITC-FN from the FITC residue, we dialyzed the sample using Slide-A-Lyze™ Dialysis Cassettes with a molecular weight cut off 20,000 to 50,000 and stored the conjugate at 4°C in the column buffer in a light-proof microcentrifuge tube.

To bind the conjugated FN-FITC with the activated polyacrylamide beads, we incubated the beads in a solution containing 50 μ g/mL of the protein conjugate in PBS at 37 °C for a minimum of 3 hours. After this step, the beads are cell-compatible and ready to use.

Fabrication of polyacrylamide microbeads by inverse emulsification via vortex mixing

Inverse emulsification of the PAAm pre-gel solution was performed dissolving 50 μL of the pre-gel solution in 500 μL of HFE 7500 Novec Engineer Fluid (3M, Maplewood, MN) containing (10% w) of the surfactant Krytox® 157 FSH (DuPont, Midland, MI) inside a 1.5 mL Eppendorf tube. After that, the mixture was vacuumed for 15 min and subsequently vortexed for 1 min at maximum speed using a vortexer [71]. Right after, the Eppendorf tube was directly exposed to UV (302nm) light with a benchtop transilluminator (UVP) during

15 minutes to allow polymerization. Once polymerization was completed, the supernatant oil phase was carefully removed with a pipette tip and the remaining solution containing microbeads was supplemented with 1 ml of 20% v/v of PFO (1H,1H,2H,2H-perfluoro-1-octanol 97 %, Sigma-Aldrich) in Novec 7500 oil was added for 3 h to remove the surfactant from the droplets. Right after, the solution was centrifuged at 3500 rpm (Sorvall Legend RT, Beckman Coulter Inc. Indianapolis, IN), the supernatant oil phase was carefully removed and the beads were resuspended in PBS and stored at 4C. The centrifugation-resuspension step was repeated 3 times for improved purity of the resulting beads solution in PBS.

The subsequent surface activation and conting with protein of interest were performed in the same manner as described in previous sections.

3.2.3 Planar PolyAcrylamide Gels Fabrication

Collagen-coated PAAm gels of $\simeq 20$ μm thickness and 12 mm in diameter were prepared as cellular substrates as previously described by our group [27, 28]. Basically we initially we prepared squared 25 mm coverslips by activating them inside a UV ozone lamp (Model 30, Jelight Co. Irvine, CA) for 10 min and then coating them with a 1M solution of NaOH in deionized (DI) water for 5 min. After this step, we washed out the NaOH solution, rinsed the coverslip with DI water twice and completely dry it using a vacuum line. We then totally covered the surface of the coverslip with a solution of 3% (v/v) (3-Aminopropyl)triethoxysilane (APTES, Sigma-Aldrich, St. Louis, MO) in ethanol for 20 min at room temperature. After this step, we carefully washed the surface of the coverslip with pure ethanol and soft baked the coverslip for 5 min at 37 °C. The amino-silanated coverslips remain usable typically for a 48 hours period. In case a stronger bond between the coverslip and the PAAm gel is required, this can be achieved by including an extra step consisting of covering the amino-silanated coverslips with 0.5% (v/v) Glutaraldehyde (Sigma-Aldrich, St. Louis, MO) in Phosphate Buffered Saline (PBS) for 30 min at room temperature. This mild and relatively fast reaction (Schiff base reaction) between compounds containing aldehydes (or ketones) and amino groups, result in covalent, and hence stronger, imine groups (Schiff base) that will bind the PolyAcrylamide gel in a stronger manner [29, 30].

Once the coverslips were ready, we prepared the pre-gel solution with a mixture of 5% Acrylamide and 0.3% Bisacrylamide (8.7 kPa, [30]) and seeded them with 0.03% carboxilated FluoSpheres (Invitrogen, Carlsbad, CA). We then mixed the solution with 1% (v/v) of 10% (w/v) Ammonium Persulfate (APS, Sigma-Aldrich, St. Louis, MO) in DI water and N,N,N',N'-Tetramethyl ethylenediamine (TEMED, Sigma-Aldrich, St. Louis, MO) to initiate the polymerization reaction. We then pipetted 3 μL of the pre-gel solution on top of the silanized coverslips, placed a round 12mm coverslip on top, and immediately inverted the mixture and let the gel polymerize for 30 min. During polymerization, the microspheres migrated to the bottom (i.e., the free surface of the gel). We posteriorly used a 0.15 mg/mL Sulfo-SANPAH (Thermo Fisher Scientific, Waltham, MA) solution in DI water to cover the gels, followed by UV activation to facilitate the cross-linking of 125 μg/mL of rat tail Collagen Type I (Dow Corning Inc. Midland, MI) to the surface of the polyacrylamide gels. The gels were incubated for 1 hour at 37 °C and then equilibrated with medium for at least 3 hours. We measured the thickness of the substrates by locating the top and bottom planes of the gel and subtracting their vertical positions as previously described [28]. The Poisson's ratio of the gel was measured to be 0.46, following an elastographic traction force microscopy method previously developed by our group [31].

3.2.4 Cell Culture

Human vascular umbilical endothelial vein cells (VECs) (purchased from Cell Application, San Diego, CA) were cultured in medium M199 supplemented with 10% (vol/vol) endothelial cell growth medium (Cell Application , San Diego, CA), 10% (vol/vol) FBS (Lonza, Basel, Switzerland), 1% sodium pyruvate, 1% L-glutamine, and 1% penicillin– streptomycin (Gibco, Waltham, MA) until they formed a confluent monolayer on top of 10cm cell culture plates (Thermo Fisher Scientific, Waltham, MA).

After culturing the cells and prior to seeding them in the desired substrate, we aspirated the supernatant medium and washed 3 times gently with PBS. We then aspirate the supernatant completely and incubate the monolayer 2mL of Trypsin-EDTA Solution 1X for 5 minutes at 37 °C until the cells completely detach from the plate.

We aspirated and collected the 2mL of suspended cells in Trypsin-EDTA and suplemented the solution with 3mL of medium, to neutralize peptide cleavage. After this step, we centrifuged the sample inside a 15mL conical tube at 1000 rpms for 5 min to generate a pellet of cells. The supernatant was then aspirated and the cells were resuspended in 5 mL of fresh medium. After this step, the cells were ready to be seeded on the substrate.

We used a hemocytometer to count cells and seed for confluency ($\simeq$ 1E-7 cells/cm^2) on top of the collagen or fibronectin coated substrates.

Staining cytoplasm of adherent cells with fluorescent dye

Before proceeding to stain the cells, a working dye solution of the dye was prepared dissolve the lyophilized product (CellTracker™, Thermo Fisher Scientific, Waltham, MA) in high-quality Dimethyl Sulfoxide (DMSO, Sigma-Aldrich, St. Louis, MO) to a final concentration of 1 mM (1000X) solution. Next, we diluted the stock solution to a final working concentration of 10 μM in serum-free medium. The working solution was then warmed up to 37 °C.

Once the working solution was sufficiently warmed up, we removed the medium from the culture and gently added the pre-warmed CellTracker™ working solution. We then incubated the plate for 30 minutes inside the incubator. After that, we removed the working solution from the culture, washed very gently with PBS and gently added 10mL of warm medium to the tissue culture plate. The sample was then ready for imaging.

Schistosoma Mansoni eggs isolation and culture

Ethics Statement. Golden Syrian hamsters infected with the NMRI (Puerto Rican) isolate of S. mansoni were obtained from the Biomedical Research Institute (BRI), Rockville, MD [72]. Vertebrate maintenance and handling at the Animal Care Facility were in accordance with protocols approved by the Institutional Animal Care and Use Committee (IACUC) at the University of California San Diego.

Eggs were recovered from livers of 3-5 week-old infected hamsters [73]. Mature and immature eggs were separated at the second Percoll column step in the protocol. In brief,

eggs from the first Percoll column were layered on top of the second Percoll column, prepared by mixing 2.5 ml Percoll with 7.5 ml of 0.25 M sucrose. Following centrifugation at 800 x g for 10 min. the immature eggs were removed at the interface and the mature eggs were collected from the bottom of the column. The two egg fractions were washed 3-5 times with M199 culture medium, centrifuged at 400 rpm for 3 min., removing any remaining Percoll and tissue debris. The immature eggs were further washed by gravity with M199 culture medium, any mature eggs present will settle at the bottom of the tube before the immature eggs. Immature egg enrichments typically contained 5-10% of the mature stages and egg shells whereas mature egg fractions contains less than 5% of immature eggs, as observed by microscopic examination.

Egg secreted products (ESP) of mature and immature eggs were harvested as described in [74]. Hatch assay of post-culture mature eggs confirmed that the eggs contained viable miracidia.

3.2.5 Microscopy and Imaging

Phase contrast microscopy

A Leica DMI 6000B inverted phase contrast microscope (Leica Camera, Wetzlar, Germany) controlled by a dedicated workstation running the open source μ-Manager software (Vale lab, UCSF) was used for image acquisition. The microscope was equiped with a Zyla 3-Tap Enclosed C-mount 16 bit camera (Andor Technology, Belfast, UK) and a Mercury Short-Arc Discharge Lamp with Reflector with emission filters to generate excitation light in the usual DAPI, FITC, TRITC, and CY5 wavelengths.

We typically acquired time-lapse image sequences at 10 and 100 frame per second (fps) in bright field (BF) and fluorescent field (FLUO) with 10x, 20x and 40x lenses and exposures ranging from 10-20 ms (BF) and 100-200 ms (FLUO).

Confocal microscopy

Three dimensional z-stack bright field and fluorescent images of samples were taken using an Olympus IX81 confocal microscope (Olympus Corp. Tokyo, Japan) with a cooled CCD camera (Hamamatsu Photonics, Shizuoka, Japan), using Metamorph software (Molecular Devices LLC. San Jose, CA) and a 40× N.A. 1.35 oil-immersion objective. Following the acquisition, the sequences of z-stack images were analyzed using the software suite Volocity (PerkinElmer, Waltham, MA), which rendered some of the optical sections into 3D models.

Airy scan imaging and confocal data preprocessing

The higher resolution imaging for single beads study was performed on an enclosed Zeiss LSM 880 Confocal microscope (Carl Zeiss AG, Oberkochen, Germany) with superresolution capabilities under the fast Airyscan mode. A 40x water lens was used. For experiments solely related to characterizing PAAm microbeads shapes, a 200 μm stack with either 1.21 μm or 2.21 μm spacing was acquired. The in-plane calibration factors were 0.0824 μm/px and 0.123 μm/px, respectively. For every experiment, 4 different fluorescent channels were acquired: DAPI, FITC, TRITC and CY5. The duration of timelapse experiments varied. Each experiment was ended when a full reconstruction of the microbead of interest was obtained. Since the samples were already fixed and not motile, time steps were not a concern in these set of experiments.

Before performing any analysis on microscopy data from the Zeiss LSM 880 microscope, image stacks needed to be preprocessed at a local workstation. Raw Carl Zeiss Image (CZI) Airyscan output files from the Zeiss LSM 880 microscope underwent Airyscan post-processing using Zeiss's imaging software Zen Black. After Airyscan processing, these files were imported with Fiji [75] and then exported and saved as .TIFF hyperstacks. These .TIFF files could then be handled with Matlab (Mathworks, Natick, MA) for further manipulation and post-processing.

Scanning Electron Microscopy

To prevent the presence of any organic contaminants inside the Scanning Electron Microscope (SEM), we fixed the samples using a fixative buffer composed of 4% Paraformaldehyde (PFA, Biotium, Freemont, CA) supplemented with 2.5% of Glutaraldehyde (Sigma-Aldrich, St. Louis, MO) in Phosphate Buffered Saline (PBS). We first aspirated the medium in our samples, covered them completely with the fixative buffer and incubate overnight at 4 °C.

After overnight fixation, we aspirated and stored the PFA solution and cover the samples with PBS prior to serial dehydration. We then prepared a series of ethanol concentrations in DI water for dehydration of our samples (50%, 60%, 70%, 80%, 90%). We continued rinsing our samples with fresh buffer (PBS) and replacing the buffer solution with the lowest concentration ethanol solution (50%) and left for 15-20 minutes. We continued the process with increasing ethanol concentrations until we reached 100%, and repeated twice the last step of the serial dehydration process. The samples were then dehydrated and ready for drying.

To prevent collapse of biological samples due to surface tension, Critical Point Drying (CPD) was performed on all samples following dehydration using a Tousimis AutoSamdri 815A critical point dryer (Tousimis, Rockville, MD). Previously dehydrated samples were placed inside the CPD chamber with sufficient ethanol to completely cover the samples. The chamber was then sealed and cooled, as valves were opened letting liquid CO_2 in and venting ethanol out, until liquid CO_2 completely replaced ethanol. The chamber was then sealed again and slowly heated until the critical point was reached at about 1350psi and $\simeq$ 35 °C. The CO_2 was then slowly drained from the chamber as a gas, preventing surface tension damaging effects in the sample.

After CPD, the sample was ready for sputter coating. This process was performed on a Emitech K575X Iridium Sputter Coater. Basically the samples were introduced inside the sputtering chamber, vacuum was applied until the pressure reached $\simeq 10^{-2}$ mbar and the system was run at 85mA for 8 seconds yielding samples coated with a thin layer of iridium

and ready for SEM imaging.

Imaging was thereafter performed using a FEI Quanta FEG 250 SEM with environmental capabilities. Images were acquired at 1kV and with magnifications ranging from 441X to 16.77kX.

3.2.6 Image Processing

Image processing was performed using Fiji and ImageJ [39] as well as in-house developed Matlab scripts. Initially images were imported to the workstation through Fiji's Bioformat plug-in, converted into separate 16-bit tiff images and stored back as individual tiff images for each channel and z level. These separate files were then imported into Matlab for further processing. Images were normalized, cleaned up applying median and gaussian filters and contrast was equalized when needed through Contrast Limited Adaptive Histogram Equalization (CLAHE), for visualization purposes only [40].

Active contour segmentation of the microspheres was implemented [76] for three dimensional shape reconstruction through isosurfaces [77].

For the quantification of nanobeads spatial density maps, segmentation on two-dimensional images was performed by statistical separation of the region of interest from the background through a Gaussian Mixture Model [41] aimed at fitting two distinct distributions of pixel intensities. Once the background region was identified and ruled out, specific positions of individual nanobeads were computed using local maxima and weighted centroid approaches. Further refinement of the (x,y) position was achieved by using a radial-symmetry-based particle localization approach with subpixelar capabilities [42].

3.2.7 Atomic Force Microscopy quantification of mechanical properties of hydrogels

Hydrogels of different stiffness were prepared by mixing 40% Acrylamide (MilliporeSigma,Burlington, MA), 2% Bis-Acrylamide (MilliporeSigma,Burlington, MA), 20mM stock solutions of Lithium phenyl-2,4,6-trimethylbenzoylphosphinate (LAP, Sigma-Aldrich, St.

Louis, MO) and water in the appropriate concentration. Three different concentrations were tested based on the stiffnesses reported previously [30] using Ammonium Persulfate (APS, Sigma-Aldrich, St. Louis, MO) and Tetramethylethylenediamine (TEMED, Thermo Fisher Scientific, Waltham, MA) as initiators and accelerator of the polymerization reaction. Flat gels were prepared by filling a cylindrical cavity formed by two previously treated coverslips (20x20 mm2, Sigma Aldrich) and a circular stainless steel washer. This setup allowed us to have flat gels with an approximate thickness of 5mm hence preventing possible interference of the bottom substrate when performing nanoindentations. All samples were polymerized by exposing them to UV (302nm) with a benchtop transilluminator (UVP, Analytik Jena US LLC, Upland CA) for 1 minute. After this step, hydrogels were soaked in deionized water and kept at 4°C to prevent evaporation. All the measurements were carried out during the following couple of days to prevent aging of the hydrogels.

Elasticity of PAAm hydrogels was measured using a Scanning Probe Microscope (Veeco Instruments Inc. Plainview, NY) with a Nanoscope IV controller. Nanoindentation curves were obtained using a standard pyramidal tip cantilever (k=0.24N/m, DNP-10, Bruker Nano Surfaces, Goleta, CA). Due to the rather large error on the nominal spring constant value provided by the manufacturer of the probe, the Sader method was employed to try and narrow its value [78]. This method relies on the measurement of the resonant frequency, a quality factor of the cantilever, its dimensions and the properties of the fluid used.

In order to reduce the effect of adhesion forces and prevent evaporation, all experiments were conducted using a fluid cell, where the tip and the sample were covered by deionized water at room temperature. A topographical image of 5x5 μm^2 was captured for each gel and a minimum of 15 nanoindentations were performed. Curves were obtained by specifying the total movement of the piezo stage (750nm) and a maximum deflection threshold relative to the baseline of 35nm. Forward and reverse velocities were fixed at 50nm/s and the scan rate was set to 0.1Hz. After each sample was characterized, the deflection sensitivity of the cantilever was corrected by performing a nanoindentation curve on a silicon surface were no indentation was possible and consequently piezo movement of the stage and

cantilever deflection must be equal.

Young's modulus for the different samples was obtained using the NanoScope Analysis software (Version 1.5, Bruker Nano Surfaces, Goleta, CA). Tip half angle was set to 20^{o} as specified by the manufacturer. A linearized Sneddon [79] model and its correction for pyramidal tips [80] was used to fit our data.

3.3 Results

This section presents some preliminary results that illustrate the potential of the microfluidic platforms developed in this chapter. We fabricated biocompatible, monodisperse, and elastic PolyAcrylamide (PAAm) microspheres with a size range of 10–50 μm via a flow-focusing microfluidic device. Fluorescent nanoparticles of $\sim$200 nm in diameter were embedded in the microgels as a marker to quantify cell-induced deformation through Particle Image Velocimetry (PIV). Once the three-dimensional deformation field is available, the three-dimensional traction stress distribution inside the microdroplet can be reconstructed by solving the elasticity equation of equilibrium for a linear, homogeneous, isotropic three-dimensional material characterized by its Poisson's ratio [61]. We used superresolution imaging techniques to quantify and characterize the fluorescent nanobeads spatial distribution inside the polymerized microdroplets and compared with the distributions found in standardized planar hydrogels. We also successfully coated the spherical hydrogels with extracellular matrix (ECM) proteins and studied the interaction of human vascular endothelial cells with the microbeads, opening the door to a myriad of in vitro and in vivo force quantification applications in three dimensional settings.

3.3.1 Operation of the flow focusing microfluidic device and generation of pre-gel liquid microdroplets

Traditional emulsification techniques have used inhomogeneous extensional and shear flows to rupture droplets, however, this approach typically results in a large size polydispersity index of the resulting liquid droplets. For the production of relatively monodisperse

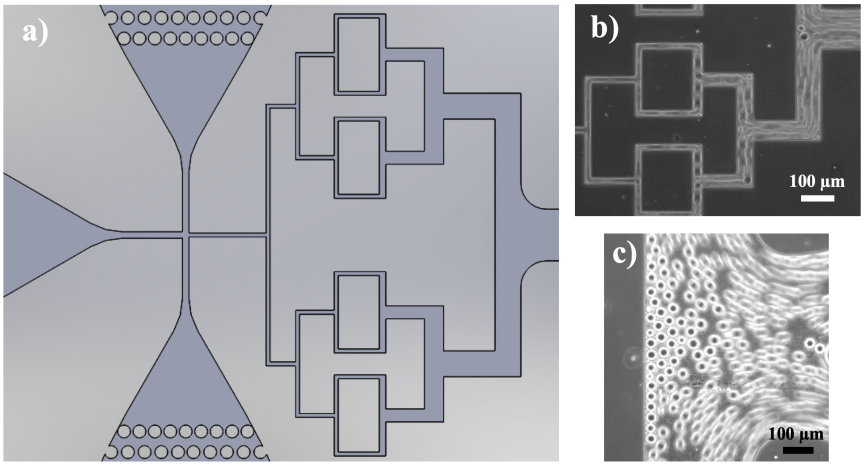

Figure 3.2: Flow focusing microfluidic device used to produce pre-gel microdroplets showing passive breakup at T junctions and homogeneous droplet distribution. a) Schematic of the device. b) Detail of the T junctions showing the passive breakup of droplets. c) Resulting monodisperse distribution of microdroplets produced inside the flow focusing device at the end of the passive breakup steps and prior to polymerization.

pre-gel PolyAcrylamide droplets we used a combined strategy consisting of a first step of flow focusing emulsification [63–66], followed by a series of T junctions in which geometrically mediated breakup of pre-gel droplets is achieved [67]. After this step, the size of the droplets is considerably reduced and can be very easily tuned adjusting the characteristic sizes of the junction of the oil and water phases (Fig. 3.1), the relation between flow rates and also the number of T junctions downstream the flow focusing stage of the device (Fig. 3.2). After pre-gel droplet formation, the resulting microdroplets were collected downstream and polymerized using UV light.

3.3.2 Size distribution of generated microdroplets inside the flow focusing microfluidic device

To characterize the size distribution of the microdroplets generated with our flow focusing device and evaluate the degree of monodispersity of the droplets that our current design was able to produce, we generated liquid droplets of our pre-gel solution using standard conditions of 30 μm wide channels for the oil and pre-gel solution phases, 20 μm wide collecting channel and flowrates of 60/20 (oil/pre-gel) μL/h, and compared against droplets

produced with a rapid but effective way of generating emulsified droplets of micrometric size using a recently developed processs based on inverse emulsification via vortex mixing [71]. The results shown in Figure 3.3, showing histograms of the droplets distributions in both cases, for 5 different fields of view sufficiently separated from each other, represent more than enough evidence of a much superior performance of our hybrid flow focusing device in terms of smaller size of the microdroplets (an average size of ~ 36 μm for our device VS $\sim$ 53 μm for the vortex mixing) as well as their monodispersity (the standard deviation in the case of our device is as small as $\sim 6\%$ of the mean while for the vortex mixing device this number skyrockets up to $\sim 45\%$ of the mean value). In addition, our microfluidic device can be easily tuned to produce smaller (or bigger) droplets just by adjusting the flowrates between the two liquid phases (oil and pre-gel solutions), without the need to restart the experiment (Figure 3.6 insert e).

3.3.3 Photoinitiated polymerization of pre-gel Acrylamide solution droplets

Once the microdroplets were produced inside the microfluidic device, the surfactant oil Krytox® 157 FSH prevented droplet coalescence by stabilizing the emulsion for a significant amount of time [81–83]. This permitted to efficiently collect and polymerize the liquid microdroplets by exposing them to UV (302nm) light with a benchtop transilluminator that triggered the polymerization reaction inside the droplets and collect them right after for posterior washing steps to remove the surfactant and the oil phase from the polymerized acrylamide microbeads.

In our pre-gel Acrylamide solution, we decided to use as a free radical source phenyl-2,4,6-trimethylbenzoylphosphinate or LAP, a highly efficient water soluble photoinitiator [84–86] and embeded carboxylated fluorescent nanoparticles as tracers (for Traction Force Microscopy). In order to test the polymerization efficiency of our microdroplets, we imaged them every 10 seconds for a period of time of ~ 2 minutes, searching for coherent internal movement of the fluorescent tracers. PAAm chains are nonfouling, meaning that adsorption of proteins to the gel or nonspecific binding of cell surface receptors is typically negligible

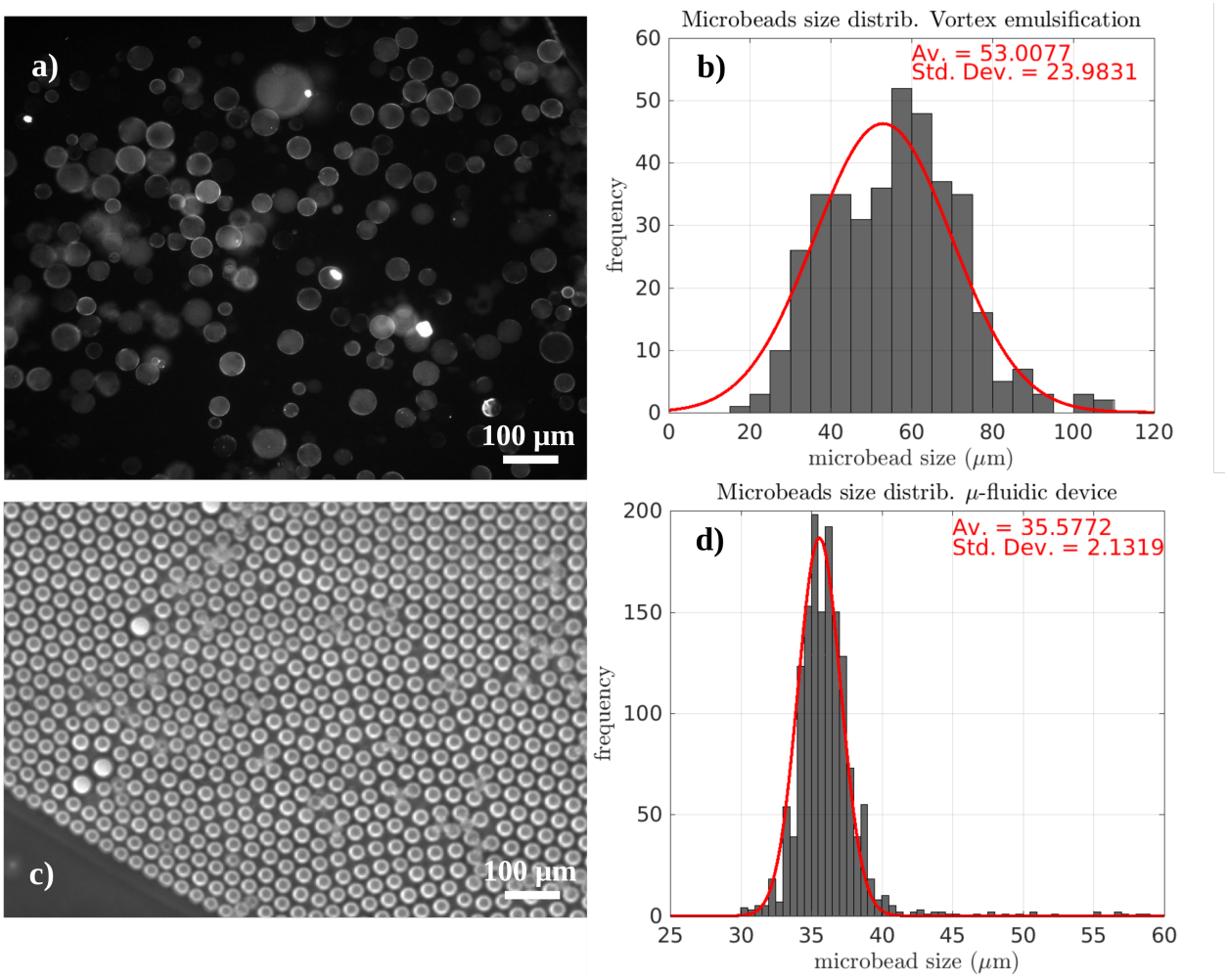

Figure 3.3: Size distribution of pre-gel droplets produced with a flow focusing microfluidic device VS droplets produced through inverse emulsification via vortex mixing. a) Fluorescent image of microdroplets containing fluorescent nanobeads and produced through inverse emulsification via vortex mixing. b) Statistical description of sizes of the liquid droplets produced via vortex emulsification. c) Bright field image of droplets collected and produced using our flow focusing microfluidic device coupled with T junctions responsible for geometrically mediated breakup of droplets. d) Statistical description of sizes of the liquid droplets produced using our microfluidic device.

[30], however, due to hydrolysis of some of the side amide groups, polyacrylamide chains can have some weak ionic properties. Since carboxylated nanobeads have a relatively high charge surface density, passive adsorption typically occurs between the nanobads and the linear polymer chains, hence immobilizing carboxylated nanobads to the gel's backbone. In addition to this ionic interactions, and far from the micrometric pore sizes of collagen gels with physiological collagen concentrations [87, 88], the typical pore sizes of PAAm gels in the range of interest for mechanobiology applications are on the order of 100 nm [89–92], which will contribute as well to efficiently trap and immobilize the fluorescent nanobeads inside the polymeric network.

Consequently, if the gel is sufficiently polymerized, coherent movement of the fluorescent beads is expected along with that of the entire gel or microbead, as opposed to the random brownian motion of fluorescent beads observed inside non-polymerized liquid droplets.

As shown in Fig. 3.4, when the pre-gel solution was not yet polymerized, random motion of the fluorescent nanobeads was evident on a maximum intensity projection image of all the images in the acquired timelapse (Fig. 3.4.b). Not surprisingly however, when the liquid droplets were polymerized under UV light (302nm) for 15 min, we observed coherent solid body movements in the fluorescent tracers inside the polymerized beads, indicative of a solidified polymeric structure with fluorescent nanobeads attached to the polymer backbone (Fig. 3.4.d). To further validate this methodology, we imaged for a longer period of time and compiled the maximum intensity projection image of all the timelapse (600 snapshots, one every 10 seconds), obtaining more compelling evidence of the coherent motion of the embedded fluorescent nanobeads.

More sophisticated strategies can be used to check the polymerization efficiency of the co-polymerization of acrylamide and bis-acrylamide (a vinyl addition polymerization initiated by a free radical-generating system), suchs as in situ dynamic photorheology [93] where the elastic and viscous moduli can be measured dynamically during photopolymerization or Fourier transform infrared spectroscopy (FT-IR) with attenuated total reflectance (ATR), that checks for the absorbance spectrum of polymerized PAAm chains [71], however,

our simple approach seems sufficient to demonstrate the efficient and satisfactory polymerization of our microbeads since photoinitiation of PAAm gels and other polymers such as PEG-diacrylate or N-acryloylmorpholine, using LAP as source of free radicals, has been previously reported in the literature [84–86].

3.3.4 Microbeads functionalization and protein conjugation

Since PolyAcrylamide chains are nonfouling, an additional step is required to functionalized the gels in order to make them able to bind proteins, hence making the gels recognizable for cell adhesion. Two main strategies have been described in the literature as separate ways to conjugate or covalently bond the acrylamide chains with extracellular matrix (ECM) proteins, such as Collagen type I or Fibronectin (FN).

The first strategy is based on the EDC/NHS chemistry [94, 95], where carboxyl groups embedded in the PAAm gel (typically from acrylic acid in the pre-gel solution) are converted into NHS ester groups that will react with primary amines (from proteins or peptides of interest) to form stable (covalent) amides. This reaction is a multistep process in which EDC (1-ethyl-3-(-3-dimethylaminopropyl) carbodiimide hydrochloride), first activates carboxyl groups forming an amine reactive O-acylisourea intermediate. This intermediate is quite unstable in aqueous solutions and requires the addition of NHS (N-hydroxysuccinimide) to form a NHS ester, that is considerably more stable than the intermediate acylisourea and allows for efficient conjugation to primary amines at physiologic pH [96].

The second strategy consists of the covalent bonding of sulfonate-coated polyacrylamide gels with primary amines via sulfosuccinimidyl 6-(4'-azido-2'-nitrophenylamino) hexanoate, more commonly known as Sulfo-SANPAH. Basically, this compound contains a nitrophenylazide group that covalently binds PAAm when exposed to UV light (320-365nm). The N-hydroxysuccinimide ester in sulfo-SANPAH can then react with primary amines to permit binding of ECM proteins to the surface of the gel, hence generating a biocompatible elastic substrate [30]. Brief schematics of both coupling reactions can be seen on Figure 3.5.

To functionalize the microbeads produced with our flow focusing device, we decided to use the second strategy (see 3.2.2), despite the fact that it has been argued that using a

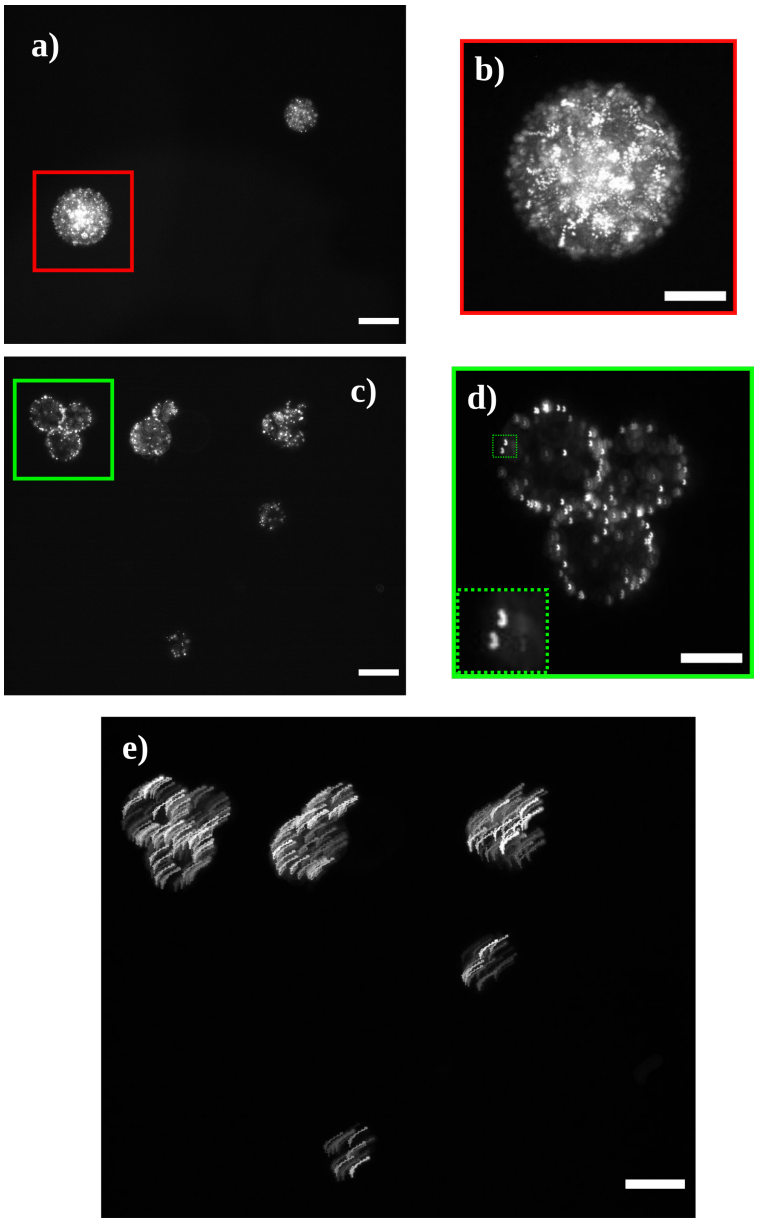

Figure 3.4: Photopolymerization of pre-gel solution microdroplets after exposure of 15 min UV light (302nm). a) Fluorescent image of pre-gel microdroplets prior to polymerization showing the embedded nanobeads in solution. b) Maximum intensity projection image of 20 snapshots taken every 10 seconds of the insert marked in a). Brownian trajectories of fluorescent nanobeads are indicative of no polymerization. c) Fluorescent image of PAAm microbeads after polymerization showing the embedded nanobeads in solution. d) Maximum intensity projection image of 20 snapshots taken every 10 seconds of the insert marked in c). Coherent translations of the fluorescent nanobeads are observed inside the microbeads. e) Maximum intensity projection image of 600 snapshots taken every 10 seconds of the field of view presented in c). This image shows very clear solid body movements of the fluorescent nanobeads embedded in the solution which points to a high degree of polymerization. Scale bars of images is 300 μm. Scale bars of inserts b) and d) is 150 μm

UV-dependent activation mechanism may result in non homogeneous protein coatings while also being a slower and more involved strategy [44]. However, our results show a rather homogeneous protein coating and cell attachment in the microbeads, while being a quite simple and fast (two steps and only 1 extra reagent involved) protocol, in our opinion.

The first four insets of Figure 3.6 show the Airy scan images of a fixed culture containing a sample of one of our microbeads batches of flexible PAAm microbeads functionalized with 50 μg/mL of Fibronectin and co-cultured with vascular endothelial cells. We imaged the sample in 4 fluorescent channels. FITC (495-519 nm) showing the conjugated FITC-FN complex, TRITC (547-572 nm), showing the distribution of internal fluorescent nanobeads, Cy5 (650-670 nm), showing the the cytoplasmic content of the vascular cells monolayer around the microbead and finally DAPI (358/461 nm), to show the spatial localization of the cell nuclei around the sphere. All 4 channels show a homogeneous distribution of protein coating and excellent cell attachment which proves the efficacy of our protein conjugation protocol. Insets f) and g) of Figure 3.6 show an isosurface reconstruction of the FITC-FN coating around the microsphere for the three dimensional volume showing as well a homogeneous protein coating along the entire sphere.

3.3.5 Mechanical characterization of microbeads

To characterize the mechanical properties of the produced microbeads in our flow focusing microfluidic device, we conducted a series of experiments using atomic force microscopy (AFM) to quantify the stiffness of the polymerized gels. We used flat gels as proxy for our microbeads since our Acrylamide polymerization reaction relies on a photoinitiator with increased water solubility that guarantees a more homogeneous polymerization reaction and hence, mechanical properties.

Atomic Force Microscopy (AFM) was used to characterize the mechanical properties of flat gels with different ratios of Acrylamide and Bis-Acrylamide and LAP. AFM uses nanoindentations to determine the hardness of a local region in the gel. Samples are positioned on top of a piezo-driven stage that moves them upwards towards a cantilever with a tip of selected geometry. Once the sample enters in contact with the tip, the cantilever

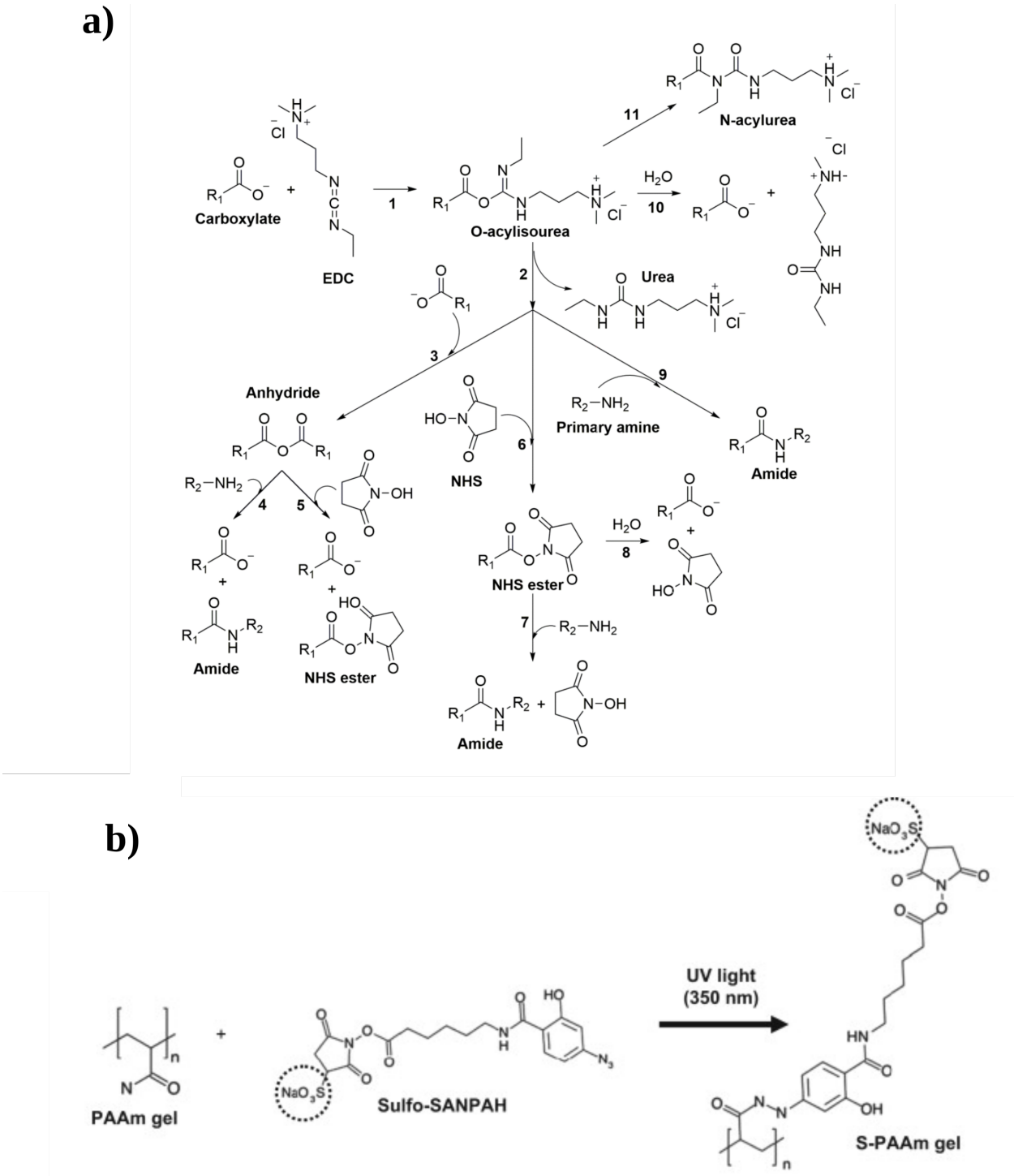

Figure 3.5: Schematic diagrams of the coupling reactions between PolyAcrylamide (PAAm) gels and ECM proteins. a) Schematic diagram of the coupling reaction between carboxylates and primary amines via EDC/NHS chemistry (Adapted from [96]). b) Scheme for reaction of sulfosuccinimidyl 6((4-azido-2-nitrophenyl)amino) hexanoate (Sulfo-SANPAH) with polyacrylamide (PAAm). Adapted from [97].

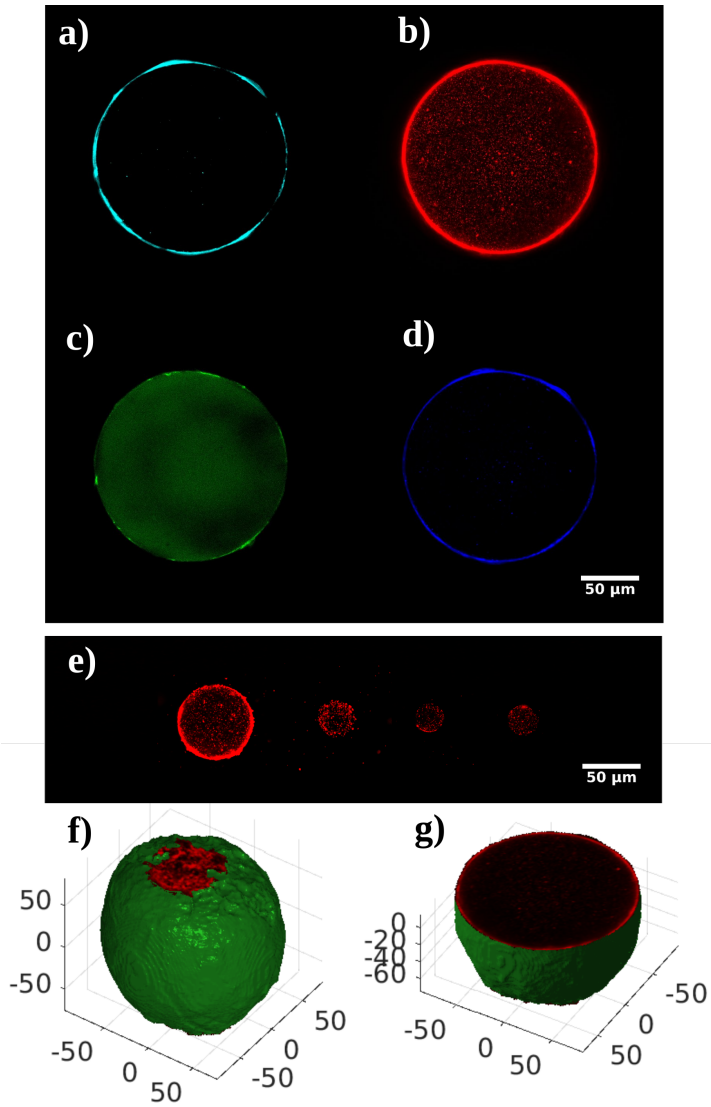

Figure 3.6: Polymerized PAAm microbeads can be functionalized with ECM proteins and become a 3D-biocompatible substrate for cells and tissues. The first inset of the figures shows Airy scan confocal images of a PAAm bead functionalized with FITC-FN and surrounded by a layer of adhered vascular endothelial cells (HuVec). a) Cy5 channel shows cytoplasmic CellTracker fluorescent dye b) TRITC channel shows the fluorescent nanobeads. c) FITC channels shows the fluorescent FITC-FN coating. d) DAPI channels shows the nuclei of the endothelial cells surronding the microbead. e) Different sizes of polymerized microparticles generated with our flow-focusing microfluidic device. f) Three dimensional reconstruction of the Airy scan confocal images of a microbead coated with FITC-FN. g) Equatorial cut of the microsphere shows uniform distribution of fluorescent nanobeads inside the PAAm microbead.

deflects and its motion is captured by the reflection of a laser beam in a photo-detector (Fig). In hard samples the deflection of the cantilever and the distance traveled by the stage are the same, however, for soft samples such as hydrogels, the cantilever also captures the indentation of the tip into the sample. Deflection-indentation curves can be easily converted to force-indentation by using the characteristic spring value of the cantilever. These curves were fitted with the Sneddon model and its correction for pyramidal tips, to extract the sample Young's modulus.

We first compared the effects of LAP and APS over gels with different ratios of Acrylamide to Bis-Acrylamide. The results shown in Fig clearly demonstrate that for gels with a low stiffness the effects of APS are not significant when compared to polymerizing with 2mM LAP (3.1767 $\pm$ 0.1853 kPa vs 3.395$\pm$0.7004 kPa and 8.7011$\pm$0.6643 kPa vs 8.7765$\pm$0.9588 kPa). However, for stiffer gels, there is a significant difference when comparing polymerization with APS and 2mM of LAP (38.3090$\pm$4.8310 kPa and 53.4103$\pm$7.8274 kPa).

Additionally, we compared the effect of LAP concentration on gels with same ratio of Acrylamide to Bis-Acrylamide (Fig). Results show that for concentration of 0.2mM and 2 mM of LAP there are no significant differences in between them (8.7091$\pm$0.2423 kPa and 8.7765$\pm$0.9588 kPa) and with gels polymerized with APS (8.7011$\pm$0.6643 kPa). Nonetheless, for a concentration of 10mM LAP the Young's modulus increases (10.2423$\pm$0.764 kPa).

The results shown in Figure 3.7 clearly indicate that the use of LAP as photoinitiator does not significantly affect the stiffness values previously reported for mixtures of Acrylamide/Bisacrylamide [30]. Previous studies have reported heterogeneities on the mechanical properties and structure of polymerized microbeads when the initiator is introduced in the oil phase of the emulsion [71, 98]. This strategy relies on a polymerization reaction that initiates from the outer part of the sphere and progresses inwards to the center of the sphere. While some other studies argue that no significant differences in the structure of the polymer was observed [17] following this approach, we believe that introducing the initiator inside the microbeads pre-gel solution from the beginning guarantees higher homogeneity in the polymerization reaction, hence giving our photoinitiated approach advantages over other methodologies.

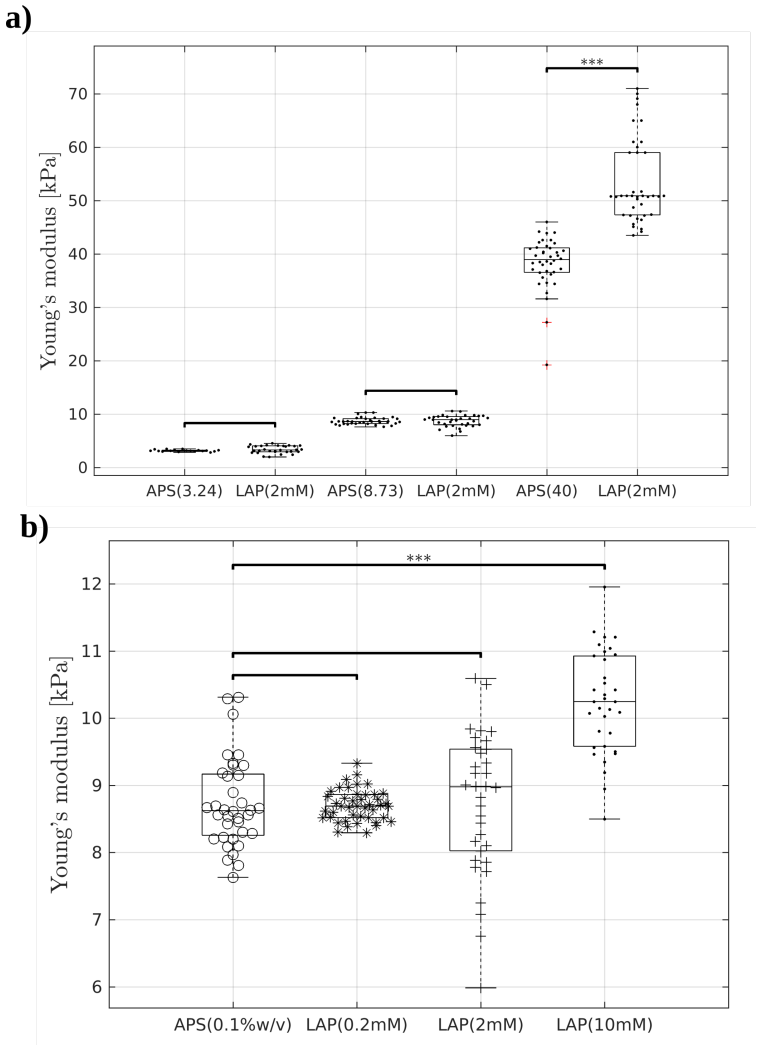

Figure 3.7: PolyAcrylamide gels elasticity analysis by AFM indentation. a) Comparison of LAP photoinitiator with a chosen concentration of 2mM with traditional APS 0.1% (w/v) formulation for three different stiffness values. Only for gel stiffness values as high as 40kPa significant differences were observed between the use of APS and LAP. b) Effect of increased concentrations of photoinitiator in the pre-gel solution. Only significant differences were observed when concentration values were increased up to 10 mM.

3.3.6 Spatial distribution of fluorescent nanobeads inside PAAm Hydrogels

Homogeneity in the spatial distribution of fluorescent nanobeads inside PolyAcrylamide gels is crucial in order to quantify cell-induced deformations via image correlation in three dimensional assays [60, 61]. Fluorescent carboxylated nanobeads of ∼200 nm in diameter were embedded inside our PAAm microbeads to serve as fiduciary markers for deformations inside the gel. Carboxylate-modified nanobeads are typically manufactured by grafting polymers containing carboxylic acid groups to sulfate microspheres. As a result of this grafting process, the beads end up with a highly charged, relatively hydrophilic and porous surface layer. However, the particles are polystyrene-based and hence they always retain some hydrophobic characteristics. Anionic microspheres are typically very sensitive even to rather small concentrations of multivalent ions, and for this reason, calcium and magnesium salts are usually avoided in buffers in order to avoid particle clustering [99]. For chemical stability reasons (prevent charge neutralization of nanobeads surface groups that would lead to particle clustering), carboxylated nanobeads are also recommended to be used with buffers that guarantee a pH level greater than 5.0.

For planar PAAm hydrogels, a higher density of fluorescent nanobeads close to the surface is usually desired, while keeping a relatively smaller density in planes below the surface so that they don't bleach into the surface plane. The reason for this is that Traction Force Microscopy (TFM) measurements are typically done acquiring a z-stack (see Figure 3.8.a) of images in the fluorescent channel associated with the nanobeads and centered at the surface of the gel with some planes above and below it to optimize accuracy of the image cross-correlation method [100]. This can be easily achieved by using PBS as the main buffer when preparing the pre-gel solution. PBS has typically a pH of 7.4 but also adds some charge concentration to the solution in the form of salt ions that neutralizes some charges on the surface of the nanobeads, thus increasing their hydrophobicity and somehow pushing them out of solution, typically to the free surfaces, the bottom coverslip and the top surface of the gel. This creates a rather mild surfactant effect that optimizes the three

dimensional nanobead density inside planar gels for 3DTFM applications, as shown in Figure 3.8.d. We imaged planar PAAm gels using confocal microscopy (Airy scan) and generated z-stacks of fluorescent images of the beads distribution for each plane, separated 0.5 μm in the z direction. We can clearly see a rather homogeneous nanobead spatial density of $\sim$0.3 beads/μm^2, with a rather apparent leap in density as we approach the bottom coverslip ($\rho \sim 0.4$ beads/μm^2), and especially near the top surface of the gel, where the nanobeads density dramatically jumps almost by ten fold ($\rho \sim 3$ beads/μm^2). Nanobeads spatial density distributions were computed using an in-house developed code that finds local maxima in the fluorescent images (Fig. 3.8.b), corresponding with individual beads positions as described in 4.2.

For spherical PAAm microbeads intended to function as force probes in three dimensional settings, it is quite important to achieve a homogeneous three-dimensional spatial distribution of fluorescent nanobeads inside the spheres and avoid localized regions of increased concentration of fiduciary markers that could saturate mask the correlation between stressed and relaxed states. For this reason, in our pre-gel solution we used deionized water as the main buffer to minimize the presence of ions in solution beyond our fluorescent nanobeads. Of particular concern was the pressence of the photoinitiator LAP in solution (a lithium salt). However, after computing the histograms of the spatial density of beads (beads/μm^2) on every z-plane of the z-stack (Figure 3.9.d), we saw a rather constant value of $\sim$0.3 beads/μm^2 for every plane throughout the volume of the sphere, without any significant jumps. A 2-D probability density function for the spatial density of nanobeads encountered along all z-planes is plotted on Figure 3.9.e.

Finally, a comparison between both planar and microspheres is plotted on Figure 3.10, proving the suitability of our fabricated PAAm microbeads as homogeneous three dimensional force sensors.

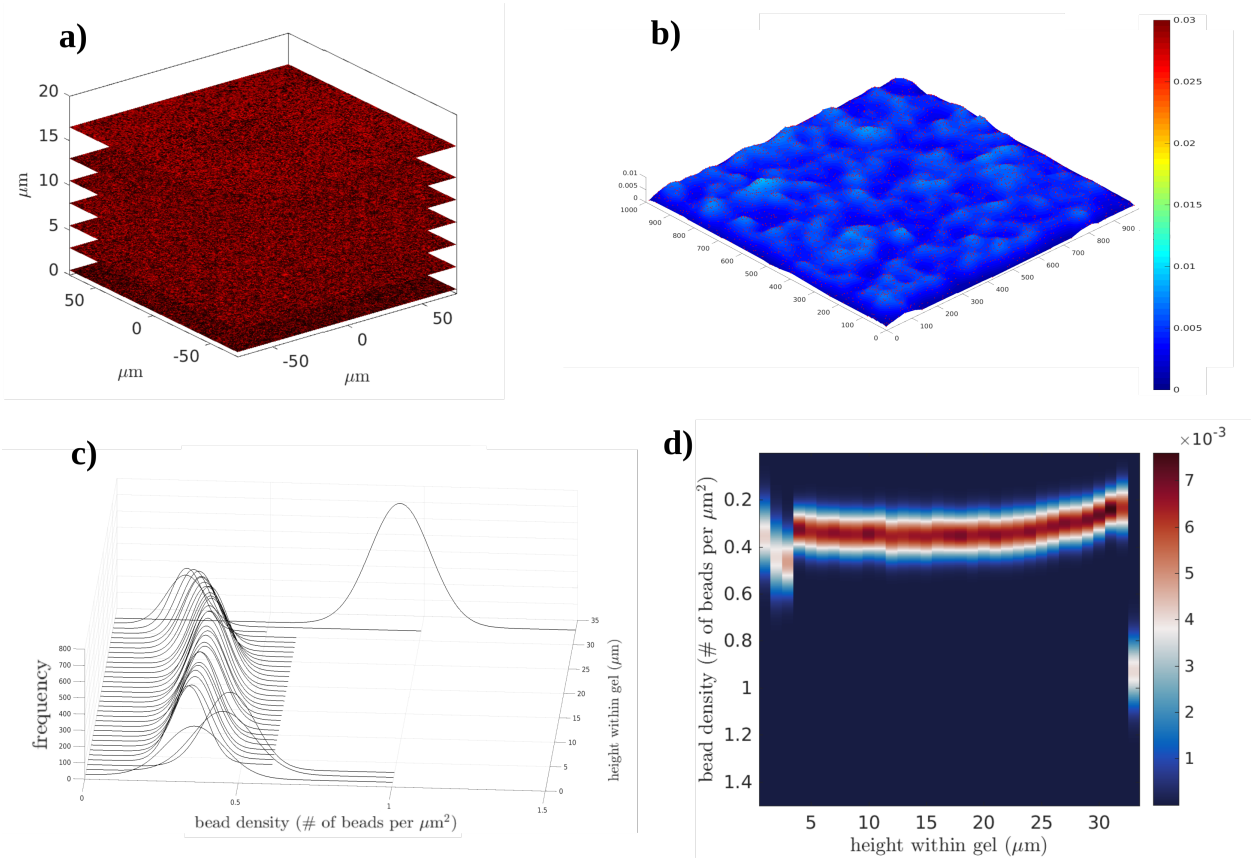

Figure 3.8: A z-stack of fluorescent images was taken (Δz=0.5 μm) of a planar PAAm gel generated as described in [28, 101]. The use of PBS as main solvent for the pre-gel solution combined with having two preferred surfaces (bottom silanized coverslip and top free surface), generates a biased bead distribution of nanobeads inside the gel. a) Z-stack images were taken every 0.5 μm in the z direction. b) Three dimensional surface plot of the nanobead density for a certain plane in z. c) Three dimensional histogram of nanobeads density for the entire PAAm gel. d) 2D probability density map of the nanobeads density for each z plane imaged within the planar PAAm gel.

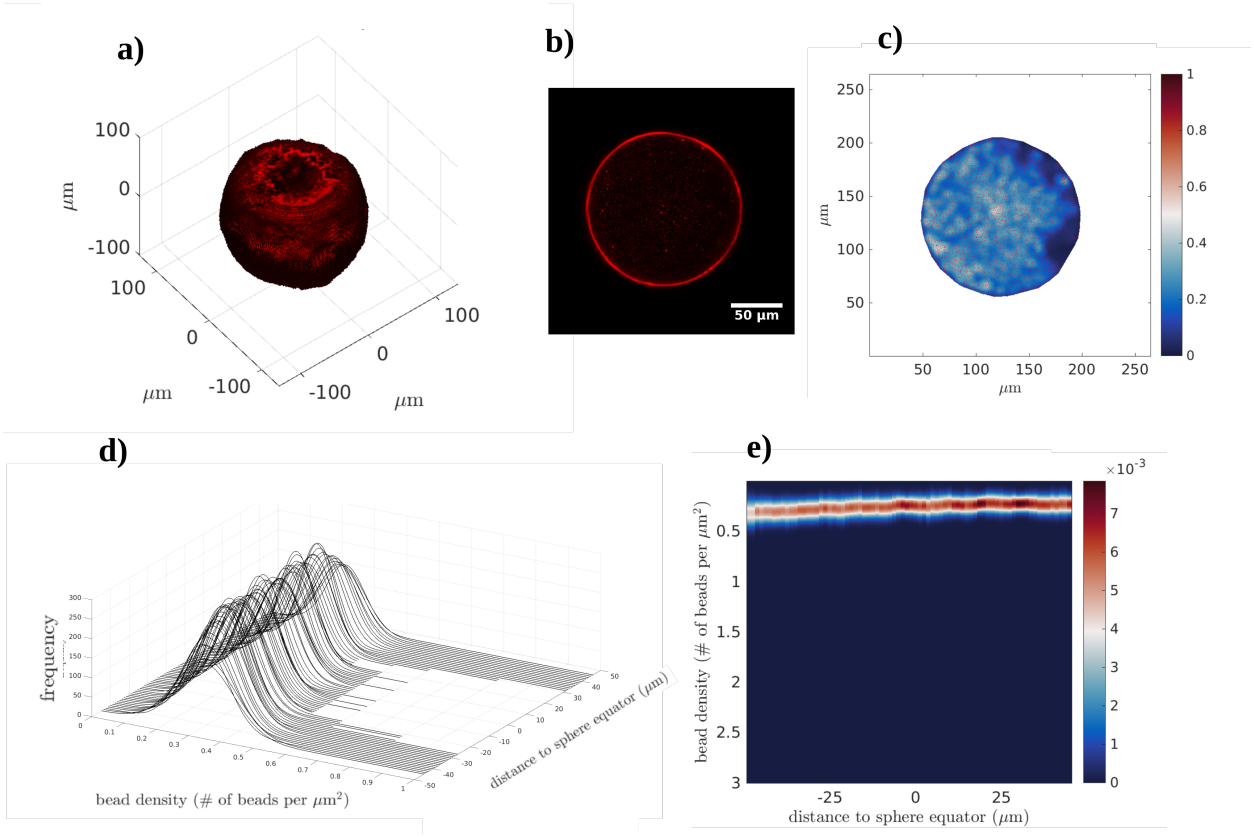

Figure 3.9: A z-stack of fluorescent images was taken of a spherical photoinitiated polymerized PAAm microbead generated with our flow focusing device. For spherical gels, a homogeneous nanobeads density distribution is preferred to avoid loss of resolution at the surface of the microbead. Deionized water was used as main solvent of our pre-gel solution to prevent a preferential localization of nanobeads at the surface of the gel. a) 3D reconstruction of Z-stack images taken every 1.21 μm in the z direction. b) Airy scan image reconstruction of equatorial plane of the microsphere showing fluorescent nanobeads. c) Spatial density distribution of nanobeads (beads/μm^2) for equatorial plane of the microsphere. d) Three dimensional histogram of nanobeads density for the planes imaged in the microsphere. e) 2D probability density map of the nanobeads density for each z plane imaged within the photopolymerized PAAm microsphere.

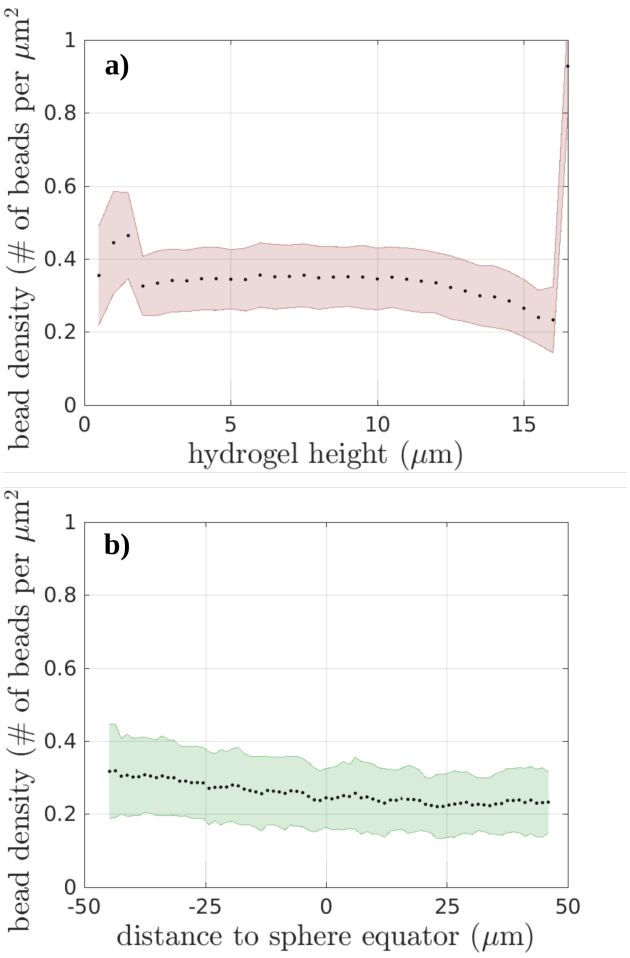

Figure 3.10: Comparison between nanobeads density distribution for each z plane for planar PAAm gels VS photoinitiated polymerized PAAm microspheres. a) fluorescent nanobeads spatial density inside planar PAAm hydrogels plotted against hydrogel height. Shaded region represents standard deviation. b) fluorescent nanobeads spatial density inside photoactivated polymerized PAAm spherical hydrogels plotted against distance to the equator of the sphere. Shaded region represents standard deviation.

3.3.7 Quantification of encapsulation mechanical forces exerted by vascular endothelial cells on schistosoma mansoni egss of varying stiffness

One of the myriad of potential applications of our newly developed three-dimensional microbeads force quantification platform is the quantification of mechanical forces exerted by vascular endothelial cells when they are trying to engulf schistosoma mansoni eggs [102].

Schistosomiasis is a chronic and morbid disease of affecting approximately 200 million

people worldwide. Mature schistosoma flatworms wander in the host's hepatic portal and mesenteric venous system where they encounter a range of blood flow conditions and geometrical confinement [103]. Once in the venous system, they mate and produce eggs which eventually exit the body via the faeces or urine. Many eggs, however, become trapped in internal tissues and organs through the formation of granulomas, inducing chronic inflammation and fibrosis [74, 104].

The egg excretion process still remains ill-defined to date [105] and very little research has been conducted so far to understand the mechanics of the interaction between schistosoma mansoni eggs and the vascular endothelium when the egss are first internalized into tissues from the blood stream and also, the interaction between the eggs and the epithelium that precedes the release of eggs into the intestinal lumen to complete the parasite's life cycle. A proper description of the biochemical and mechanical cues of these tow egg-cell monolayer interaction is therefore long due.

In order to investigate this process, we performed 3DTFM experiments of mature, immature and dead eggs on top of HUVEC cells attached to a flexible PAAm substrate seeded with fluorescent nanobeads [28] and computed the intracellular tension inside the endothelial monolayer [100]. From these experiments, we concluded that endothelial cells exert tangential and downward pushing forces on the substrate when encapsulating schistosoma eggs, generating also significant intracellular tensions inside the monolayer [102]. We could not however quantify the actual three dimensional stresses that the eggs experiment and that could trigger the mechanically-induced secretion of cytokines from inside the egg.

In order to investigate the process of vascular internalization of flexible inert particles, we generated flexible PAAm microbeads of similar size of schistosoma mansoni eggs coated with 50 μg/mL of fibronectin and co-cultured them with vascular endothelial cells overnight. After $\sim$12 h, it was evident that the vascular cells completely embedded the microbeads (Fig. 3.11.a-d). Further SEM imaging of the sample (Figures 3.11 and 3.12) revealed actin-rich filaments (Figures 3.11.e and 3.11.f) coming radially from the endothelial substrate and towards the center of the microsphere that were compatible with downward mechanical pushing forces, as previously reported for mature, immature and dead schistosoma mansoni

eggs being engulfed by endothelial monolayers [102].

This results show that vascular endothelial cells are able to engulf big flexible spherical particles (r$\sim$100 μm) through the exertion of three dimensional traction forces with a preferentially downward pushing component. The results shown in Figure 3.11 also open the door to investigating the effect on the vascular endothelial layer of mechanically-induced secretion of chemokines from the flexible particles that could have a dramatic effect in the immune response and initial granuloma formation [105].

3.4 Discussion

Quantifying compressive stresses in living tissues has proven itself a rather hard task so far [109]. Up to this date, very few methods have achieved somehow reliable ways to quantify cell-generated mechanical forces in three dimensional assay [15–17, 44, 58, 60, 110, 111]. Despite the wide range of existing techniques to explore cellular and tissue mechanics in vitro and in vivo, particular scenarios such as embryo development, xenograft tumor models or the recently blooming field of organoid culture and development from induced pluripotent stem cells (hiPSC), remain elusive to direct in vivo quantitative mechanical measurements of tissue mechanics, in part due to the complexity of such specimens (multiple time and length scales), but also due to the fact that minimal perturbations are typically required to keep enough physiologically relevance during the mechanical measurements [112].

Some methods have used functionalized oil droplets capable of quantifying anisotropic normal stresses caused by the surrounding tissue [15]. However, they are mostly based in incompressible fluids and hence incapable of quantifying compressible forces or shear, due to the liquid nature of the force probe.

Some other approaches have been more focused on the use of hydrogels to develop three dimensional elastic probes capable of quantifying anisotropic and isotropic compressive (or tensile) forces as well as shear stresses. Biocompatible alginate-based hydrogels have been proposed as linearly elastic force probes to be used for compressive stress quantification [60]. However, the process of fabricating and functionalizing the alginate beads is

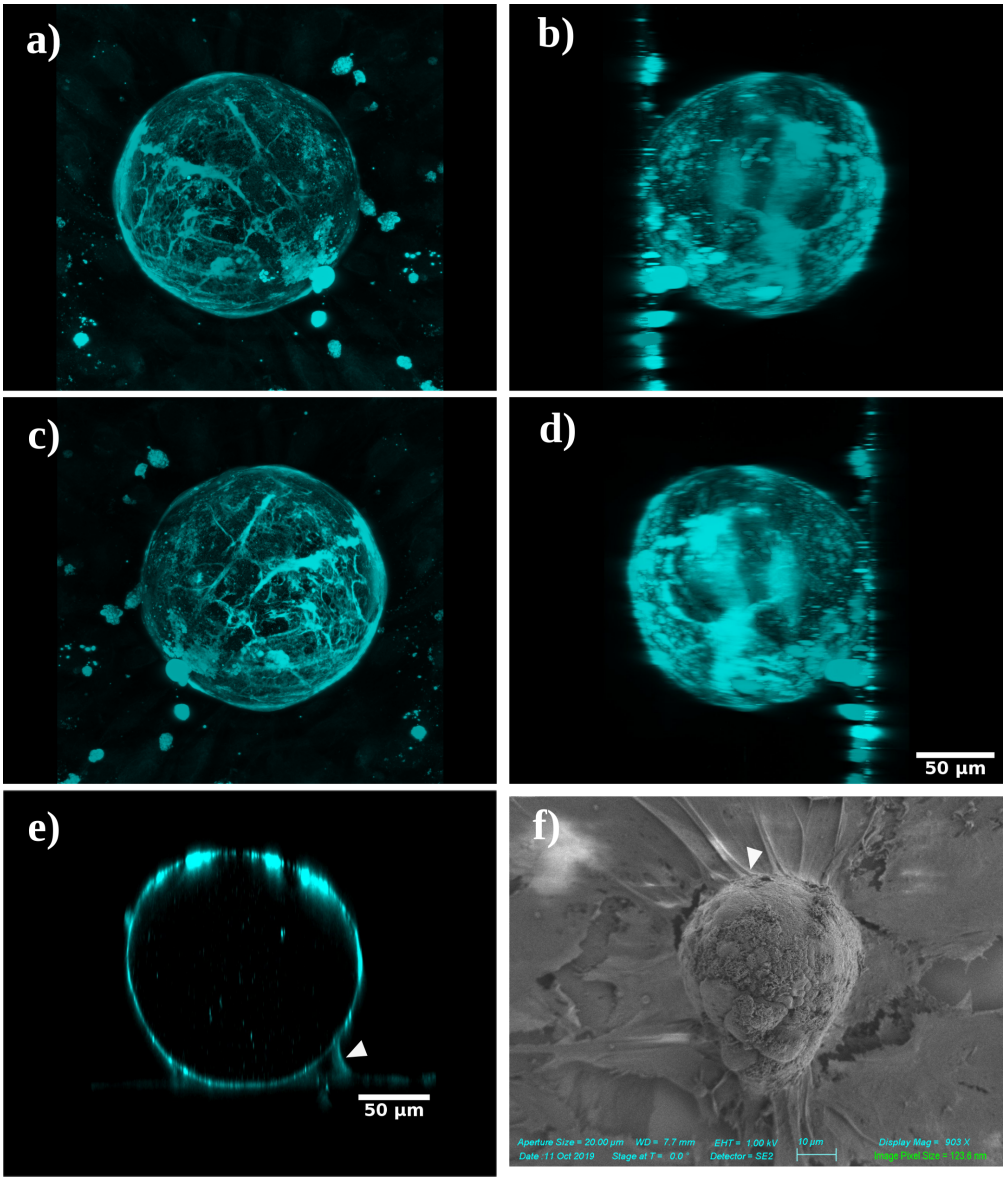

Figure 3.11: Three-dimensional view of a photoactivated polymerized PAAm microsphere functionalized with FN and completely engulfed by vascular endothelial cells (HUVEC). Several angular points of view are shown in the composition. a) Vertical/cenital point of view. b) View rotated 90° (sagittal view). c) View rotated 180°. d) View rotated 270°. e) Sagittal equatorial section of the sphere showing a detail of the actin-rich filopodia-like structures that help HUVECs to encapsulate and engulf the functionalized bead. f) SEM image of the completely engulfed PAAm bead showing a perspective of the HUVEC's filopodia-like structures engulfing the bead, mechanically compatible with a vertical downwards pushing traction force distribution.

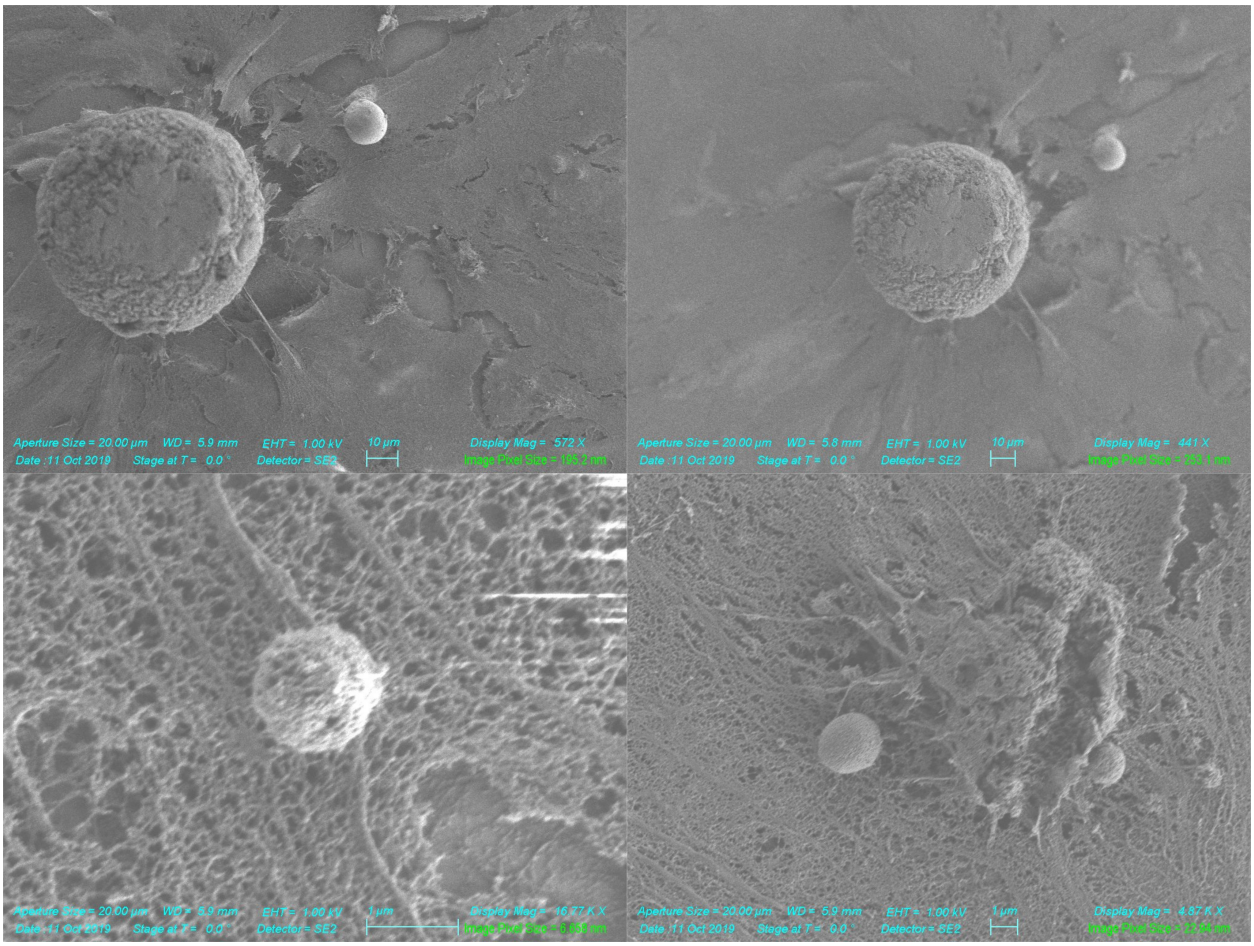

Figure 3.12: SEM captures of different size PAAm microbeads interacting with vascular endothelial cells.

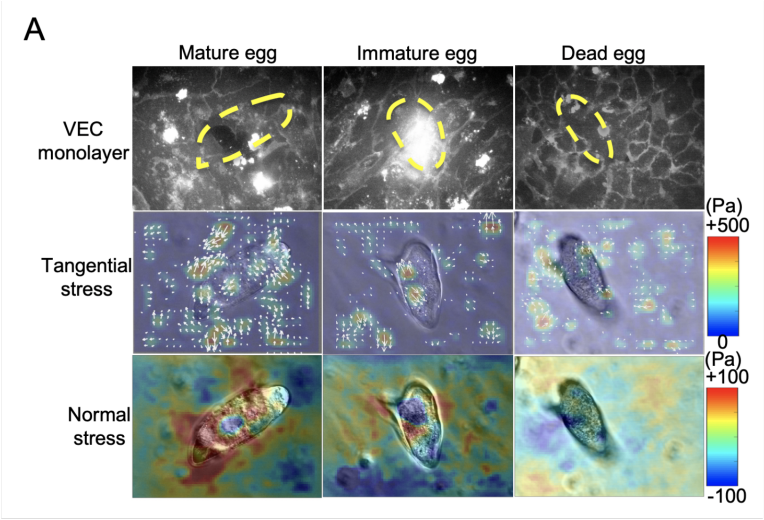

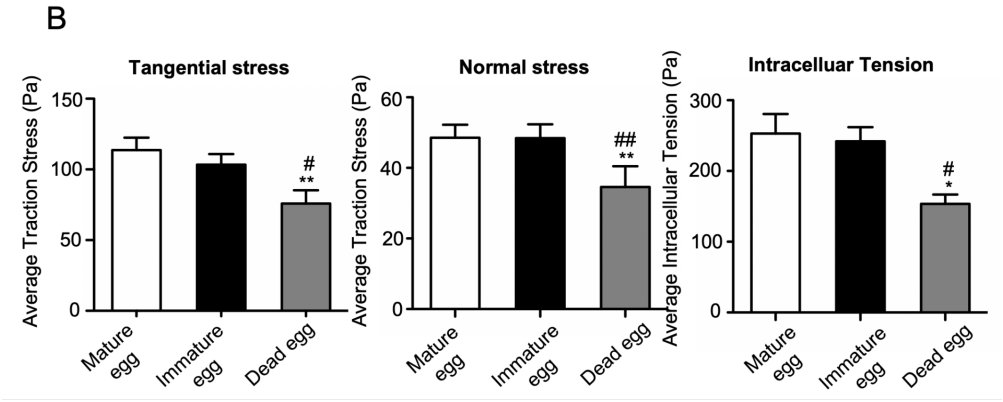

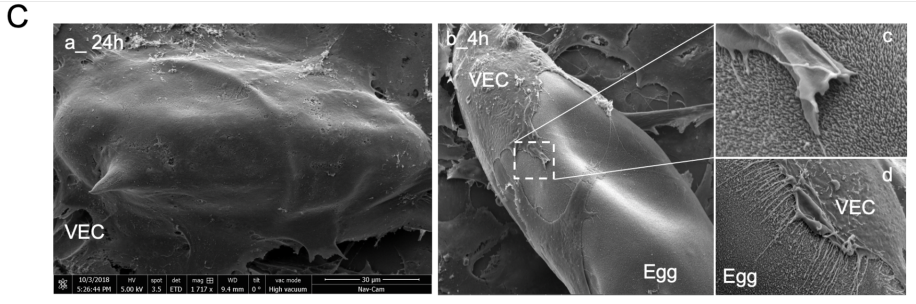

Figure 3.13: A - Vascular endothelial cells exert three dimensional traction forces in order to encapsulate the Schistosoma mansoni egg. The magnitude of these forces depend on the viability of the eggs and particularly drop for dead eggs. B - Tangential and normal traction forces are statistically significantly smaller when the schistosoma mansoni egg is no longer viable. In addition, the intracellular tension [100] experienced by VECs is smaller when the egg is not alive. C - VECs form actin-rich filopodia-like structures that physically connect and encapsulate Schistosoma mansoni eggs [106–108]. Adapted from [102]

tedious and involves several reagents, purification steps and a careful pH control to ensure gel homogeneity and the presence of enough integrin-binding for cell adhesion available in the microbeads. Alginate-based biomaterials have traditionally been used in wound healing, drug delivery, and tissue engineering applications mostly due to their strong biocompatibility (non-degradable in mammals when covalently crosslinked) and ease of gelation [113], but their limited range of linearity constitutes a major drawback in order to become a standard in three dimensional force quantification. Another issue with this method arises from the fact that alginate was ionically cross-linked by calcium, making the microbeads vulnerable to degradation in environments with rapidly changing ionic concentrations, and hereby, cell type dependent.

Apart from alginate, other types of hydrogels have been proposed recently. Particularly, Polyethyleneglycol (PEG)-based microbeads have been conjugated with Förster resonance energy transfer (FRET) fluorophore pairs, showing a fluorescence shift upon global or local tissue deformations [114]. Needless to say, FRET pairs conjugated to elastic substrates require of extensive calibration efforts [115] that invalidates their candidacy as potential three dimensional force probe standards.

As a natural evolution from the successful investigations of cell mechanics on top of flexible PolyAcrylamide (PAAm) substrates (typically two dimensional), some other authors have developed PolyAcrylamide-based droplets of micrometric dimensions typically generated from emulsifications of a water-oil mixture and have then typically used them to quantify three dimensional isotropic and anisotropic compressive forces [16, 17, 44, 71, 110, 111].

A recent study [17] has developed highly uniform, deformable and tunable hydrogel particles based on Acrylamide-BisAcrylamide solutions emulsified through the SPG emulsification technique [116]. The method, specifically designed for studying ligand-dependent cellular interactions constitutes a very elegant approach to reference-free three-dimensional force quantification and living tissues and is successfully applied to phagocytic engulfment of elastic microparticles by macrophages. However, the need for specialized and expensive equipment to produce the microspheres (a microporous glass membrane), and the dependence on superresolution imaging techniques to reconstruct the three dimensional shape of

the spheres (required for force quantification), makes this method not available to laboratories without specialized resources.

An easier but quite effective approach has also been recently introduced as a way to produce polyacrylamide microbeads by inverse emulsification of pre-gel solutions inmmersed in oil reservoirs [71, 110, 111], however, the introduction of high levels of mechanical energy during emulsification results in a widely disperse distribution of microbeads sizes that is not easily controllable. In addition to this, the quantification of compressive stress levels, based on the measured deformation of the microparticle, is in need of some assumptions (uniform tensile and compressive loads along the microparticle axial and radial directions), and prone to errors.

One last representative technology that has been recently introduced is based on the fabrication of PAAm microbeads using a flow focusing microfludic device that generates an emulsion of pre-gel solution beads mixed with oil [44]. Following this approach the authors are able to produce monodisperse beads at rates as high as 20-60 kHz. In order to polymerize the pre-gel solution, they used free-radical crosslinking copolymerization of acrylamide (AAm) and N,N'-methylenebisacrylamide (BIS) initiated by ammonium persulphate (APS). However standardized this approach is for two-dimensional substrates (typically several orders of magnitude bigger in size than the micrometric beads), the authors reported substantial dispersion of bead elasticity and structural parameters, most likely due to the fact that they introduce the initiator in conjuction with the mixture of acrylamide monomer and crosslinker. This is probably the cause of co-monomers (in the presence of the initiator since the very beginning) starting to interact in the pre-gel volume prior to droplet formation at the flow-focusing device. It has been previously reported that pH and total monomer concentration will have strong impact on the reactivity ratios [117], and it seems clear that both monomer and crosslinker concentration will not be constant in time with this strategy, hence causing a time-dependant dispersion in elasticity in the beads produced in the flow focusing device.

To produce our elastic microbeads we opted for Polyacrylamide (PAAm)-based spherical hydrogels produced in an in-house developed flow focusing microfluidic device as a way

to produce monodisperse force probes that can be easily functionalized with ECM proteins and introduced into developing three-dimensional tissues. PAAm hydrogels were selected for their biocompatibility, non-degradability in culture conditions, compressibility and ease of surface functionalization, but most importantly, due to the fact that PAAm stiffness can be tuned over a large range by adjusting monomer and crosslinker concentrations [30]. Once the master of the microfluidic device, containing multiple designs per silicon wafer, has been optimized and fabricated, a vast amount of PDMS devices can be casted on the same wafer, which boosts the yield of different devices and experiments that can be produced with one single silicon wafer. We believe that our microfluidic platform (Fig 3.1) and protocol is simple enough while having powerful capabilities to produce monodisperse elastic hydrogel beads in a high throughput manner.

Control of microbeads size and homogeneity

Control of droplet size and frequency inside a flow focusing microfluidic device is a complex fluid dynamics problem that has received quite a bit of attention in the past decades due to the increasing interest in generating monodisperse emulsions in industrial applications [66, 118–123].

The dynamics of breakup in a flow-focusing device cannot be completely explained by a competition between the shear stress and interfacial tension [124]. However, scaling laws have been described [125, 126] for the different regimes typically enconuntered (squeezing, dripping and jetting) and flow-focusing devices are capable of producing controllable emulsions with a polydispersity index well below 1% [64].

With our in-house developed flow focusing device, we were able to produce droplets of sizes ranging from 20 to 100 μm (Figs. 3.3 and 3.6.e) and with a polidispersity index of $\sim 6\%$. Our device is a successful combination of the flow-focusing strategy to generate the initial droplets and several downstream passive-breakup T junctions that further reduce the size of the liquid droplets initially generated in the device [67].

We were able to succesfully generate homogeneous cell-size beads that can serve as elastic force probes for embryogenesis or organoid development applications [16, 110], as well

as one order of magnitude bigger microbeads intented to serve as a proxy for schistosoma mansoni eggs, to investigate the role of the egg mechanical properties and cytokyne release activity during encapsulation by vascular endothelial cells [102].

Photopolymerization of hydrogel microbeads

Photopolymerized hydrogels [127] are recently being thoroughly investigated for a number of tissue engineering applications mostly because of the ability to polymerize in situ in a minimally invasive manner such as by injection of the liquid pre-gel solution at the site of injury and posterior polymerization via typically a UV source. [128–131].

While polymerization of monomers using visible or UV light sources work well for many applications [132], they generally are not widely used in tissue engineering applications because most conventional monomers can be cytotoxic. Consequently, photopolymerizable hydrogels for tissue engineering applications have generally been formed from macromolecular hydrogel precursors (PEG acrylate derivatives, PEG methacrylate derivatives and modified polysaccharides such as hyaluronic acid derivatives).

In order to produce homogeneously polymerized monodisperse hydrogel microbeads to be used as force probes in three dimensional environments, it seemed natural to choose hydrogel photopolymerization as a way to ensure structural homogeneity inside droplets of micrometric size. Several studies have already reported an important level of dispersity in mechanical properties within the same batch of beads [44, 71], when using the typical initiators commonly employed to polymerize PolyAcrylamide gels, Ammonium persulfate (APS), Azobisisobutyronitrile (AIBN) and the accelerator Tetramethylethylenediamine or TEMED, which we hypothesize could be due, in part, to inhomogeneous polymerization at the micrometric scale [98].

Among the commercially available photoinitiators, 1-[4-(2-hydroxyethoxy)-phenyl]-2-hydroxy-2-methyl-1-propanone, also known as Irgacure 2959, has been commonly used for gel encapsulation and other photopolymerization reactions involving the fabrication of radial-gradient matrix polyacrylamide substrates of varying stiffness [30, 133] or the fabrication of high-throughput phenotypical screening assays for force and stifness quantification of

cardiomyocytes [134], despite exhibiting significant limitations.

Irgacure is a type I photoinitiator and, despite being one of the most available water soluble compounds, the reported water solubility for this photoinitiator is less than 2 wt% [85]. While this factor was overcome for planar PAAm gel applications [134], where fast polymerization was achieved when the pre-gel solution was exposed to UV light (365nm wavelength) in gels of ∼12 mm in diameter and ∼40 μm in height, it becomes of particular concern when trying to polymerize micrometric sized water-based microdroplets using a fluorinated oil as the continuous phase in the emulsion.

When trying to photopolymerize emulsified water-based microdroplets, water solubility and particularly, the partition coefficient [135] of the photoinitiator chosen for the pre-gel solution becomes of significant importance. The partition coefficient, defined as the ratio of the concentrations of a solute between the two solvents (a biphase of liquid phases), specifically for unionized solutes (Eq. 3.1).

$$logP_{oct/wat} = log\left(\frac{[solute]^{unionized}_{octanol}}{[solute]^{unionized}_{water}}\right) \tag{3.1}$$

The partition coefficient is hence a measure of the hydrophilic or hydrophobic properties of a chemical substance. Consequently, this coefficient is a measure of differential solubility of the compound between the two solvents. For our microdroplet generation application, $logP$ then became particularly relevant, since we were concerned about the poor solubility exhibited by Irgacure 2959 when we first tried to use it as our photoiniator. We hypothesized then that, even though Irgacure 2959 was initially being dissolved in our pre-gel solution, its rather high $logP$, may be causing migration of the solute into the fluorinated oil phase, reducing drastically the effective solute concentration insode our droplets that resulted in pratically impossible polymerization via UV initiation.

Even though the reported value of $logP$ in the literature for Irgacure 2959 (0.74, [136]) has been substantially improved since its predecesors I-184, I-651 and I-907 (2.34, 4.75 and 3.00 respectively, [137]), and is quite smaller than those of other commonly used photoinitiators such as benzophenone (3.21, [136]), our attempts to use this photoinitiator

to polymerize droplets of micrometric sizes were not successful using concentrations as high as 100mM of I2959.

For this reason, we decided to investigate the possibility of using photoinitiators with increased water solubility and more benevolent partition coefficient, as a way to increase the efficient solute concentration of initiator inside our droplets. We decided to try monoacylphosphineoxide salts, in particular Li-TPO (oxide form), also known as Lithium phenyl-2,4,6-trimethylbenzoylphosphinate or LAP 3.14, a water soluble, cytocompatible, type I photoinitiator for use in the polymerization of hydrogels or other polymeric materials. This photoinitator seemed to be a better option than Irgacure 2959 for biological applications due to its increased water solubility, increased polymerization rates with 365 nm light, and absorbance at 400 nm allowing for polymerization with visible light. It also has improved polymerization kinetics when compared to I2959 which is very promising and opens the door to its use at reduced initiator concentration and longer wavelength light that could potentially permit its polymerization in in vivo applications [84–86, 138].

As reported in [86], LAP has a much better water solubility (47g/L vs 5g/L for I2959), three times less toxicity than I2959 (3.1 LC_50 VS 9.0 for I2959), and also an increased rate of polymerization (670 mmol/L/s for LAP vs 540 mmol/L/s for I2959). As we can see in Fig. 3.14 from [85], LAP shows a decent level of molar extinction coefficient at wavelengths within the visible spectrum ($\sim$ 380 nm), which makes it a potential candidate as a photoinitiator for in vivo applications. Still, photopolymerization at typical UV wavelengths ($\sim$ 300nm) show a similar exponential behavior as I2959 (Fig. 3.14).

Since LAP has a significantly high water solubility, even though we could not find reported values for its partition coefficient in the literature, we were able to efficiently polymerize polyacrylamide base microdroplets with concentrations of LAP as low as 2mM, and report a homogenous distribution of fluorescent nanoparticles inside the beads, that constitutes strong evidence of a homogeneous polymer network 3.9. In addition to this, we would expect a far more homogeneous polymerization reaction in our assay (where the initiator is dissolved inside the droplets prior to polymerization initiation via UV light) than in the assay reported in [44, 71], where the initiator is included in the bulk pre-gel solution and

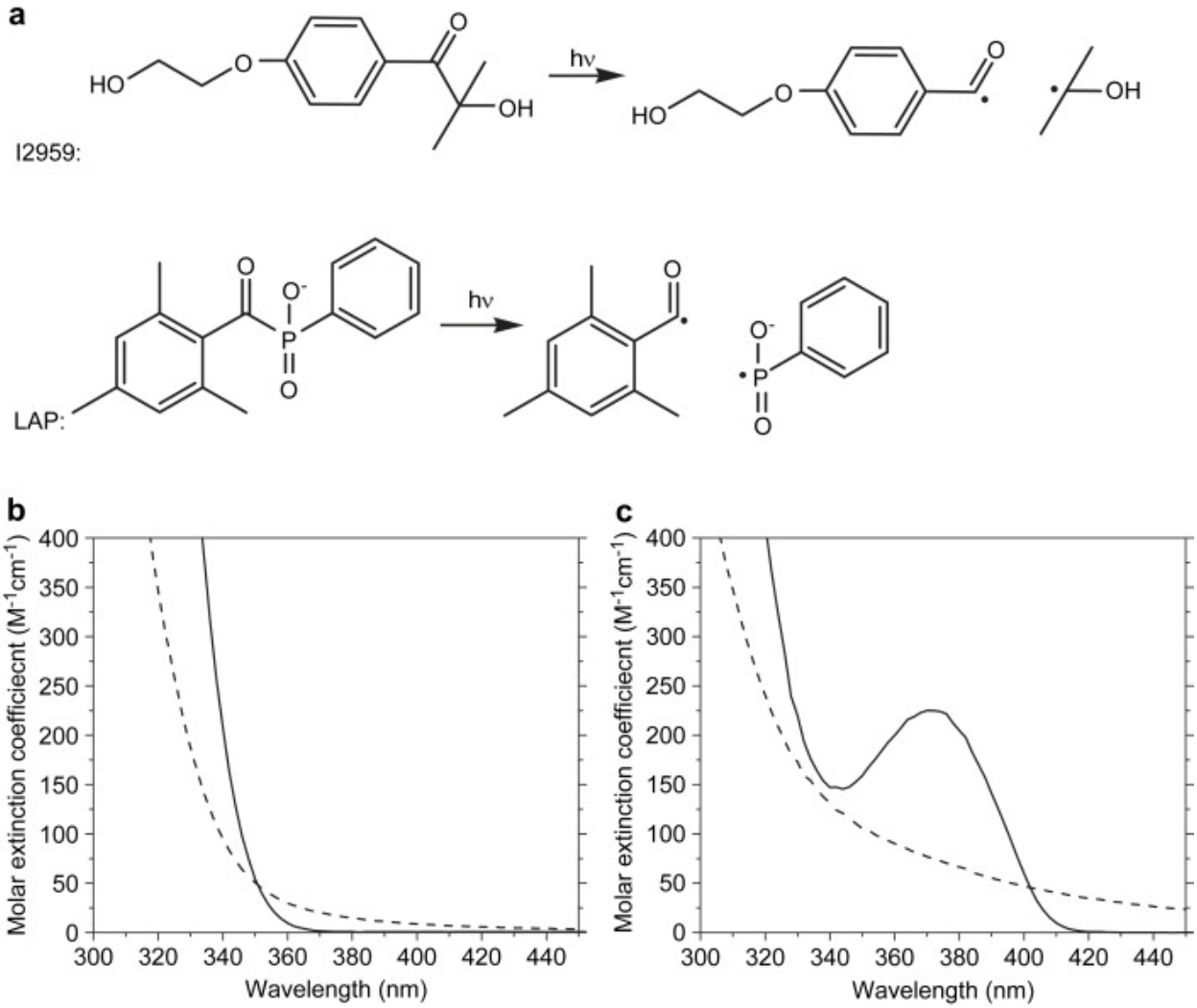

Figure 3.14: (a) Cleavage of I2959 and LAP into substituent radicals following photon absorption. (b) Molar absorptivities of the I2959 (solid line) and cleavage products (dashed line). (c) Molar absorptivities of LAP (solid line) and cleavage products (dashed line). Adapted from [85]

reacting even before the liquid droplets are formed and hence causing a time-dependent polymerization kinetics that would result in structural heterogeneity within the batch and possibly inside the droplet, or even through SPG droplet extrusion [17], where the polymerization of acrylamide droplets is induced from the outside-in of the droplet, by addition of $\sim$ 1.5mg/mL of Azobisisobutyronitrile (AIBN) after completing the extrusion phase. Previous studies reported surface layers of the microbeads peeling off suggesting differences in the polymer composition between the surface layer and the core of the beads [98].

Mechanical characterization of hydrogel microbeads

In the past five years there has been an increased number of publications focused on the production of polymerized hydrogel microbeads [17, 44, 60, 71, 96, 110, 111]. However, only a few studies have reported mechanical properties of polymerized polyacrylamide microbeads to serve as force probes in three dimensional settings [17, 44, 71].

Atomic Fore Microscopy is typically the standard to assess mechanical properties in hydrogels [30]. However, some other methodologies such as Real-Time Deformability Cytometry (RT-DC) have also been proposed as a way to investigate the poroelastic properties of PAAm [44, 139]. Measurements reported so far using AFM exhibit some discrepancies that have been attributed to surfactant adsorbance at the surface of the beads [71], or even to inhomogeneous polymerization due to the varying composition of pre-gel solution with time [44].

In this study, we present AFM indentation measurements in planar PAAm hydrogels photopolymerized with the recently introduced LAP photoinitiator with different concentrations of the initiator. The results show a smooth linearly elastic behavior of the PAAm for all concentrations tested. As reported previously, viscoelastic dissipation can be neglected for PAAm gels in AFM measurements and poroelastic effects can be neglected as well when using a pyramidal tip [140].

Since our method of polymerization uses a photoactivatable, water-soluble initiator that is already dissolved in the pre-gel solution and initiates the polymerization reaction only when exposed to UV light (hence completely controllable), we expect a small level

of dispersity in mechanical properties in our microbeads as well as agreement with our measurements in planar gels, since our protocol includes thorough washing steps as well as a surfactant cleaning step with 20% v/v 1H,1H,2H,2H-Perfluoro-1-octanol (PFO) in HFE-7500. Nevertheless, further investigation of the mechanical properties of photopolymerized PAAm microbeads with varying sizes and monomer/crosslinker composition ratios is still required.

Hydrogel microbeads surface functionalization and protein conjugation

A number of studies involving protein conjugation to hydrogels have opted for the path of EDC/NHS [94, 95] as a way to efficiently conjugate proteins and achieve higher coupling efficiency and more stable amine-reactive intermediates. While we in no manner disagree with the effiency and robustness of this technique as a way to conjugate ECM proteins to polymerized hydrogels, we argue that using the standard technique to coat ECM proteins on top of planar hydrogels [30], by means of activating a 0.2mg/ml solution of Sulfo SANPAH on top of the gels and then incubatin with ECM proteins, constitutes a fast and efficient way of coating our microbeads that resulted in good fibronectin-FITC conjugation to our spheres (Fig. 3.6) and formidable cell attachement (Fig. 3.12).

Hydrogel microbeads as a force probe standard and extended capabilities

In this study we have demonstrated a robust and efficient manner to produce spherical hydrogels of micrometric size via photopolymerization of pre-gel acrylamide solutions using a water soluble and biocompatible photoinitiator (LAP). While the potential applications to this technology are enormous at this moment and furthermore, increasing as new ideas for convoluted gel geometries arise [141], the potential for biocompatible photoinitiators such as LAP are beyond exciting. As more and more ECM-derived hydrogels and biocompatible monomers (GelMa, MeHa, etc.) are being developed and synthesized [142, 143] the possibility of in-situ polymerization and force quantification in in-vivo scenarios seem to be closer in our scientific horizon.

It is also particularly exciting to consider the possibility of in-situ polymerized hy-

drogels not only as force probes but also as platforms capable of releasing chemicals ad hoc when being squeezed or stiffened in a control manner [142].

3.5 Conclusions

In this chapter we have shown the development of a robust and reliable way of producing photoinitiated polymerized PolyAcrylamide elastic microbeads with tunable mechanical properties that can be very easily functionalized with the extracellular matrix (ECM) protein of interest.

We produced a monodisperse distribution of microdroplets inside an in-house designed and developed flow focusing microfluidic device with a relatively high throughput. As expected, the polidispersity index for our beads is rather small ($\sim$ 6 %) and more than adequate for our application as elastic force probes.

We then collected and polymerized the still liquid pre-gel solution beads by means of the incorporation of a photoinitator in the initial pre-gel solution. The use of the photoinitiator Lithium phenyl-2,4,6-trimethylbenzoylphosphinate (LAP), overcomes all the problems previously encountered with the use of the standard photoinitiator compound for 2D hydrogels, 2-Hydroxy-4'-(2-hydroxyethoxy)-2-methylpropiophenone, also known as Irgacure 2959. The improved water solubility and partition coefficient of LAP permits adequate solution in the water-based pre-gel solution and, more importantly, retention in the dispersed phase (water) during emulsification.

We were also able to efficiently and rapidly functionalized our microbeads with conjugated FITC-FN, that allowed for visualization of the homogenous coating in all spheres as well as permitting cell attachment and complete engulfment of the elastic microbeads by human endothelial cells.

We then characterized the mechanical properties of planar PAAm gels with the same formulation as our microbeads obtaining perfectly linearly elastic behaviors that allowed us to anticipate similar results for our microbeads since our polymerization strategy is the most homogeneous and controlled reported so far.

We were also able to quantify and characterize the spatial distribution of fluorescent nanobeads inside planar and spherical hydrogels. Fluorescent nanobeads are introduced in the pregel solution to serve as fiduciary markers for gel deformation in Traction Force Microscopy (TFM) applications. In planar two dimensional gels, a higher concentration of beads near the surface is typically desired and this is achieved by the use of a saline buffer in the gel solution that induces nanobead migration to the free surfaces. For our microbeads however, a spatially homogeneous distribution of nanobeads was found for all planes close and far from the sphere equator. This constitutes an optimal situation for 3D TFM applications and represents strong evidence of a homogeneous acrylamide polymerization reaction.

We finally presented results of the interaction of our elastic microbeads with Human Umbilical Vein Endothelial Cells (HUVEC). These results clearly showed how the endothelial monolayer was able to recognize, engulf and exert downward pushing traction forces in an attempt to internalize the foreign object. The technology is hence of particular interest for the study of the interaction of vascular endothelial cells with schistosoma mansoni eggs, since we have observed similar behaviors in endothelial cells when trying to encapsulate the eggs. The possibility of modelling this process isolating different parameters such as surface protein expression, stiffness, geometry and even release of cytokines could constitute a major source of information to advance the understanding the life cycle of the parasite causing schistosomiasis, a chronic and morbid disease of poverty affecting approximately 200 million people worldwide.

Overall, our results demonstrate that our photopolymerized hydrogel microbeads are a powerful tool for the cross-comparison of results obtained from different cell mechanical characterization techniques, and for the validation of future novel techniques, such us our novel capillary controlled hydrogel micro-channels. This technology opens new perspectives for the analysis of stresses exerted not only at the cellular scale, but also inside organoids or developing tissues, where the non-perturbing characterization of mechanical stresses is pretty much nonexistent to date.

With the increasingly growing interest in exploring the roles of tissue mechanics in physiology and pathology, significant advances are arising aimed at developing new technolo-

gies that can serve as force probes to quantify 3D tissue mechanical properties. Particular interest is being dedicated to increasing the throughput and accuracy of the 3D mapping of tissue mechanics and to developing new biocompatible materials that can efficiently integrate with the surrounding tissue or even play active roles in tissue repair or engineering. We believe our developed platform along with our previously reported 3D TFM methodologies will constitute an important contribution to the field of three dimensional quantification of tissue mechanics and will contribute to expand the current knowledge of cellular mechanotranduction in physiologically relevant settings.

3.6 Acknowledgements

Chapter 3, in part is currently being prepared for submission for publication of the material. Criado-Hidalgo, Ernesto; Garcia-Herreros, Antoni; Yeh, Yi-Ting; Lasheras Juan C.; del Álamo, Juan C. The dissertation author was the primary investigator and author of this material.

Chapter 3, in part is also currently being prepared for submission for publication of the material. Yeh, Yi-Ting; Skinner, Danielle; Suzuki, Brian; Youjeong, Na; McKerrow, James; Criado-Hidalgo, Ernesto; Zhang, Shun; del Álamo, Juan C.; Caffrey, Connor. The dissertation author was a co-author of this material.

Chapter 4

A capillary controlled hydrogel micro-channel for isotropic compressive stress quantification

4.1 Introduction

As a result of an interrupted blood flow and oxygen supply, tissues inside the human body can be damaged or die. Some physiological functions in vertebrates can temporarily fail without significant impact for the rest of our body, however, blood flow must be maintained continuously to deliver oxygen from the respiratory system to the rest of tissues in the human body in a steady manner [144]. This dramatically important function is realized by red blood cells (RBCs), which enclose oxygen-carrying proteins called hemoglobin. Hemoglobin has a quaternary structure characteristic of many multi-subunit globular proteins that allows it to become saturated with oxygen molecules (oxyhemoglobin). Oxyhemoglobin is formed during physiological respiration when oxygen binds to the heme component of the protein in RBCs. However, RBCs are only capable of carrying a limited concentration of hemoglobin which consequently limits the amount of oxygen that can be transported by each individual cell [145].

Healthy RBCs have remarkable deformability and stability, which enable them to undergo considerable deformation during their flow through capillaries [146]. Of particular

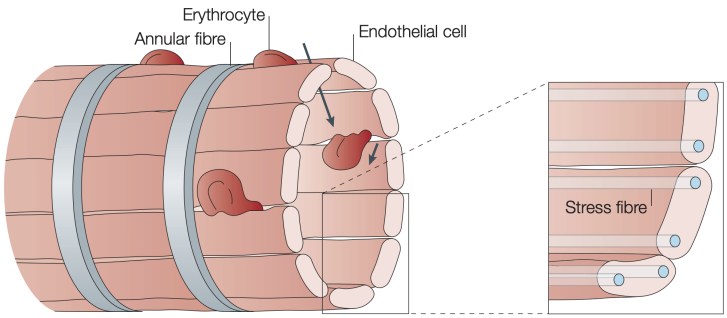

Figure 4.1: Schema of a venous sinus located in the cords of the red pulp. Blood from the cords collects in the sinuses (shown by arrows). The venous sinuses consist of a lining of endothelial cells that are positioned in parallel and connected by stress fibres to annular fibres, which are composed of extracellular-matrix components. The stress fibres run along the long axis of the endothelial cells and are most prominent where the endothelial cells are in contact. Contractility of the stress fibres allows the formation of slits between the endothelial cells, thereby regulating the passage of blood and blood cells from the red-pulp cords into the sinuses and back into the venous system. Because the red-pulp cords contain a large number of macrophages, ageing erythrocytes that are no longer able to pass through the slits are phagocytosed. Adapted from [149]

importance is their travel through microcapillaries, since the microcirculation is responsible for 80 percent of the total pressure drop occurring between the aorta and the vena cava [147], hence exerting significant mechanical loads on RBCs. However, when certain conditions such as iron deficiency anemia, hemolytic disease or even malaria impair the ability of RBCs to deform adequately [148], the transport of oxygen from the lungs to the rest of organs can be compromised, causing a myriad of life threatening symptoms and repercussions.

Diseased RBCs are typically filtered out at the spleen, present in almost all vertebrates through a process modulated by the spleen-specific structure of the interendothelial slit [146, 150]. The structure of the spleen favors the removal of older erythrocytes from the circulation and leads to the efficient purging of bloodborne microorganisms and cellular debris [149]. During their circulation through the spleen, red blood cells (RBCs) are forced to squeeze through gaps between endothelial cells that are ~ 8 times narrower than the typical RBC diameter (Fig. 4.1). The subsequent RBC squeezing motion causes large RBC deformations that remove old and diseased cells from the circulation. Despite the importance of this process, there is limited quantitative data about the deformation and

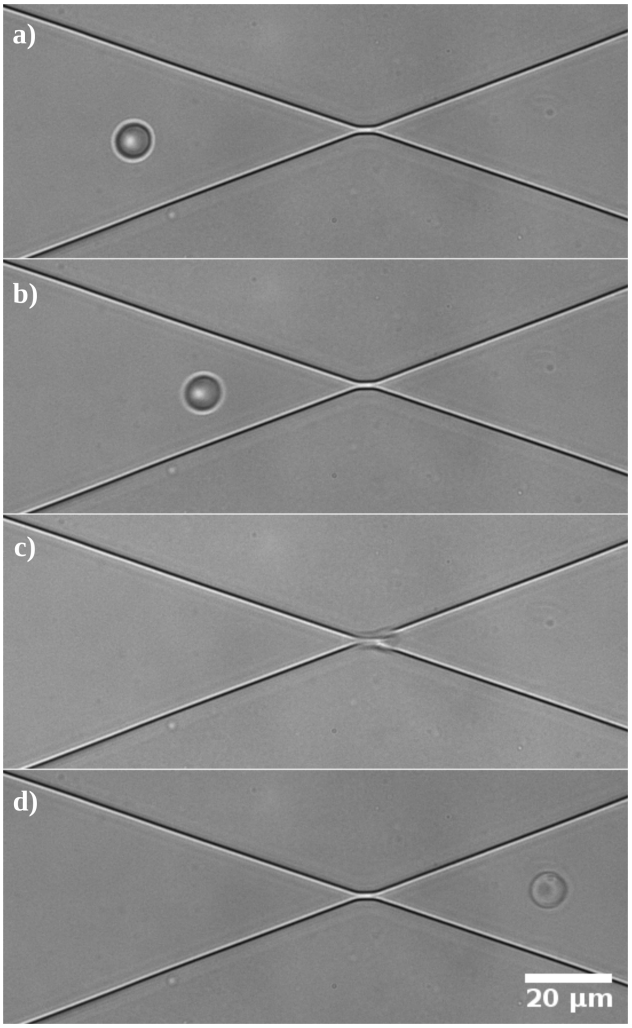

Figure 4.2: Microfluidic device to study the mechanics of RBC inter-endothelial splenic transmigration. a), b) RBC migrating with the flow prior to undergoing spleen flitration-like event. c) RBC going through narrowest section of the constriction. d) RBC after filtration event might exhibit mechanical changes in the cytoskelont-membrane interface. Adapted from [151]

stress experienced by the RBCs. Current state of the art to recreate spleen filtration of RBCs consists typically of microfluidic devices fabricated on PDMS with narrow channels of controlled length, width and height (see Fig. 4.2). The need for new devices and materials that allow to expand our capabilities to reproduce and understand physiologically relevant situations in vitro as well as to be able to quantify and characterize the mechanics of RBC filtration through the spleen is beyond question.

In this chapter we introduce a novel family of PDMS microfluidic devices with $\sim$1 μm

narrow constrictions where we harnessed capillary phenomena to embed photopolymerizable hydrogels of tunable geometry, mechanical properties and surface chemistry that serve as a platform to study in vitro RBC filtration through the spleen in a more physiologically relevant manner than current available technologies. This microchannel can also be seeded with tracer fluorescent particles to allow for stress quantification through traction force microscopy [61].

Our preliminary results show feasibility of the proposed technology and pave the way to a new high-throughput scenario of three dimensional investigation of the mechanics of soft cells traveling through soft constriction or microchannels with tunnable mechanical properties that represent more physiologically relevant landscapes.

4.2 Materials and Methods

4.2.1 Microfluidic devices design and fabrication

A series of in-house designed and manufactured polydimethylsiloxane (PDMS) microfluidic devices were used to produce the hydrogel microchannels [32, 62, 152, 153].

In order to generate photopolymerizable PolyAcrylamide (PAAm) microchannels inside a pre-existing microfluidic device, we designed a new device (Fig. 4.3) in which a high capillary resistance at the entrance generates a big enough pressure drop to facilitate the control of a liquid meniscus inside the channel (at the region of interest) with a high dynamic range. This allows for precise positioning of the meniscus at the region of interest, where the circulating cells will travel through, as well as reasonable control of the curvature of interface once the meniscus reaches the cusps inside the device.

Photolitography

Microfluidic devices were manufactured using soft lithography [32]. The master device for the microchannel microfluidic device was fabricated in a sequential manner initiated by applying a coating of MCC Primer 80/20 (Microchemicals, Westborough, MA) into a 4 inch single side polished silicon wafer (University Wafer, South Boston, MA) for 30 seconds

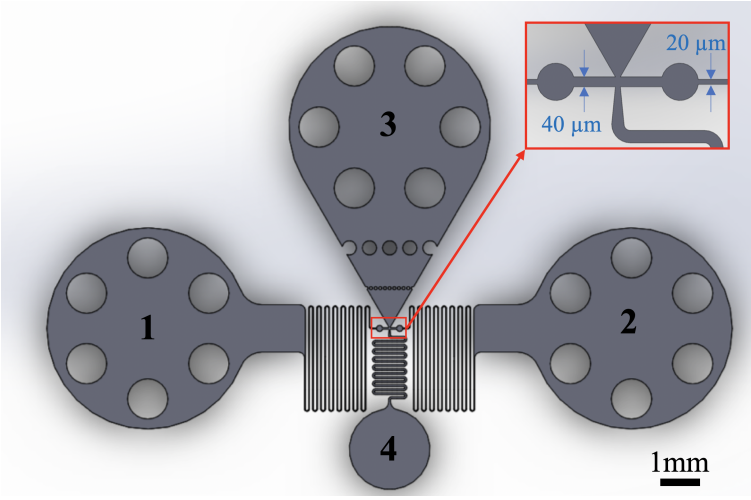

Figure 4.3: Schematic of the microfluidic device used to generate the capillary-controlled PAAm microchannel. [1]: Inlet used to introduce the pregel solution to generate the left side of the microchannel. [2]: Inlet used to introduce the pregel solution to generate the right side of the microchannel. [3]: Inlet used to introduce a fluid phase containing cells/particles to go through the engineered PAAm constriction. [4]: Outlet of the fluid phase of the device for cells/particles collection and downstream assays.

at 3000rpm. Shortly after, a layer of positive photoresist AZ12XT 20PL-05 (Microchemicals, Westborough, MA) was spincoated on top of the primed silicon wafer on a two step process. The first step was done at 500rpm (100rpm/s) and for 10 seconds. The second step was done at 850rpm (300rpm/s) and for 30 seconds. After a short soft bake at 110°C for 2 min, we exposed (250mJ/cm2) the sample under a 375 nm laser using a MLA150 maskless aligner (Heidelberg Instruments Mikrotechnik GmbH, Germany) fed with the drawings of our device designed by SolidWorks (Dassault Systèmes SolidWorks Corporation, Waltham, MA). A post-exposure bake of 1 min at 90°C was performed and the features were obtained by developing the sample for 2 min using AZ-300MIF (Microchemicals, Westborough, MAs). Two 1 min steps of water rinsing were performed to clear the sample from residues. Profilometry measurements using a Dektak 150 surface profiler (Veeco Instruments Inc. Plainview, NY) confirmed the expected thickness of 5μm. Afterwards, the wafer was passivated with tridecafluoro-1,1,2,2-tetra-hydrooctyl-1–1trichlorosilane (Gelest, Morrisville, PA) for 15 min inside a vacuum chamber to prevent PDMS adhesion to the wafer.

PDMS casting and bonding to substrate

PDMS replicas of the device were made by casting a previously degassed for 30 min mixture of the PDMS oligomer and crosslinking agent (Sylgard® 184, Dow Corning Inc. Midland, MI) in a 10:1 (w/w) proportion on the passivated silicon wafer. The sample was then cured at 65°C overnight. The next day the master was peeled off from the wafer, cut into several single devices and the inlet and outlet holes were punched (2.5 mm) with a biopsy puncher (Miltex, Integra Lifesciences, Plainsboro Township, NJ). Finally, we activated the surface of both coverslip (Corning, 24x60 mm and thickness 1.5 mm) and PDMS chip under a UV ozone lamp (Model 30, Jelight Co. Irvine, CA) for 4 min with an oxygen inflow of 0.2 lpm and bonded them together at 65°C for a minimum of 4 hours before they were ready to be used.

4.2.2 PolyAcrylamide microchannel generation

PolyAcrylamide solution and photoinitiator

The pre-gel solution was prepared by mixing 25 μL of 40 % Acrylamide (Millipore-Sigma,Burlington, MA), 30 μL of 2% Bis-Acrylamide (MilliporeSigma,Burlington, MA), 3 μL of 2% 0.2 μm carboxilated FluoSpheres (Invitrogen, Carlsbad, CA), 20 μL of 20mM Lithium phenyl-2,4,6-trimethylbenzoylphosphinate (LAP, Sigma-Aldrich, St. Louis, MO) and 122 μL of deionized water to a total volume of 200 μL that yielded gels of $\sim$ 9kPa. According to the desired hydrogel stiffness the proportion of Acrylamide to Bis-Acrylamide can be re-adjusted [30]. Afterwards, we kept cold ($\sim$ 4°C) and degassed the pre-gel solution for one hour inside a vacuum chamber to prevent gelation inside the syringe while running the experiment.

Capillary control of the interface

Accurate control of the two symmetric hydrogel interfaces at the cusp of the constriction of the microfluidic devices was achieved introducing a long and narrow bifurcation channel located at the entrance in the design of the microfluidic device that generates a large

enough pressure drop to control the movement of the fluid interface at speeds ≤ 1 μm/s with pressure drops $\leq$100 mbar. PTFE tubing with OD = 3/32" and ID = 1/32" were use to connect the 1 ml syringe to the entrance of the microfluidic device. A precision linear stage was used to accurately control the volume drawn from the syringes into the device.

Microchannel polymerization

When the desired geometry of the interface was achieved at the cusp of the constrictions inside the microfluidic device, copolymerization of acrylamide and bisacrylamide (vinyl addition polymerization initiated by a free-radical generating system) was initiated by illuminating the microfluidic device with UV light (302nm) with a benchtop UVP (Analytik Jena US LLC, Upland, CA) transilluminator for 5 minutes triggering the liberation of free radicals by the photoinitiator in the solution. The microfluidic device was immediately carefully washed and hydrated with deionized water to prevent rapidly occurring shrinkage of the gel due to the reduced dimensions.

Microchannel walls functionalization

In order to efficiently functionalize the microchannel with a protein of interest we incorporated Acrylic Acid (AA, Sigma-Aldrich, St. Louis, MO) into the pre-gel mixture to allow covalent coupling of primary amine groups to the polymerized hydrogel via EDC/NHS crosslinking chemistry chemistry [17, 96]. Basically, after hydrogel formation, we flushed activation buffer consisting of a mixture of 100 mM 2-(N-morpholino)ethanesulfonic acid (MES, Sigma-Aldrich, St. Louis, MO), 200 mM NaCl and adjusted to pH 6, through the constriction for 5 minutes. After that, the channel was soaked and incubated for 15 minutes in activation buffer supplemented with 40 mg/mL of 1-ethyl-3-(3- dimethylaminopropyl)carbodiimide, 20 mg/mL N-hydroxysuccinimide (NHS, Sigma-Aldrich, St. Louis, MO) and 0.1% (v/v) Tween 20 (Sigma-Aldrich, St. Louis, MO).

4.2.3 Cell Culture

Red Blood cells isolation from blood and preservation

Human blood from healthy donors was obtained in Heparin treated BD Vacutainer tubes (Becton, Dickinson and Company, Franklin Lakes, NJ) at the San Diego Blood Bank. Upon arrival to the lab red blood cells (RBC) were isolated using a density gradient technique [154, 155]. First, a 15ml centrifuge tube (Falcon tube, Thermo Fisher Scientific, Waltham, MA) was filled with 3 ml of Histopaque 1119 (Sigma-Aldrich, St. Louis, MO). After that, a layer of 3ml of Histopaque 1077 (Sigma-Aldrich, St. Louis, MO) was added on top and then 6 ml of whole blood were carefully added to prevent any mixture of the three layers. Next, the tube was centrifuged for 30min at 700x g at room temperature. Once the centrifugation was done, the top layers containing plasma, mononuclear cells and granulocytes were discarded and the tube was filled with 10ml of PBS (Dulbecco's Phosphate Buffered Saline, Sigma-Aldrich, St. Louis, MO) and RBC were resuspended. The tube was centrifuged again for 10 minutes at 200x g and the supernatant cells were removed, this step was repeated twice to discard platelets and damaged RBCs. Finally, RBCs were resuspended in AS-32 media (dextrose, sodium chloride, adenine, citric acid, sodium citrate and sodium phosphate were all bought from FisherScientific) in a 5% Hematocrit concentration and stored at 4°C until used. All the experiments were conducted within the week of RBC isolation.

4.2.4 Microscopy and Imaging

Phase contrast microscopy

A Leica DMI 6000B inverted phase contrast microscope (Leica Camera, Wetzlar, Germany) controlled by a dedicated workstation running the open source μ-Manager software (Vale lab, UCSF) was used for image acquisition. The microscope was equiped with a Zyla 3-Tap Enclosed C-mount 16 bit camera (Andor Technology, Belfast, UK) and a Mercury Short-Arc Discharge Lamp with Reflector with emission filters to generate excitation light in the usual DAPI, FITC, TRITC, and CY5 wavelengths. All experiments were performed at 37°C inside a temperature and CO2 controlled enclosure. Images were acquired using the

40x (air objective) and 63x (oil) lenses. For the images of Red Blood Cells going through constrictions, a frame rate as high as 100 fps was used for enough time resolution of shape changes in the RBCs.

4.2.5 Image Processing

Image processing was performed using Fiji and ImageJ [39] as well as in-house developed Matlab scripts. Initially images were imported to the workstation through Fiji's Bioformat plug-in, converted into separate 8-bit tiff images and stored back as individual tiff images for each channel. These separate files were then imported into Matlab for further processing. Images were normalized, cleaned up applying median and gaussian filters and contrast was equalized when needed through Contrast Limited Adaptive Histogram Equalization (CLAHE), for visualization purposes only [40].

4.3 Results

This section presents some preliminary results that illustrate the potential of the microfluidic platforms developed in this study. We fabricated a set of PDMS microfluidic devices with embedded channels where we introduced a pre-gel solution consisting of acrylamide monomers, a crosslinker and a photoinitiator. Here we demonstrate that it is possible to polymerize the solution in situ, at the cusps inside the microfluidic device, generating a two symmetric flexible interface that result in a narrow channel with customizable mechanical properties and surface chemistry.

We used conventional phase contrast microscopy to monitor the liquid interface as we were assessing the controllability of the capillary interface. Once the geometry of the inerface is fixed via control of upstream pressure, we photopolymerized the solution generating two symmetric hydrogels at the cusps of the device and were able to functionalize the resulting hydrogels with the protein of interest via EDC/NHS chemistry.

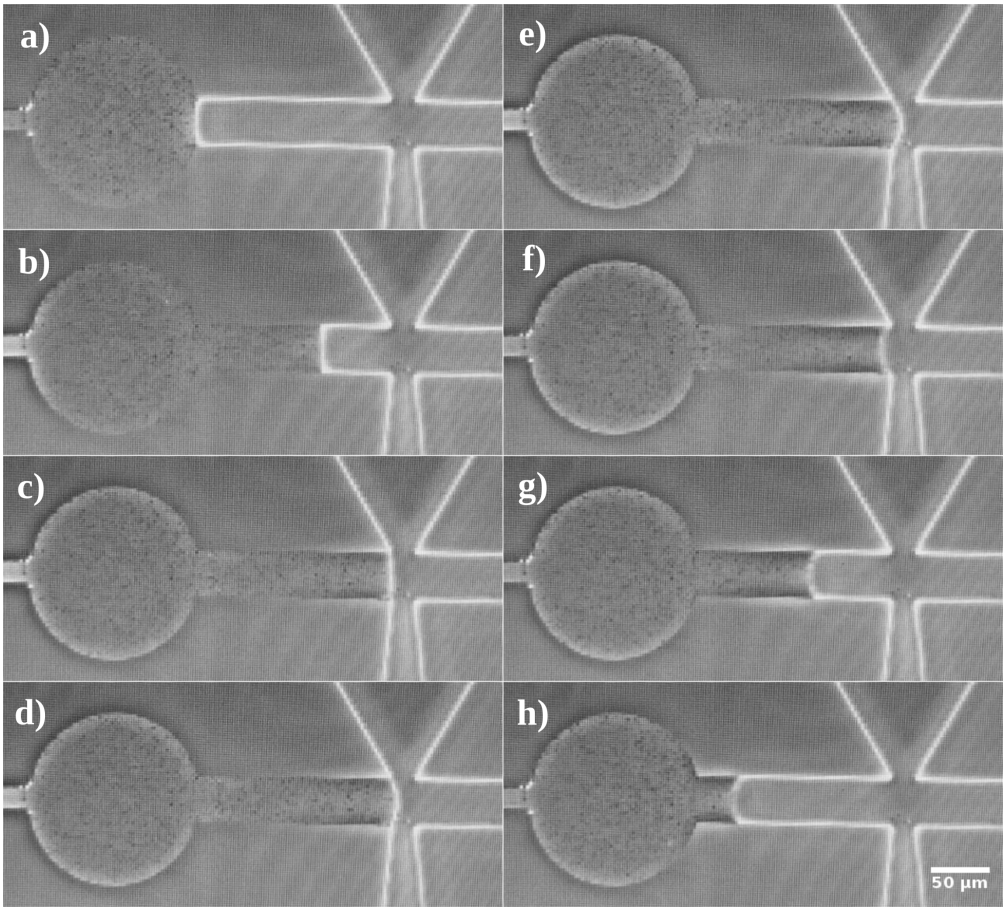

Figure 4.4: Timelapse representation of the microfluidic channel operation and interface controllability. a-e) inserts show the filling process and formation of the anchored capillary-controlled interface at the cusps of the device. f-h) inserts show retraction of the interface via suction from the upstream syringe pump.

4.3.1 Controlling the position of the pre-gel liquid interface

In order to asses the controllability and dynamic range of our microfluidic device (Fig. 4.3), we introduced the pre-gel solution and slowly pumped the solution until we carefully were able to form the capillary interface at the cusp of the device, being this clearly controllable with small steps in pressure of the order of *sim* 1-5 mbar. Once the stability and robustness of the liquid interface were positively evaluated, we proceeded to withdraw the pre-gel solution, resulting in an equally smooth and controllable phase Figure 4.4 shows a timelapse of images of the process followed.

4.3.2 Local curvature distribution and mean curvature radius of the pre-gel liquid interface

With the graphical data obtained we were able to automatically track the position and geometry of the liquid-air interface inside the device using in-house developed Matlab codes taking advantage of the image processing and the computer vision toolbox (in particular the motion-based object tracking module) and analyze the local curvature for all 8 snapshots shown in Fig. 4.4. The results are shown in Figure 4.5.

Snapshots a) to c) in Figure 4.5 show the initial pumping phase inside the microfluidic device, where the capillary stresses are not so notorius and an almost flat interface is possible with a slow pumping speed. The hydrophobic character of PDMS also contributes to an almost flat interface, where the contact angle is $\sim$ 90 degrees (liquid is mostly non-wetting [59]). Once the liquid reaches the free edge of the cusp inside the microfluidic device, an increase of curvature is observed due to the increase in pressure in the quasi-static loading regime, according to the Young-Laplace equation. Insets d) and e) on Figure 4.5 reflect this behavior.

During the rapid retraction phase (shown in snapshots f)-h)), dynamical effects can be seen though, reflecting the behavior predicted by the dynamics of the triple line [59], where a decreased contact angle can be seen in this case due to the increase in the capillary number (which scales linearly with the velocity of the fluid).

After examining the distribution of local curvatures at the interfaces, we computed the mean radius of curvature (R_m) for all of them and plotted the results on Figure 4.6. We can clearly see the initial steps of almost flat interfaces, characterized by huge mean radii (again, due to PDMS' hydrophobicity that results in an almost 90 degrees contact angle), and then a sudden drop once the fluid interface approached the edge and capillary forces kicked in to stabilize the surface of the pre-gel solution. We observed radii as small as 35 μm for the most deformed condition and $\sim$ 50 μm for the previous snapshot (d) in Fig. 4.4).

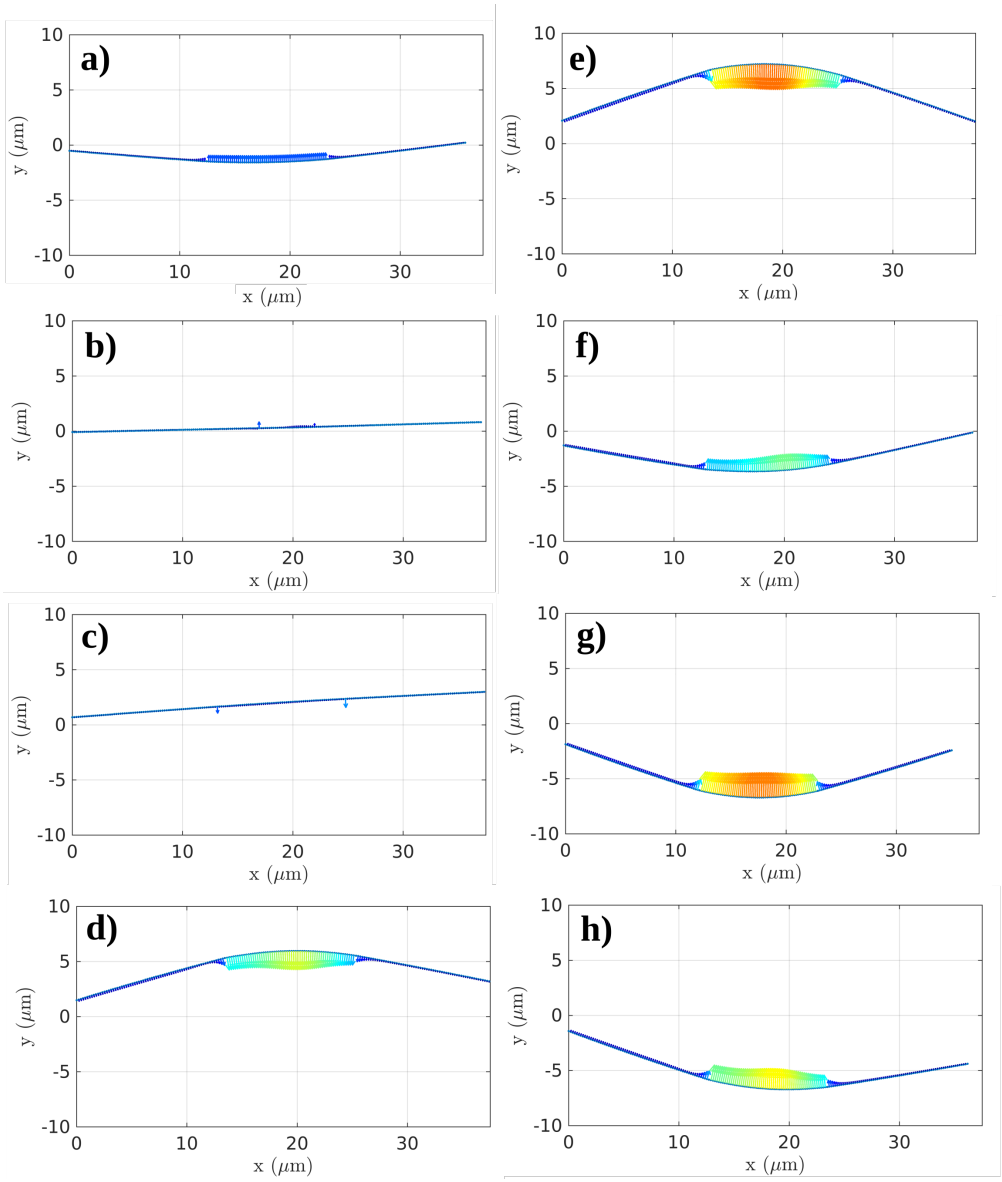

Figure 4.5: Color-coded vectors show local curvature analysis of the free surface of the pre-gel solution inside the microfluidic device. a-e) Filling of the device and anchoring of the interface at the cusp. e) Maximum curvature encountered when the interface is anchored at the cusp of the device. f-h) Emptying the device with negative pressure from upstream syringe pump.

4.3.3 Reconstructed geometries of the nozzle of proposed liquid interfaces

We were also able to reconstruct the proposed geometries of the resulting polymerized nozzle that would arise from the combination of the two symmetric and opposed polymerized

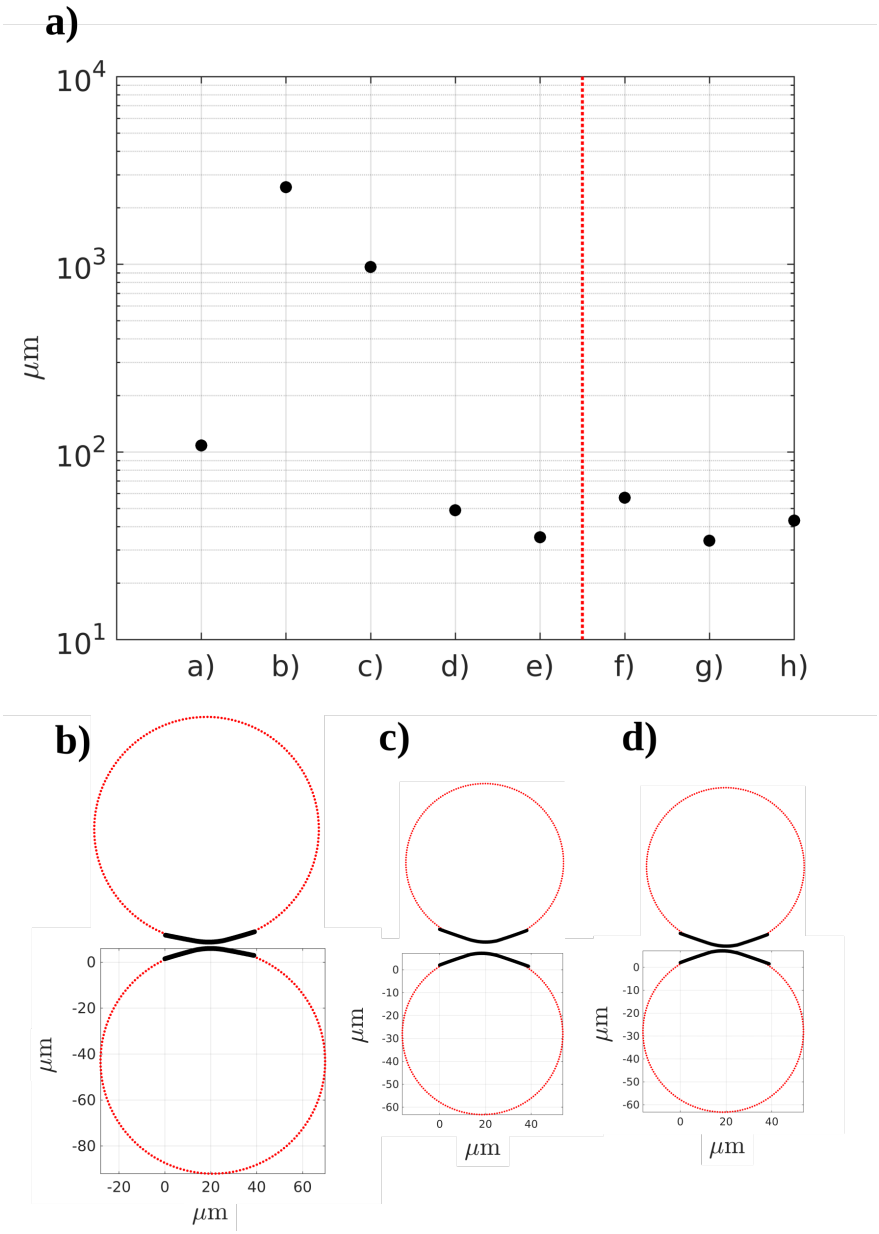

Figure 4.6: Analysis of radius of curvature for the different interfaces inside the microfluidic device. a) Mean radius of curvature for all the liquid interfaces shown in 4.4. Dotted red line represents transition from pumping liquid to withdrawal. b) Graphical representation of resulting nozzle for interface d), where (R_c ~48.9μm) and a width of channel of 5 μm. c) nozzle for interface e), where (R_c ~35.07μm) and a width of channel of 5 μm. d) nozzle for interface e), where (R_c ~35.07μm) and a width of channel of 1 μm.

channels. These two opposed hydrogels are placed closed enough to create the constriction that serves as a mimic for the flexible interspleen slits [149]. We reproduced the geometries for the two cases shown in Figs. 4.4 and 4.5, where the liquid interface is located at the edge

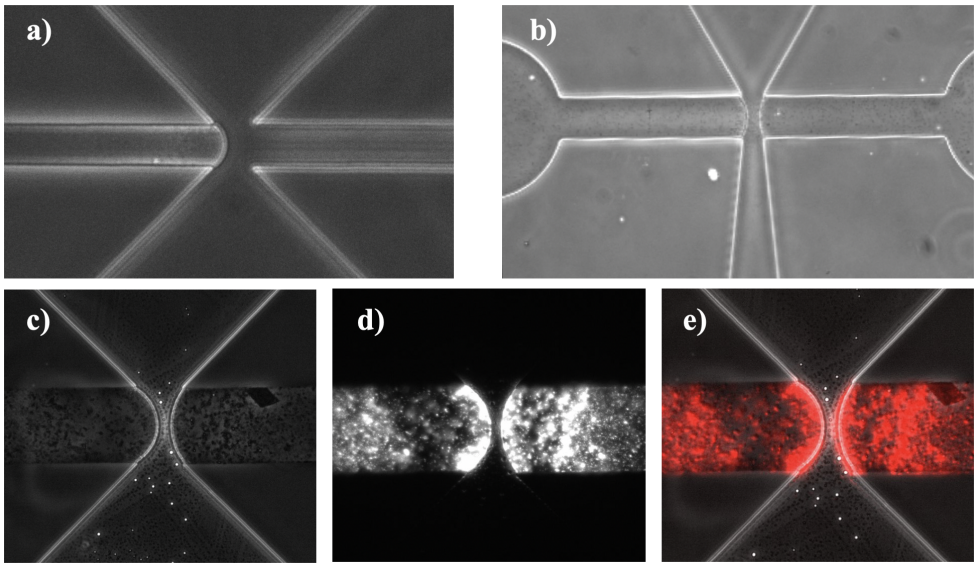

Figure 4.7: Photopolymerized microchannels inside our microfluidic device. Inset a) shows a single channel polymerized. Inset b) shows symmetric and opposed photopolymerized microchannels. Insets c)-e) show an asymmetric photopolymerized microchannels corresponding with distinct pressure levels on the two channels before polymeryzation. Inset d) shows embedded fluorescent nanobeads for TFM applications.

of the PDMS (snapshots d) and e)).

Snapshot b) in Figure 4.6 shows the case of a cusp with R $\sim$ 48.9 μm and where the polymerized interfaces are separated 1 μm from each other. As we demonstrated earlier, the device has a high dynamic range that allows for great controllability of the position of the liquid interface at the cusp of the device, so a separation as small as $\sim$1 μm does not represent a major challenge for our design. Snapshots c) and d) depict the geometry of the interface with $R_m \sim 35.07$ μm and for separations of 5 and 1 μm respectively.

4.3.4 Photopolymerized microchannels

We were finally able to photopolymerize the pre-gel acrylamide solution inside the microchannels following the strategy detailed on 4.6, where the small height of the channel (and hence that of our photopolymerized gels), constituted a real challenge for the photopolymeryzation of acrylamide solutions. The results of individual (inset a)), symmetric (b)) and asymmetric (c)-e)) polymerized hydrogel constrictions are depicted on Figure 4.7.

The inset on Figure 4.7.d shows the distribution of embedded fluorescent nanobeads inside the photopolymerized hydrogel. Ideally, the application of these devices would allow not only for a more physiologically relevant constriction, but would also allow for the three dimensional quantification of traction forces as RBCs travel through the constriction [61].

4.4 Discussion

Migrating cells with mesenchymal behavior typically have to squeeze through small pores during their path [156, 157]. Leukocytes for instance, typically scattered throughout the body, are able to infiltrate any type of tissue when inflammatory or immune responses are triggered [158]. They travel from the bloodstream, across vascular and epithelial monolayers and through the extravascular space with migration velocities that are ∼100 times faster than mesenchymal and epithelial cell types before reaching locations of injury or infection [159]. Cancer cells have also been shown to switch from a predominantly integrin-based motility mode to a much faster amoeboid migration mode via matrix metalloproteinase (MMP) inhibition or depletion [160]. Upon these fast migratory processes, however, these cells sometimes undergo nuclei damage when trying to squeeze through pores of small size [161], and it has been previously reported how constricted migration causes mis-localization of DNA repair proteins and DNA breaks [162]. Although there has been intense focus on the biochemical aspects of the process, very little is still know about the role of mechanics in three dimensional cell migration.

There are also other situations where cells experience rapid velocities in a liquid suspension. This is the case of red blood cells (RBCs) in normal circulation, as we previously discussed in 4.1 when we described RBC's spleen filtration mechanisms [149], but also that of white blood cells in the bloodstream. When circulating in the bloodstream and inactivated, neutrophils are typically rounded in shape. However, once they become activated, they can change shape and become more amorphous or amoeba-like and can extend pseudopods in their search for antigens [163].

Of particular interest is the case of surgical interventions where cardiopulmonary by-

pass (CPB) with moderate hypothermic cardiac arrest (MHCA) is required, such as complex procedures in cardiac surgery. An increase in proinflammatory cytokines and histological changes in the kidney, lung, and liver after CPB has been previously reported [164], in comparison to patients undergoing off-pump coronary artery bypass (OPCAB) [165]. These findings, correlate with elevated leukocyte activation that can result in increased leukocyte infiltration and severe organ damage.

It has been recently hypothesized that neutrophil activation, typically regulated by complex intracellular signaling pathways [166] may be halted and disregulated by mechanical factors during CPB, in particular the shear stresses levels experienced by the circulating cells inside the pump [164, 167], and that could potentially be higher than expected in localized areas of the circuit, resulting in excessive leukocyte activation and also hemolysis [168].

The need for better and closer to physiological conditions in-vitro platforms to study the effect of mechanical shear stress on circulating cells such as Red Blood Cells (RBC) undergoing hemolysis or neutrophils undergoing mechanical activation or priming is beyond any question. Current state of the art platforms have been typically fabricated out of stiff polymers such as PDMS and are far from being optimized.

Inspired by the capillary interfaces of the crosslinked collagen gels observed on the microfluidic platform reported on [169], we came up with the idea of harnessing capillary effects in order to create pre-gel liquid interfaces, as closer as possible to each other, with smooth curvature and in situ photopolymerizable, in order to generate ad hoc flexible constrictions with tunable mechanical properties and surface chemistry.

We designed and developed a microfluidic device with symmetric channels that can create two opposed pre-gel solution liquid interfaces closer to each other. The demonstrated high level of controllability of the relative positions of the liquid interfaces allows for the user to achieve separation gaps of the order of $\sim 1\mu$m. The curvature of the interfaces can also be tuned and designed ahead of time according to capillary action inside the microfluidic device, creating customizable nozzle or constriction geometries.

We were also able to embed fluorescent nanoparticles in the pre-gel solution that could serve as fiduciary markers for Traction Force Microscopy (TFM) applications [61]. The use

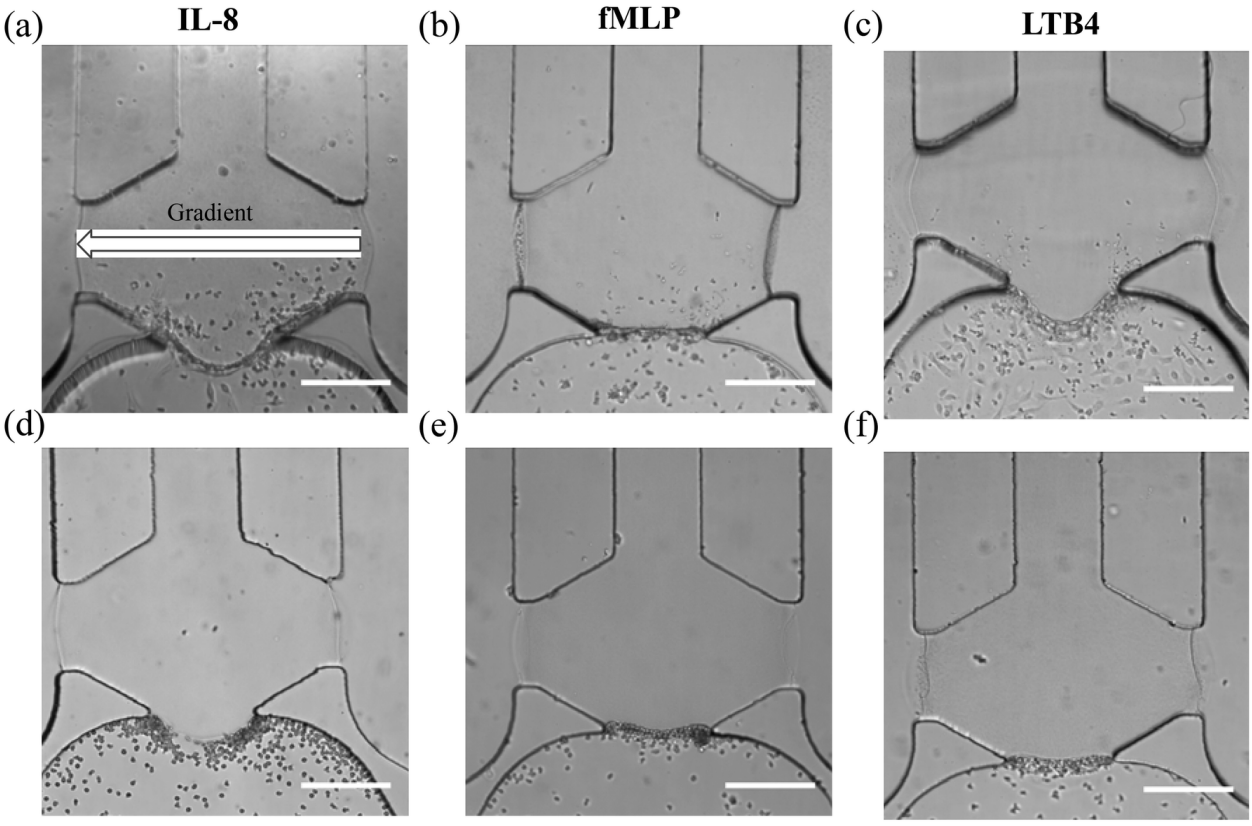

Figure 4.8: Bright-field images of neutrophil TEM 5 h after neutrophil injection under single chemoattractant gradients (gradient direction is indicated in (a)): (a) 50 ng mL-1 of IL-8; (b) 50 ng mL-1 of fMLP; (c) 50 ng mL-1 of LTB4. Bright-field images of neutrophil migration without an endothelial cell layer 5 h after neutrophil injection under single chemoattractant gradients: (d) 50 ng mL-1 of IL-8; (e) 50 ng mL-1 of fMLP; (f) 50 ng mL-1 of LTB4. Endothelial cells cultured in the bottom channel appear to be in elongated shape (30-40 μm) and much larger than the surrounding round neutrophils ($\sim$10 μm). (scale bar: 200 μm). Adapted from [169]

of a photopolymerizable pre-gel solution consisting of acrylamide monomers crosslinked by bis-acrylamide also allows to tune the mechanical properties of the constriction, as well as the surface chemistry of the channel via EDC/NHS chemistry [96].

While several studies in the past ten years have been able to conduct research on the transverse of RBCs through the interendothelial slit (IES) in the human spleen [146, 150, 153, 170–172], they have mostly modeled the process as the passage of flexible structures (RBC, typically represented with with two-component protein-scale models [146]), through totally rigid slits (typically casted in PDMS microfluidic devices of E $\sim$ 2MPa), neglecting the fluid-structure interaction (FSI) problem that would arise from the interaction between the two flexible objects, RBC and slit. Some discrepancies have already been observed between models and the experimental data [153] and although we built on the phenomenal work developed by these groups, we believe that the introduction of a flexible model for the interendothelial slit (despite of the pressence of stress fibers [173] in the axial direction) with customizable mechanical properties and surface chemistry opens a new research avenue for both experimental and computational studies that could most likely get one step closer to a more realistic representation of the process of RBC filtration through interendothelial slits.

However, the process of photopolymerization of a hydrogel solution in regimes where capillary forces dominate and where the surface to volume ratio in contact with porous substrates (PDMS) is rather big, hence allowing for oxygen (a well known reaction inhibitor [132, 174]) to diffuse into the channel through the pores of PDMS, was beyond challenging. Only the introduction of a new photoinitiator with improved water solubility, LAP [85], the reduction of the pore size of the PDMS via introduction of triblock copolymers [175] in the base/curing agent mixture and the pressence of an additional bone dry gas channel adjacent to the main channel that houses the PAAm pre-gel solution (oxygen-purged microfluidic device [176]) allowed for efficient polymerization of our hydrogels in such demanding conditions.

4.5 Conclusions

Current state of the art microfluidic devices that include constrictions to study RBC deformability, leukocyte activation due to shear stress as well as the effect of constricted migration on the nuclear lamina (that has been shown to be mechanoresponsive to ECM elasticity in mature tissue [161]), rely on the fabrication of microchannels containing high aspect ratio sub-micrometer slits casted on stiff PDMS devices, typically using the 10:1 formulation that yields moduli of elasticity as high as ~ 2 MPa [177]. While these platforms have been able to shed light on a remarkable amount of scientific questions involving cellular dynamics of individual cells undergoing strong deformations when transiting through the slits, they are still far from physiological conditions when it comes to mechanical properties of the surrounding tissue. Despite the importance of these transmigration processes there is still a lack of quantitative data available on the deformation and stress distributions of transmigrating cells.

From the preliminary results shown in this chapter, it is clear that improved strategies in the design of microfluidic platforms are required to push the limits of this type of assays from purely qualitative evaluation of the shape deformation of RBCs and other cell types to more quantitative approaches, where stress distributions can be characterized.

In this chapter, we have been able to harness capillary force at the cusps of the microchannels inside our microfluidic devices and polymerize a pre-gel polyacrylamide solution in very demanding conditions. This hydrogels contain fluorescent nanobeads that serve as markers to quantitatively evaluate deformations (and hence stresses) in the polyacrylamide gel. We have also been able to successfully coat our hydrogels with the protein of interest, to reflect a closer to reality fluid structure interaction problem, down top the nanometric scale.

Overall, our newly developed microfluidic device with a photopolymerized polyacrylamide constriction constitutes an important improvement towards the development of new analytical tools in the field of single cell deformability and evaluation of mechanical stresses as a triggering factor for phenotypical changes in circulating cells, such as Red Blood Cells (RBCs), tumor cells or innate immune cells.

4.6 Appendix

4.6.1 Photo-activated polymerization of polyacrylamide hydrogels at the micron scale inside PDMS microfluidic devices

Over the past two decades there has been an increased interest in developing biocompatible materials and composites with mechanical properties ans tructuctural similarity [113] close to those encountered in physiological conditions [178]. In particular, hydrogels (synthetic or extracellular matrix (ECM) derived [129]) and their interaction with other tissues, materials or scaffolds has been thoroughly investigated for their applications on regenerative medicine [130].

Achieving an efficient and resilient bonding of hydrogels to rigid solids (such as glass, ceramics and certain metals) have been recently explored by covalently bonding the stretchy polymer networks of tough hydrogels on surfaces of the solids [179] and included as a standard protocol of hydrogel preparation for Traction Force Microscopy (TFM) applications [30]. In both applications the bonding process includes hydroxilation of silanes that form chemically stable siloxane bonds at the solid interface. Amine groups on amino-silanes can easily react with glutaraldehyde (GA) through a Schiff base reaction [29], forming a stronger bond with amine groups of proteins or acrylamide chains [30]. The use of methacrylated silanes such as silane 3-(trimethoxysilyl) propyl methacrylate (TMSPMA), allows for direct copolymerization of the silane with the the acrylate groups in either acrylamide (AAm) under a free radical polymerization process, generating stable covalently bonded long-chain polymer networks onto the desired solid surfaces [179].

However, a complete explanation on the mechanics behind the bonding process of hydrogels and porous elastomer materials such as PDMS has been more elusive due to the fact that elastomers are tipycally highly permeable to oxygen, being this gas a well known inhibitor of hydrogel polymerization [132]. Basically, molecular oxygen is able to rapidly sequester free radicals reacting with initiator, primary, and growing polymer radicals to form peroxy radicals that are more stable and do not readily reinitiate the polymerization reaction (Fig. 4.9), hence seriously affecting the hydrogel free-radical based polymerization

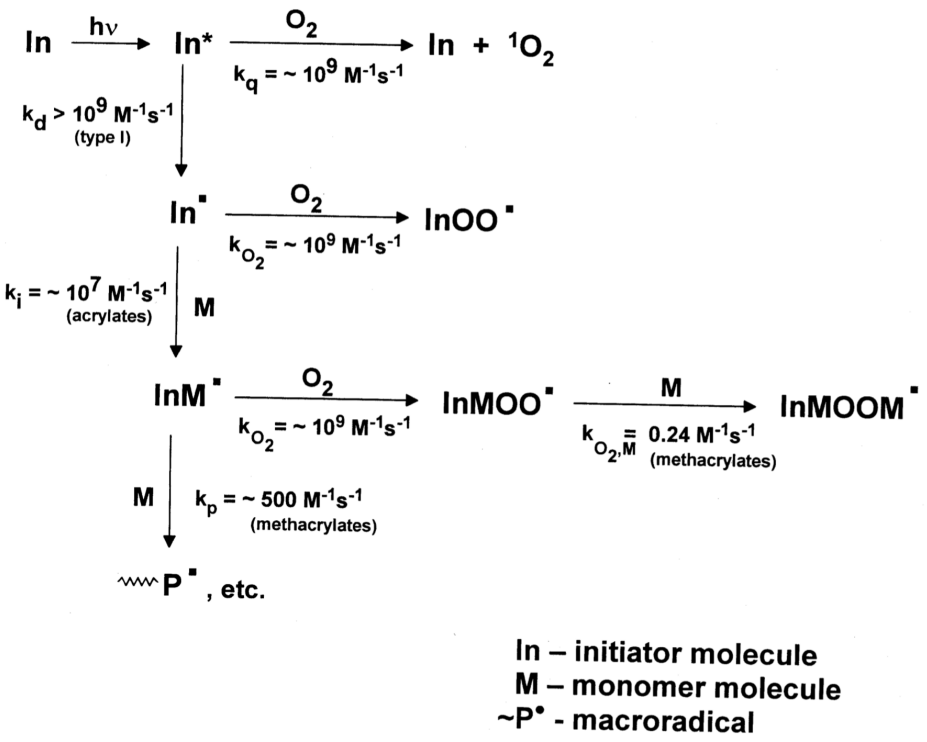

Figure 4.9: Effect of oxygen concentration on photopolymerization. Adapted from [132]

process or even the surface covalent crosslinking process of the hydrogel with the elastomer [174].

Several studies in the past five years have proposed efficient strategies to assemble hydrogels and elastomers into hybrids with robust interfaces, overcoming the undesired pressence of oxygen at the interface [180] mostly through the use of benzophenone [181], an organic compound predominantly used as a photo initiator in UV-curing applications such as inks and clear coatings in the printing industry. Implantation of benzophenone into the surface of PDMS is typically done taking advantage of the fact that acetone-induced swelling of the elastomer led to the diffusion of benzophenone into the PDMS walls of a microchannel. After that process, UV-initiated decomposition of benzophenone generates free radicals within the PDMS that directly initiates polymerization of acrylic acid, resulting in the polyacrylamide (PAAm) gel and the PDMS forming an interpenetrating polymer network to a depth of 50 μm and protruding 150 nm above the PDMS surface [182].

The presence of oxygen inhibits the polymerization reaction specially at the capillary

level. In the case of our microchannel device, the dimensions of the channel are typically 20-40 μm width and 5 μm high. This restrictive dimensions (specially in height) come motivated by the need of small constrictions required to accurately reproduce RBC spleen filtration events. When trying to photo-polymerize our acrylamide solution inside the microchannel we found out that most of the times the solution would not polymerize inside the microfluidic device, regardless of the concentration of photoinitiator (kept in reasonable levels of $\leq$ 100mM) or the time we exposed the solution to the UV lamp (ranging between 3min - 15min). This led us to hypothesize the presence of an "oxygen boundary layer" on top of the PDMS substrate that in our case might be tall enough ($\sim$5 μm) as to completely inhibit the PAAm polymerization reaction inside the device [174, 183].

In order to test this hypothesis we conducted a series of experiments to help us understand the mechanics of PAAm polymerization inside microfluidic devices of small height (h $\leq$ 10 μm). We tried to photopolymerize droplets of our pre-gel solution of 3 μL in volume on top of several surfaces, as shown on table 4.1, with and without a top 12mm round coverslip to simulate the capillary regime in the desired cases (Fig. 4.10).

From these set of experiments, we confirmed that polymerization of capillary layers of PAAm solution would not polymerize on top of untreated PDMS surfaces with a coverslip on top (to simulate the capillary thickness), regardless of the photoinitiator chosen, hence reproducing the behavior observed inside the microfluidic device and somehow confirming the localization of the problem to the surface of the elastomer. Polymerization results from experiments depicted on Fig.4.10 are summarized in Table 4.1.

The previously described benzophenone-based polymer grafting strategies did not seem appropriate for our application, since they usually cause PDMS swelling that can be significant at the capillary scale and they can also modify the mechanical properties of the hydrogel, since the release of free radicals with UV exposure is not very well controlled.

After unsuccesfully trying reduced concentrations of base:curing agent (10:1, 5:1, 4:1) in an attempt to reduce pore size and oxygen permeability in PDMS [184] and degassing our microfluidic devices in vacuum for 24h (which also did not work as expected), we subsequently explored recent surface chemistry modification strategies that several groups have used in

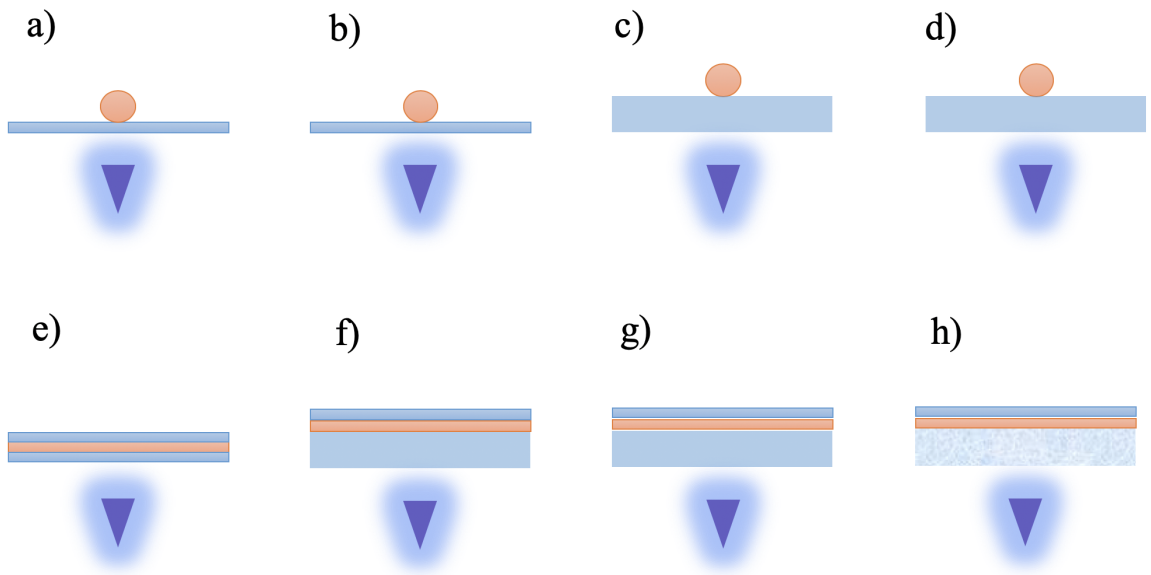

Figure 4.10: UV photopolymerization of PolyAcrylamide (PAAm) solutions (3 μL) on top of different substrates. a) Glass coverslip without cover and I2959 as photoinitiator (PI). b) Glass coverslip without cover and Lithium phenyl-2,4,6-trimethylbenzoylphosphinate (LAP) as PI. c) PDMS and no cover and I2959 as PI. d) c) PDMS and no cover and LAP as PI. e) Glass coverslip, LAP as PI and glass coverslip as a cover. f) PDMS, I2959 as PI and glass coverslip as a cover. g) PDMS, LAP as PI and glass coverslip as a cover. h) PDMS with Pluronics, LAP as PI and glass coverslip as a cover.

the past as a way to achieve nonbiofouling PDMS surface [185, 186]. Most of these surface modifications have been oriented at rendering a more durable hydrophillic surface in the PDMS or coating with specific molecules in order for the surfaces to serve as biomolecular detectors via immunoassays and even though plasma treatment does create a diffusional barrier that significantly reduces the amount of oxygen partitioning into PDMS [184], this did not seem to be enough to prevent the inhibition of polymerization near the surface for the restrictive case of $\sim$1 μm tall hydrogels inside our microfluidic devices.

Inspired by the fact that PDMS is a good solid solvent, we decided to adapt a rather simple strategy to achieve surface modification of PDMS substrates based on gradient-induced migration of Pluronic molecules inside the PDMS microfludic device [175], in order to reduce porosity at the surface to prevent the formation of the oxygen inhibition layer [152, 176]. Basically, we dissolved a small amount of Pluronic powder (Sigma-Aldrich, St. Louis, MO) in ethanol to an approximate concentration of 200mg/mL and mixed 20 μL of this solution with 10g of 10:1 PDMS base:curing agent mixture. The curing and bonding process were exactly the same as described previously in 4.2 for previous microfluidic devices casted on top of silicon masters.

Pluronics belongs to a group of triblock copolymers with the general composition of $(PEO)_m(PPO)_n(PEO)_m$, with m=100, n = 65 for the case of Pluronics F127, used in this study, constituting two poly(ethylene oxide) (PEO) hydrophilic branches and one hydrophobic polypropylene oxide (PPO) branch. Even with the presence of the later, Pluronics molecules are much more soluble in water than in PDMS and consequently, when water is present in the channels of the microfluidic device the Pluronic molecules embedded inside the PDMS are able to migrate towards the water interface. A rather dense single molecular layer is formed on the channel surface with the hydrophilic branches of the co-polymer facing outwards (Fig. 4.11).

After casting a PDMS sample with the new Pluronic formulation, we repeated the experiment of polymerization on top of a PDMS block covered with a 12mm coverslip obtaining a satisfactory polymerization reaction this time, confirming the hypothesis that, under these conditions, the oxygen inhibition layer height is in this case much smaller, allowing

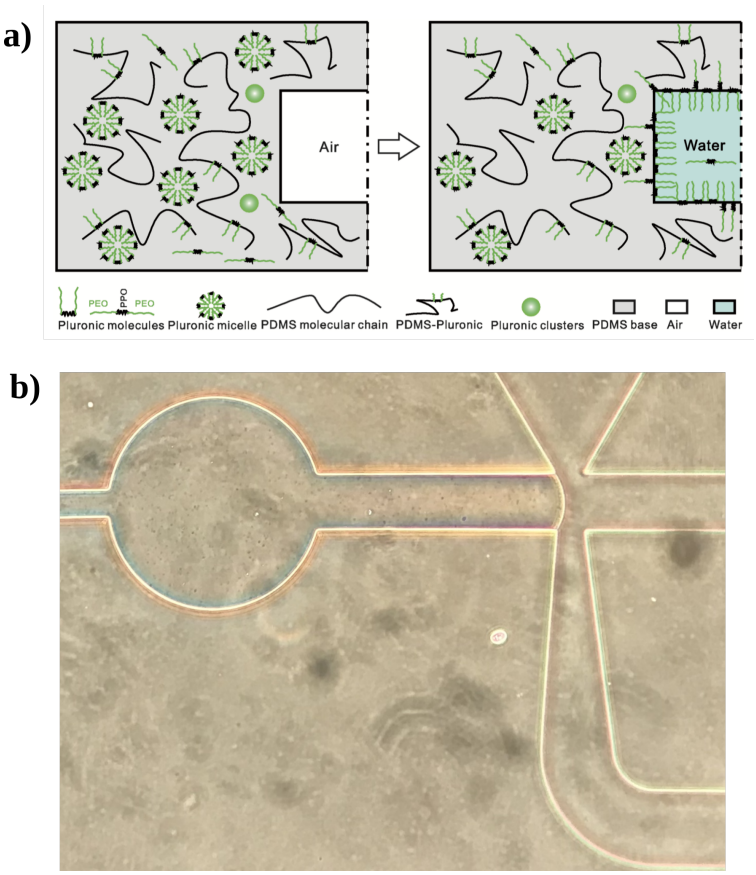

Figure 4.11: a) Schematics of the process of surface modification based on gradient-induced migration of Pluronic toward the water channel inside microfluidic devices. Adapted from [175]. b) Resulting microchannel polymerization with Pluronic PDMS formulation

for the full polymerization of the gel under capillary conditions (Fig. 4.10.h). This is most likely due to the presence of a dense network (oversaturated even at the low concentration of 2 μL/g according to [175]) of polymer branches that hinders the diffusion and replenishment of molecular oxygen to the surface of the microfluidic device.

Under these conditions, we casted a new microfluidic device with the usual microchannel design and successfully polymerized the capillary driven hydrogel interface inside the channels of the microfluidic device, as depicted on Fig. 4.11.b.

To further boost the robustness of the process, we also introduced a nitrogen micro-jacketed extra layer to our microfluidic device in order to purge oxygen from flowing fluids during photopolymerization, as previously reported in [176].

Table 4.1: UV photopolymerization of PolyAcrylamide samples. PolyAcrlylamide droplets were polymerized on top of glass coverslips or PDMS substrates and with and without coverslip covers.

Sample	Substrate	Photoinitiator	Cover	UV exposure (min)	Polym.
a)	glass cover.	Irgacure (2mM)	none	1.5 min	YES
b)	glass cover.	LAP (2mM)	none	1.5 min	YES
c)	PDMS	Irgacure (2mM)	none	1.5 min	NO
d)	PDMS	LAP (2mM)	none	1.5 min	YES
e)	glass cover.	LAP (2mM)	glass cover.	1.5 min	YES
f)	PDMS	Irgacure (2mM)	glass cover.	1.5 min	NO
g)	PDMS	LAP (2mM)	glass cover.	1.5 min	NO
h)	PDMS + Pluronic	LAP (2mM)	glass cover.	1.5 min	YES

4.7 Acknowledgements

Chapter 4, in part is currently being prepared for submission for publication of the material. Criado-Hidalgo, Ernesto; Garcia-Herreros, Antoni; Yeh, Yi-Ting; Lasheras Juan C.; del Álamo, Juan C. The dissertation author was the primary investigator and author of this material.

Chapter 5

Concluding Remarks

A brief summary of the main conclusions achieved in this dissertation is presented in this chapter, a more detailed discussion can be found at the end of each chapter.

The present work has been mostly focused on the development of methodologies to study mechanobiology problems of great relevance in biology and physiology. We have also presented preliminary data on the understanding of the interaction of epithelial tissue with three dimensional obstacles of different stiffness while trying to maintain tissue integrity, as well as the interaction of vascular endothelial cells with elastic round hydrogels and red blood cells on their passage through narrow constrictions of elastic properties.

On Chapter 2 of this dissertation we have developed a series of microfabricated assays and image processing techniques to be applied to the study of collective cell migration of epithelial monolayers in the presence of obstacles. Traditional assays studying collective cell migration of epithelial layers have been restricted to two-dimensional assays, however, realistic and physiologically relevant scenarios require three-dimensional configurations and understanding the implications of the changes in cell polarity and directionality that could originate from the availability of unrestricted physical space for migration. We studied the effect of adherent and non-fouling coatings in three-dimensionsional pillars as well as a the long term interaction of epithelial layers with flexible objects coated with proteins of interest. We observed completely different behaviors when collagen, the adhesion protein E-Cadherin or the non-fouling protein PLL-PEG were presented to the monolayer. Interestingly enough,

monolayers were able to engulf the non-fouling obstacle and preserve integrity in a similar manner as what was reported previoulsy in two-dimensional assays with non-adherent regions [13]. A relatively high level of intarecellular tension in the monolayer, necessary for tissue integrity without integrin adhesions in non-adherent obstacles, resulted in rupture of the monolayer, as shown in through SEM imaging.

In this chapter we also put forward the hypothesis of Piezo1 playing a significant role in Contact Inhibition of Proliferation (CIP) through the Hippo pathway. Several hypothesis or explanations have been published in the past trying to explain the mechanistic details of this process that has deep implications in tissue integrity, development and homeostasis in general [50], however, a complete understanding is yet to be achieved. Key actors in the process are mechanosensitive proteins, such as E-Cadherin and their link to growth factors [187, 188]. We overexpressed the mechanosensitive ion channel Piezo1 in our developed epithelial cell lines and observed how the machanism that permits YAP translocate away from the nucleus in dense or overconfluent configurations, thus slowing down cell proliferation in dense configurations, seems to be inactive in Piezo1 overexpressed cell lines, revealing Piezo1 as a key actor in CIP.

On Chapter 3 of this dissertation we have developed a series of microfluidic devices capable of manufacturing small, monodisperse, biocompatible elastic round hydrogels for cell generated force quantification in three-dimensional assays or even in vivo. We present a novel strategy that uses a photoinitiated PolyAcrylamide (PAAm) polymerization reaction to generate the hydrogels from previously emulsified pre-gel solutions. The main advantage of our protocol is the use of a photoinitiator with increased water solubility, LAP, and with improved biocompatibility and reaction kinetics than I2959, the standard in photoinitiated polymerized PAAm hydrogels for cell mechanics applications. This advantages allow for an increased homogeneity on the polymerization reaction yielding mechanical properties of the hydrogels similar to those reported previously for APS initiated gels and that have been considered the standard in the field [30].

The easiness of use of our methodology, that does not require complex assays or involved pH-dependent polymerization processes, as well as the biocompatibility of our hy-

drogels constitutes key advantages that could potentially transform this protocol and technique into one of the standards of three-dimensional force quantification in cell and tissue mechanics.

On Chapter 4 of this dissertation we have developed a set of microfluidic devices where we harnessed capillary stresses at the cusp creating elastic constrictions of small size ($\sim$1 μm) that serve as gaps where cells have to squeeze through in their passage through the microfluidic device. Cells sometimes have to squeeze through narrow gaps in their life cycle. Examples from this are red blood cell filtration at the spleen, cancer cell migration through tissue or even leukocytes undergoing phenotypical changes due to mechanical stresses in bypass surgeries. Despite the relevance of these scenarios, the levels of stress that cells undergo in such situations are hard to quantify mostly due to the lack of devices and methodologies that can offer a reliable and systematic way of quantifying mechanical stresses at the micrometric level. Even to this day, there are no quantitative measurements of mechanical stress at this lenghscale to our knowledge. With the devices that we engineered, we can generate micrometric size hydrogels seeded with fluorescent nanobeads acting as fiduciary markers for gel deformability. We basically used capillary flows to position the pre-gel solution at the cusp of our devices and posteriorly polymerize with UV light, thus generating PAAm hydrogel elastic constrictions that would deform with cells squeezing through them, allowing for mechanical stress quantification in such scenarios.

Bibliography

[1] Ray Keller, Lance Davidson, Anna Edlund, Tamira Elul, Max Ezin, David Shook, and Paul Skoglund. Mechanisms of convergence and extension by cell intercalation. *Philosophical Transactions of the Royal Society of London. Series B: Biological Sciences*, 355(1399):897–922, 2000.

[2] Ray Keller. Shaping the vertebrate body plan by polarized embryonic cell movements. *Science*, 298(5600):1950–1954, 2002.

[3] Benoit Ladoux and René-Marc Mège. Mechanobiology of collective cell behaviours. *Nature Reviews Molecular Cell Biology*, 18(12):743, 2017.

[4] Xingbo Yang, Dapeng Bi, Michael Czajkowski, Matthias Merkel, M Lisa Manning, and M Cristina Marchetti. Correlating cell shape and cellular stress in motile confluent tissues. *Proceedings of the National Academy of Sciences*, 114(48):12663–12668, 2017.

[5] Daniel J Cohen, Martijn Gloerich, and W James Nelson. Epithelial self-healing is recapitulated by a 3d biomimetic e-cadherin junction. *Proceedings of the National Academy of Sciences*, 113(51):14698–14703, 2016.

[6] Ninna S Rossen, Jens M Tarp, Joachim Mathiesen, Mogens H Jensen, and Lene B Oddershede. Long-range ordered vorticity patterns in living tissue induced by cell division. *Nature communications*, 5:5720, 2014.

[7] Pilar Rodríguez-Franco, Agustí Brugués, Ariadna Marín-Llauradó, Vito Conte, Guiomar Solanas, Eduard Batlle, Jeffrey J Fredberg, Pere Roca-Cusachs, Raimon Sunyer, and Xavier Trepat. Long-lived force patterns and deformation waves at repulsive epithelial boundaries. *Nature materials*, 16(10):1029, 2017.

[8] Xavier Serra-Picamal, Vito Conte, Romaric Vincent, Ester Anon, Dhananjay T Tambe, Elsa Bazellieres, James P Butler, Jeffrey J Fredberg, and Xavier Trepat. Mechanical waves during tissue expansion. *Nature Physics*, 8(8):628, 2012.

[9] S Tlili, E Gauquelin, B Li, O Cardoso, B Ladoux, H Delanoë-Ayari, and F Graner. Waves in cell monolayer without proliferation: density determines cell velocity and wave celerity. *Preprint at http://arXiv. org/abs/1610.05420*, 2016.

[10] Shiladitya Banerjee, Kazage JC Utuje, and M Cristina Marchetti. Propagating stress waves during epithelial expansion. *Physical review letters*, 114(22):228101, 2015.

[11] Ester Anon, Xavier Serra-Picamal, Pascal Hersen, Nils C Gauthier, Michael P Sheetz, Xavier Trepat, and Benoît Ladoux. Cell crawling mediates collective cell migration to close undamaged epithelial gaps. *Proceedings of the National Academy of Sciences*, 109(27):10891–10896, 2012.

[12] Sri Ram Krishna Vedula, Hiroaki Hirata, Mui Hoon Nai, Yusuke Toyama, Xavier Trepat, Chwee Teck Lim, and Benoit Ladoux. Epithelial bridges maintain tissue integrity during collective cell migration. *Nature materials*, 13(1):87, 2014.

[13] Sri Ram Krishna Vedula, Grégoire Peyret, Ibrahim Cheddadi, Tianchi Chen, Agustí Brugués, Hiroaki Hirata, Horacio Lopez-Menendez, Yusuke Toyama, Luís Neves De Almeida, Xavier Trepat, Chwee Teck Lim, and Benoit Ladoux. Mechanics of epithelial closure over non-adherent environments. *Nature communications*, 6:6111, 2015.

[14] Hannah G Yevick, Guillaume Duclos, Isabelle Bonnet, and Pascal Silberzan. Architecture and migration of an epithelium on a cylindrical wire. *Proceedings of the National Academy of Sciences*, 112(19):5944–5949, 2015.

[15] Otger Campàs, Tadanori Mammoto, Sean Hasso, Ralph A Sperling, Daniel O'connell, Ashley G Bischof, Richard Maas, David A Weitz, Lakshminarayanan Mahadevan, and Donald E Ingber. Quantifying cell-generated mechanical forces within living embryonic tissues. *Nature methods*, 11(2):183, 2014.

[16] Nicole Traeber, Klemens Uhlmann, Salvatore Girardo, Gokul Kesavan, Katrin Wagner, Jens Friedrichs, Ruchi Goswami, Keliya Bai, Michael Brand, Carsten Werner, Daniel Balzani, and Jochen Guck. Polyacrylamide bead sensors for in vivo quantification of cell-scale stress in zebrafish development. *Scientific reports*, 9(1):1–14, 2019.

[17] Daan Vorselen, Yifan Wang, Matthew J Footer, Wei Cai, and Julie A Theriot. Super-resolved and reference-free microparticle traction force microscopy (mp-tfm) reveals the complexity of the mechanical interaction in phagocytosis. *bioRxiv*, page 431221, 2018.

[18] Christopher C DuFort, Matthew J Paszek, and Valerie M Weaver. Balancing forces: architectural control of mechanotransduction. *Nature reviews Molecular cell biology*, 12(5):308–319, 2011.

[19] A Wayne Orr, Brian P Helmke, Brett R Blackman, and Martin A Schwartz. Mechanisms of mechanotransduction. *Developmental cell*, 10(1):11–20, 2006.

[20] Donald E Ingber. Mechanical control of tissue morphogenesis during embryological development. *International Journal of Developmental Biology*, 50(2-3):255–266, 2003.

[21] Tadanori Mammoto and Donald E Ingber. Mechanical control of tissue and organ development. *Development*, 137(9):1407–1420, 2010.

[22] Hiroko Kita-Matsuo, Maria Barcova, Natalie Prigozhina, Nathan Salomonis, Karen Wei, Jeffrey G Jacot, Brandon Nelson, Sean Spiering, René Haverslag, Changsung Kim, Maria Talantova, Ruchi Bajpai, Diego Calzolari, Alexey Terskikh, Andrew D. McCulloch, Jeffrey H. Price, Bruce R. Conklin, H. S. Vincent Chen, and Mark Mercola. Lentiviral vectors and protocols for creation of stable hesc lines for fluorescent tracking and drug resistance selection of cardiomyocytes. *PloS one*, 4(4), 2009.

[23] Kevin C Miranda, Tatiana Khromykh, Perpetina Christy, Tam Luan Le, Cara J Gottardi, Jennifer L Stow, and Rohan D Teasdale. A dileucine motif targets e-cadherin to the basolateral cell surface in madin-darby canine kidney and llc-pk1 epithelial cells. *Journal of Biological Chemistry*, 276(25):22565–22572, 2001.

[24] Bertrand Coste, Jayanti Mathur, Manuela Schmidt, Taryn J Earley, Sanjeev Ranade, Matt J Petrus, Adrienne E Dubin, and Ardem Patapoutian. Piezo1 and piezo2 are essential components of distinct mechanically activated cation channels. *Science*, 330(6000):55–60, 2010.

[25] Chris A Kaiser, Monty Krieger, Harvey Lodish, and Arnold Berk. *Molecular cell biology.* WH Freeman, 2007.

[26] Michael R Green and Joseph Sambrook. Molecular cloning. *A Laboratory Manual 4th*, 2012.

[27] Juan C Del Alamo, Ruedi Meili, Baldomero Alonso-Latorre, Javier Rodríguez-Rodríguez, Alberto Aliseda, Richard A Firtel, and Juan C Lasheras. Spatio-temporal analysis of eukaryotic cell motility by improved force cytometry. *Proceedings of the National Academy of Sciences*, 104(33):13343–13348, 2007.

[28] Yi-Ting Yeh, Ricardo Serrano, Joshua François, Jeng-Jiann Chiu, Yi-Shuan Julie Li, Juan C Del Álamo, Shu Chien, and Juan C Lasheras. Three-dimensional forces exerted by leukocytes and vascular endothelial cells dynamically facilitate diapedesis. *Proceedings of the National Academy of Sciences*, 115(1):133–138, 2018.

[29] Yi Jia and Junbai Li. Molecular assembly of schiff base interactions: construction and application. *Chemical reviews*, 115(3):1597–1621, 2014.

[30] Justin R Tse and Adam J Engler. Preparation of hydrogel substrates with tunable mechanical properties. *Current protocols in cell biology*, 47(1):10–16, 2010.

[31] Begoña Álvarez-González, Shun Zhang, Manuel Gómez-González, Ruedi Meili, Richard A Firtel, Juan C Lasheras, and Juan C Del Álamo. Two-layer elastographic 3-d traction force microscopy. *Scientific reports*, 7:39315, 2017.

[32] Younan Xia and George M Whitesides. Soft lithography. *Annual review of materials science*, 28(1):153–184, 1998.

[33] Michael T Yang, Jianping Fu, Yang-Kao Wang, Ravi A Desai, and Christopher S Chen. Assaying stem cell mechanobiology on microfabricated elastomeric substrates with geometrically modulated rigidity. *Nature protocols*, 6(2):187, 2011.

[34] Jessamine Ng Lee, Cheolmin Park, and George M Whitesides. Solvent compatibility of poly (dimethylsiloxane)-based microfluidic devices. *Analytical chemistry*, 75(23):6544–6554, 2003.

[35] John H Koschwanez, Robert H Carlson, and Deirdre R Meldrum. Thin pdms films using long spin times or tert-butyl alcohol as a solvent. *PLoS one*, 4(2):e4572, 2009.

[36] C Redon, JB Brzoska, and F Brochard-Wyart. Dewetting and slippage of microscopic polymer films. *Macromolecules*, 27(2):468–471, 1994.

[37] Marianne E Harmon, Mary Tang, and Curtis W Frank. A microfluidic actuator based on thermoresponsive hydrogels. *Polymer*, 44(16):4547–4556, 2003.

[38] Katharine E Jensen, Raphael Sarfati, Robert W Style, Rostislav Boltyanskiy, Aditi Chakrabarti, Manoj K Chaudhury, and Eric R Dufresne. Wetting and phase separation in soft adhesion. *Proceedings of the National Academy of Sciences*, 112(47):14490–14494, 2015.

[39] Curtis T Rueden, Johannes Schindelin, Mark C Hiner, Barry E DeZonia, Alison E Walter, Ellen T Arena, and Kevin W Eliceiri. Imagej2: Imagej for the next generation of scientific image data. *BMC bioinformatics*, 18(1):529, 2017.

[40] Ali M Reza. Realization of the contrast limited adaptive histogram equalization (clahe) for real-time image enhancement. *Journal of VLSI signal processing systems for signal, image and video technology*, 38(1):35–44, 2004.

[41] Zoran Zivkovic. Improved adaptive gaussian mixture model for background subtraction. In *Proceedings of the 17th International Conference on Pattern Recognition, 2004. ICPR 2004.*, volume 2, pages 28–31. IEEE, 2004.

[42] Raghuveer Parthasarathy. Rapid, accurate particle tracking by calculation of radial symmetry centers. *Nature methods*, 9(7):724, 2012.

[43] Junghyun Kim, Sewoon Han, Andy Lei, Masaru Miyano, Jessica Bloom, Vasudha Srivastava, Martha R Stampfer, Zev J Gartner, Mark A LaBarge, and Lydia L Sohn. Characterizing cellular mechanical phenotypes with mechano-node-pore sensing. *Microsystems & nanoengineering*, 4(1):1–12, 2018.

[44] S. Girardo, N. Traeber, K. Wagner, G. Cojoc, C. Herold, R. Goswami, R. Schluessler, S. Abuhattum, A. Taubenberger, F. Reichel, D. Mokbel, M. Herbig, M. Schurmann, P. Muller, T. Heida, A. Jacobi, E. Ulbricht, J. Thiele, C. Werner, and J. Guck. Standardized microgel beads as elastic cell mechanical probes. *Journal of Materials Chemistry B*, 6(39):6245–6261, 2018.

[45] Steven M Zehnder, Melanie Suaris, Madisonclaire M Bellaire, and Thomas E Angelini. Cell volume fluctuations in mdck monolayers. *Biophysical journal*, 108(2):247–250, 2015.

[46] Yosiyuki Sakamoto, Makio Ishiguro, and Genshiro Kitagawa. Akaike information criterion statistics. *Dordrecht, The Netherlands: D. Reidel*, 81, 1986.

[47] Sheldon Weinbaum, Peng Guo, and Lidan You. A new view of mechanotransduction and strain amplification in cells with microvilli and cell processes. *Biorheology*, 38(2, 3):119–142, 2001.

[48] Akira Nagafuchi, Yasuaki Shirayoshi, Kenji Okazaki, Kunio Yasuda, and Masatoshi Takeichi. Transformation of cell adhesion properties by exogenously introduced e-cadherin cdna. *Nature*, 329(6137):341–343, 1987.

[49] Mireille Lambert, Françoise Padilla, and René Marc Mège. Immobilized dimers of n-cadherin-fc chimera mimic cadherin-mediated cell contact formation: contribution of both outside-in and inside-out signals. *Journal of cell science*, 113(12):2207–2219, 2000.

[50] Andrea I McClatchey and Alpha S Yap. Contact inhibition (of proliferation) redux. *Current opinion in cell biology*, 24(5):685–694, 2012.

[51] Swapna A Gudipaty, Jody Lindblom, Patrick D Loftus, Michael J Redd, Kornelia Edes, CF Davey, V Krishnegowda, and Jody Rosenblatt. Mechanical stretch triggers rapid epithelial cell division through piezo1. *Nature*, 543(7643):118, 2017.

[52] Thuan Beng Saw, Amin Doostmohammadi, Vincent Nier, Leyla Kocgozlu, Sumesh Thampi, Yusuke Toyama, Philippe Marcq, Chwee Teck Lim, Julia M Yeomans, and Benoit Ladoux. Topological defects in epithelia govern cell death and extrusion. *Nature*, 544(7649):212, 2017.

[53] Nam-Gyun Kim, Eunjin Koh, Xiao Chen, and Barry M Gumbiner. E-cadherin mediates contact inhibition of proliferation through hippo signaling-pathway components. *Proceedings of the National Academy of Sciences*, 108(29):11930–11935, 2011.

[54] Stefano Piccolo, Sirio Dupont, and Michelangelo Cordenonsi. The biology of yap/taz: hippo signaling and beyond. *Physiological reviews*, 94(4):1287–1312, 2014.

[55] Matthew J Paszek, Nastaran Zahir, Kandice R Johnson, Johnathon N Lakins, Gabriela I Rozenberg, Amit Gefen, Cynthia A Reinhart-King, Susan S Margulies, Micah Dembo, David Boettiger, David Hammer, and Valerie Weaver. Tensional homeostasis and the malignant phenotype. *Cancer cell*, 8(3):241–254, 2005.

[56] Adam J Engler, Shamik Sen, H Lee Sweeney, and Dennis E Discher. Matrix elasticity directs stem cell lineage specification. *Cell*, 126(4):677–689, 2006.

[57] Ning Wang, Jessica D Tytell, and Donald E Ingber. Mechanotransduction at a distance: mechanically coupling the extracellular matrix with the nucleus. *Nature reviews Molecular cell biology*, 10(1):75, 2009.

[58] Friedhelm Serwane, Alessandro Mongera, Payam Rowghanian, David A Kealhofer, Adam A Lucio, Zachary M Hockenbery, and Otger Campàs. In vivo quantification of spatially varying mechanical properties in developing tissues. *Nature methods*, 14(2):181, 2017.

[59] Pierre-Gilles De Gennes, Françoise Brochard-Wyart, and David Quéré. *Capillarity and wetting phenomena: drops, bubbles, pearls, waves*. Springer Science & Business Media, 2013.

[60] Erfan Mohagheghian, Junyu Luo, Junjian Chen, Gaurav Chaudhary, Junwei Chen, Jian Sun, Randy H Ewoldt, and Ning Wang. Quantifying compressive forces between living cell layers and within tissues using elastic round microgels. *Nature communications*, 9(1):1878, 2018.

[61] Juan C Del Álamo, Ruedi Meili, Begoña Álvarez-González, Baldomero Alonso-Latorre, Effie Bastounis, Richard Firtel, and Juan C Lasheras. Three-dimensional quantification of cellular traction forces and mechanosensing of thin substrata by fourier traction force microscopy. *PloS one*, 8(9):e69850, 2013.

[62] Howard A Stone, Abraham D Stroock, and Armand Ajdari. Engineering flows in small devices: microfluidics toward a lab-on-a-chip. *Annu. Rev. Fluid Mech.*, 36:381–411, 2004.

[63] Shelley L Anna, Nathalie Bontoux, and Howard A Stone. Formation of dispersions using "flow focusing" in microchannels. *Applied physics letters*, 82(3):364–366, 2003.

[64] Piotr Garstecki, Irina Gitlin, Willow DiLuzio, George M Whitesides, Eugenia Kumacheva, and Howard A Stone. Formation of monodisperse bubbles in a microfluidic flow-focusing device. *Applied Physics Letters*, 85(13):2649–2651, 2004.

[65] Alfonso M Ganán-Calvo and José M Gordillo. Perfectly monodisperse microbubbling by capillary flow focusing. *Physical review letters*, 87(27):274501, 2001.

[66] Alfonso M Ganán-Calvo. Perfectly monodisperse microbubbling by capillary flow focusing: An alternate physical description and universal scaling. *Physical Review E*, 69(2):027301, 2004.

[67] DR Link, Shelley L Anna, DA Weitz, and Howard A Stone. Geometrically mediated breakup of drops in microfluidic devices. *Physical review letters*, 92(5):054503, 2004.

[68] Prabhakara Satyauolu Rao. Dispersant in non-polar solvent, May 13 2003. US Patent 6,562,889.

[69] Michael H Rausch, Lorenz Kretschmer, Stefan Will, Alfred Leipertz, and Andreas P Fröba. Density, surface tension, and kinematic viscosity of hydrofluoroethers hfe-7000, hfe-7100, hfe-7200, hfe-7300, and hfe-7500. *Journal of chemical & engineering data*, 60(12):3759–3765, 2015.

[70] JR Haliburton, SC Kim, IC Clark, RA Sperling, DA Weitz, and AR Abate. Efficient extraction of oil from droplet microfluidic emulsions. *Biomicrofluidics*, 11(3):034111, 2017.

[71] Nicholas R Labriola, Edith Mathiowitz, and Eric M Darling. Fabricating polyacrylamide microbeads by inverse emulsification to mimic the size and elasticity of living cells. *Biomaterials science*, 5(1):41–45, 2017.

[72] James J Cody, Wannaporn Ittiprasert, André N Miller, Lucie Henein, Margaret M Mentink-Kane, and Michael H Hsieh. The nih-niaid schistosomiasis resource center at the biomedical research institute: Molecular redux. *PLoS neglected tropical diseases*, 10(10):e0005022, 2016.

[73] JP Dalton, SR Day, AC Drew, and PJ Brindley. A method for the isolation of schistosome eggs and miracidia free of contaminating host tissues. *Parasitology*, 115(1):29–32, 1997.

[74] PD Ashton, R Harrop, B Shah, and RA Wilson. The schistosome egg: development and secretions. *Parasitology*, 122(3):329–338, 2001.

[75] Johannes Schindelin, Ignacio Arganda-Carreras, Erwin Frise, Verena Kaynig, Mark Longair, Tobias Pietzsch, Stephan Preibisch, Curtis Rueden, Stephan Saalfeld, Benjamin Schmid, Jean-Yves Tinevez, Daniel James White, Volker Hartenstein, Kevin Eliceiri, Pavel Tomancak, and Albert Cardona. Fiji: an open-source platform for biological-image analysis. *Nature methods*, 9(7):676, 2012.

[76] Tony F Chan and Luminita A Vese. Active contours without edges. *IEEE Transactions on image processing*, 10(2):266–277, 2001.

[77] Christopher R Madan. Creating 3d visualizations of mri data: A brief guide. *F1000Research*, 4, 2015.

[78] JE Sader. Calibration of atomic force microscope cantilevers. *Encyclopedia of Surface and Colloid Science*, 846, 2002.

[79] Ian N Sneddon. The relation between load and penetration in the axisymmetric boussinesq problem for a punch of arbitrary profile. *International journal of engineering science*, 3(1):47–57, 1965.

[80] GG Bilodeau. Regular pyramid punch problem. 1992.

[81] B Bergenståhl and Per M Claesson. Surface forces in emulsions. 1997.

[82] Dérick Rousseau. Fat crystals and emulsion stability—a review. *Food Research International*, 33(1):3–14, 2000.

[83] E Dickinson and CM Woskett. Competitive adsorption between proteins and small-molecule surfactants in food emulsions. *Food colloids*, pages 74–96, 1989.

[84] Tetsuro Majima, Wolfram Schnabel, and Wilhelm Weber. Phenyl-2, 4, 6-trimethylbenzoylphosphinates as water-soluble photoinitiators. generation and reactivity of o=$\dot{P}$ (c6h5)(o-) radical anions. *Die Makromolekulare Chemie: Macromolecular Chemistry and Physics*, 192(10):2307–2315, 1991.

[85] Benjamin D Fairbanks, Michael P Schwartz, Christopher N Bowman, and Kristi S Anseth. Photoinitiated polymerization of peg-diacrylate with lithium phenyl-2, 4, 6-trimethylbenzoylphosphinate: polymerization rate and cytocompatibility. *Biomaterials*, 30(35):6702–6707, 2009.

[86] Stephan Benedikt, Jieping Wang, Marica Markovic, Norbert Moszner, Kurt Dietliker, Aleksandr Ovsianikov, Hansjörg Grützmacher, and Robert Liska. Highly efficient water-soluble visible light photoinitiators. *Journal of Polymer Science Part A: Polymer Chemistry*, 54(4):473–479, 2016.

[87] Saroja Ramanujan, Alain Pluen, Trevor D McKee, Edward B Brown, Yves Boucher, and Rakesh K Jain. Diffusion and convection in collagen gels: implications for transport in the tumor interstitium. *Biophysical journal*, 83(3):1650–1660, 2002.

[88] Ya-li Yang, Stéphanie Motte, and Laura J Kaufman. Pore size variable type i collagen gels and their interaction with glioma cells. *Biomaterials*, 31(21):5678–5688, 2010.

[89] Diana L Holmes and Nancy C Stellwagen. Estimation of polyacrylamide gel pore size from ferguson plots of normal and anomalously migrating dna fragments. i. gels containing 3% n, n'-methylenebisacrylamide. *Electrophoresis*, 12(4):253–263, 1991.

[90] Diana L Holmes and Nancy C Stellwagen. Estimation of polyacrylamide gel pore size from ferguson plots of linear dna fragments. ii. comparison of gels with different crosslinker concentrations, added agarose and added linear polyacrylamide. *Electrophoresis*, 12(9):612–619, 1991.

[91] Nancy C Stellwagen. Apparent pore size of polyacrylamide gels: Comparison of gels cast and run in tris-acetate-edta and tris-borate-edta buffers. *Electrophoresis*, 19(10):1542–1547, 1998.

[92] Lisa A Flanagan, Yo-El Ju, Beatrice Marg, Miriam Osterfield, and Paul A Janmey. Neurite branching on deformable substrates. *Neuroreport*, 13(18):2411, 2002.

[93] Bor-Sen Chiou, Robert J English, and Saad A Khan. Rheology and photo-cross-linking of thiol- ene polymers. *Macromolecules*, 29(16):5368–5374, 1996.

[94] Marcel JE Fischer. Amine coupling through edc/nhs: a practical approach. In *Surface plasmon resonance*, pages 55–73. Springer, 2010.

[95] Greg T Hermanson. *Bioconjugate techniques*. Academic press, 2013.

[96] Eric Y Liu, Sukwon Jung, and Hyunmin Yi. Improved protein conjugation with uniform, macroporous poly (acrylamide-co-acrylic acid) hydrogel microspheres via edc/nhs chemistry. *Langmuir*, 32(42):11043–11054, 2016.

[97] Hyuck Joon Kwon. Chondrogenesis on sulfonate-coated hydrogels is regulated by their mechanical properties. *Journal of the mechanical behavior of biomedical materials*, 17:337–346, 2013.

[98] Shinichi Nagashima, Sizutoshi Ando, Kimiko Makino, Takeyo Tsukamoto, and Hiroyuki Ohshima. Size dependence of polymer composition in the surface layer of poly (acrylamide-co-acrylic acid) hydrogel microspheres. *Journal of colloid and interface science*, 197(2):377–382, 1998.

[99] Molecular Probes Inc. Working with fluospheres® fluorescent microspheres. technical report. 2004.

[100] Ricardo Serrano, Aereas Aung, Yi-Ting Yeh, Shyni Varghese, Juan C Lasheras, and Juan C del Álamo. Three-dimensional monolayer stress microscopy. *Biophysical journal*, 2019.

[101] Effie E Bastounis, Fabian E Ortega, Ricardo Serrano, and Julie A Theriot. A multiwell format polyacrylamide-based assay for studying the effect of extracellular matrix stiffness on the bacterial infection of adherent cells. *JoVE (Journal of Visualized Experiments)*, (137):e57361, 2018.

[102] Y Yeh, D E Skinner, B M Suzuki, N Youjeong, J H McKerrow, E Criado-Hidalgo, S Zhang, J C del Alamo, and C R Caffrey. Biomechanical interactions of schistosoma mansoni eggs with vascular endothelial cells. *In preparation.*

[103] Shun Zhang, Danielle Skinner, Prateek Joshi, Ernesto Criado-Hidalgo, Yi-Ting Yeh, Juan C Lasheras, Conor R Caffrey, and Juan C del Alamo. Quantifying the mechanics of locomotion of the schistosome pathogen with respect to changes in its physical environment. *Journal of the Royal Society Interface*, 16(150):20180675, 2019.

[104] MJ Doenhoff, O Hassounah, H Murare, J Bain, and S Lucas. The schistosome egg granuloma: immunopathology in the cause of host protection or parasite survival? *Transactions of the Royal Society of Tropical Medicine and Hygiene*, 80(4):503–514, 1986.

[105] Christian Schwartz and Padraic G Fallon. Schistosoma "eggs-iting" the host: granuloma formation and egg excretion. *Frontiers in immunology*, 9, 2018.

[106] Edward J Pearce and Andrew S MacDonald. The immunobiology of schistosomiasis. *Nature Reviews Immunology*, 2(7):499, 2002.

[107] Bruno Gryseels, Katja Polman, Jan Clerinx, and Luc Kestens. Human schistosomiasis. *The lancet*, 368(9541):1106–1118, 2006.

[108] Daniel G Colley, Amaya L Bustinduy, W Evan Secor, and Charles H King. Human schistosomiasis. *The Lancet*, 383(9936):2253–2264, 2014.

[109] Jian Zhang, Neil Chada, and Cynthia A Reinhart-King. Microscale interrogation of 3d tissue mechanics. *Frontiers in Bioengineering and Biotechnology*, 7:412, 2019.

[110] ME Dolega, Morgan Delarue, François Ingremeau, Jacques Prost, Antoine Delon, and Giovanni Cappello. Cell-like pressure sensors reveal increase of mechanical stress towards the core of multicellular spheroids under compression. *Nature communications*, 8:14056, 2017.

[111] Wontae Lee, Nikita Kalashnikov, Stephanie Mok, Ruba Halaoui, Elena Kuzmin, Andrew J Putnam, Shuichi Takayama, Morag Park, Luke McCaffrey, Ruogang Zhao, Richard L. Leask, and Christopher Moraes. Dispersible hydrogel force sensors reveal patterns of solid mechanical stress in multicellular spheroid cultures. *Nature communications*, 10(1):144, 2019.

[112] Otger Campas. A toolbox to explore the mechanics of living embryonic tissues. In *Seminars in cell & developmental biology*, volume 55, pages 119–130. Elsevier, 2016.

[113] Kuen Yong Lee and David J Mooney. Alginate: properties and biomedical applications. *Progress in polymer science*, 37(1):106–126, 2012.

[114] Jens W Neubauer, Nicolas Hauck, Max J Maännel, Maximilian Seuss, Andreas Fery, and Julian Thiele. Mechanoresponsive hydrogel particles as a platform for three-dimensional force sensing. *ACS applied materials & interfaces*, 11(29):26307–26313, 2019.

[115] Hyun Joon Kong, Thomas R Polte, Eben Alsberg, and David J Mooney. Fret measurements of cell-traction forces and nano-scale clustering of adhesion ligands varied by substrate stiffness. *Proceedings of the National Academy of Sciences*, 102(12):4300–4305, 2005.

[116] Shinzo Omi, Ken'ichi Katami, Arihiro Yamamoto, and Mamoru Iso. Synthesis of polymeric microspheres employing spg emulsification technique. *Journal of applied polymer science*, 51(1):1–11, 1994.

[117] Ignacio Rintoul and Christine Wandrey. Polymerization of ionic monomers in polar solvents: kinetics and mechanism of the free radical copolymerization of acrylamide/acrylic acid. *Polymer*, 46(13):4525–4532, 2005.

[118] Takasi Nisisako, Toru Torii, and Toshiro Higuchi. Droplet formation in a microchannel network. *Lab on a Chip*, 2(1):24–26, 2002.

[119] Christophe Clanet and Juan C Lasheras. Transition from dripping to jetting. *Journal of fluid mechanics*, 383:307–326, 1999.

[120] Taotao Fu, Yining Wu, Youguang Ma, and Huai Z Li. Droplet formation and breakup dynamics in microfluidic flow-focusing devices: from dripping to jetting. *Chemical engineering science*, 84:207–217, 2012.

[121] M De Menech, Piotr Garstecki, F Jousse, and Howard A Stone. Transition from squeezing to dripping in a microfluidic t-shaped junction. *journal of fluid mechanics*, 595:141–161, 2008.

[122] Jian Hong Xu, SW Li, Jing Tan, and GS Luo. Correlations of droplet formation in t-junction microfluidic devices: from squeezing to dripping. *Microfluidics and Nanofluidics*, 5(6):711–717, 2008.

[123] JH Xu, GS Luo, SW Li, and GG Chen. Shear force induced monodisperse droplet formation in a microfluidic device by controlling wetting properties. *Lab on a Chip*, 6(1):131–136, 2006.

[124] Piotr Garstecki, Michael J Fuerstman, Howard A Stone, and George M Whitesides. Formation of droplets and bubbles in a microfluidic t-junction—scaling and mechanism of break-up. *Lab on a Chip*, 6(3):437–446, 2006.

[125] Thomas Cubaud and Thomas G Mason. Capillary threads and viscous droplets in square microchannels. *Physics of Fluids*, 20(5):053302, 2008.

[126] Haihu Liu and Yonghao Zhang. Droplet formation in microfluidic cross-junctions. *Physics of Fluids*, 23(8):082101, 2011.

[127] Enas M Ahmed. Hydrogel: Preparation, characterization, and applications: A review. *Journal of advanced research*, 6(2):105–121, 2015.

[128] Kytai Truong Nguyen and Jennifer L West. Photopolymerizable hydrogels for tissue engineering applications. *Biomaterials*, 23(22):4307–4314, 2002.

[129] Karen L Christman, Andrew J Vardanian, Qizhi Fang, Richard E Sievers, Hubert H Fok, and Randall J Lee. Injectable fibrin scaffold improves cell transplant survival, reduces infarct expansion, and induces neovasculature formation in ischemic myocardium. *Journal of the American College of Cardiology*, 44(3):654–660, 2004.

[130] Karen L Christman. Biomaterials for tissue repair. *Science*, 363(6425):340–341, 2019.

[131] Brenda K Mann, Andrea S Gobin, Annabel T Tsai, Rachael H Schmedlen, and Jennifer L West. Smooth muscle cell growth in photopolymerized hydrogels with cell adhesive and proteolytically degradable domains: synthetic ecm analogs for tissue engineering. *Biomaterials*, 22(22):3045–3051, 2001.

[132] Ewa Andrzejewska. Photopolymerization kinetics of multifunctional monomers. *Progress in polymer science*, 26(4):605–665, 2001.

[133] Natalja E Fedorovich, Marion H Oudshoorn, Daphne van Geemen, Wim E Hennink, Jacqueline Alblas, and Wouter JA Dhert. The effect of photopolymerization on stem cells embedded in hydrogels. *Biomaterials*, 30(3):344–353, 2009.

[134] Ricardo Serrano, Wesley Lawrence McKeithan, Mark Mercola, and Juan Carlos del Álamo. High-throughput functional screening assay of force and stiffness in ipsc derived cardiomyocytes. *Biophysical Journal*, 114(3):312a, 2018.

[135] James Sangster. *Octanol-water partition coefficients: fundamentals and physical chemistry*, volume 1. John Wiley & Sons, 1997.

[136] José Luis Aparicio and María Elizalde. Migration of photoinitiators in food packaging: a review. *Packaging Technology and Science*, 28(3):181–203, 2015.

[137] Ana Sanches-Silva, Catarina Andre, Isabel Castanheira, José Manuel Cruz, Sarah Pastorelli, Catherine Simoneau, and Perfecto Paseiro-Losada. Study of the migration of photoinitiators used in printed food-packaging materials into food simulants. *Journal of agricultural and food chemistry*, 57(20):9516–9523, 2009.

[138] Amol A Pawar, Gabriel Saada, Ido Cooperstein, Liraz Larush, Joshua A Jackman, Seyed R Tabaei, Nam-Joon Cho, and Shlomo Magdassi. High-performance 3d printing of hydrogels by water-dispersible photoinitiator nanoparticles. *Science advances*, 2(4):e1501381, 2016.

[139] Oliver Otto, Philipp Rosendahl, Alexander Mietke, Stefan Golfier, Christoph Herold, Daniel Klaue, Salvatore Girardo, Stefano Pagliara, Andrew Ekpenyong, Angela Jacobi, Manja Wobus, Nicole Topfner, Ulrich F Keyser, Jorg Mansfeld, Elisabeth Fisher-Friedrick, and Jochen Guck. Real-time deformability cytometry: on-the-fly cell mechanical phenotyping. *Nature methods*, 12(3):199, 2015.

[140] Z Ilke Kalcioglu, Roza Mahmoodian, Yuhang Hu, Zhigang Suo, and Krystyn J Van Vliet. From macro-to microscale poroelastic characterization of polymeric hydrogels via indentation. *Soft Matter*, 8(12):3393–3398, 2012.

[141] Ernesto Criado-Hidalgo, Antoni Garcia-Herreros, Yi-Ting Yeh, Juan Lasheras, and Juan Carlos Del Alamo. A capillary controlled hydrogel microchannel for isotropic compressive stress quantification. *In Preparation*, 2020.

[142] Matthew G Ondeck and Adam J Engler. Mechanical characterization of a dynamic and tunable methacrylated hyaluronic acid hydrogel. *Journal of biomechanical engineering*, 138(2):021003, 2016.

[143] Steven R Caliari, Maryna Perepelyuk, Brian D Cosgrove, Shannon J Tsai, Gi Yun Lee, Robert L Mauck, Rebecca G Wells, and Jason A Burdick. Stiffening hydrogels for investigating the dynamics of hepatic stellate cell mechanotransduction during myofibroblast activation. *Scientific reports*, 6:21387, 2016.

[144] Manouk Abkarian and Annie Viallat. *Chapter 10. On the Importance of the Deformability of Red Blood Cells in Blood Flow*. The Royal Society of Chemistry, 2016.

[145] Ernest Beutler and Jill Waalen. The definition of anemia: what is the lower limit of normal of the blood hemoglobin concentration? *Blood*, 107(5):1747–1750, 2006.

[146] He Li, Lu Lu, Xuejin Li, Pierre A Buffet, Ming Dao, George E Karniadakis, and Subra Suresh. Mechanics of diseased red blood cells in human spleen and consequences for hereditary blood disorders. *Proceedings of the National Academy of Sciences of the United States of America*, 115(38):9574–9579, September 2018.

[147] Aleksander S Popel and Paul C Johnson. Microcirculation and Hemorheology. *Annual Review of Fluid Mechanics*, 37(1):43–69, January 2005.

[148] S Majid Hosseini and James J Feng. How malaria parasites reduce the deformability of infected red blood cells. *Biophysical journal*, 103(1):1–10, 2012.

[149] Reina E Mebius and Georg Kraal. Structure and function of the spleen. *Nature reviews immunology*, 5(8):606, 2005.

[150] Igor V Pivkin, Zhangli Peng, George E Karniadakis, Pierre A Buffet, Ming Dao, and Subra Suresh. Biomechanics of red blood cells in human spleen and consequences for physiology and disease. *Proceedings of the National Academy of Sciences of the United States of America*, 113(28):7804–7809, July 2016.

[151] Antoni Garcia-Herreros and Juan Carlos Del Alamo. In vitro characterization of red blood cell transmigration through splenic inter-endothelial slits. *In Preparation*, 2020.

[152] Dhananjay Dendukuri, Daniel C Pregibon, Jesse Collins, T Alan Hatton, and Patrick S Doyle. Continuous-flow lithography for high-throughput microparticle synthesis. *Nature materials*, 5(5):365, 2006.

[153] Priya Gambhire, Scott Atwell, Cécile Iss, Frédéric Bedu, Igor Ozerov, Catherine Badens, Emmanuèle Helfer, Annie Viallat, and Anne Charrier. High Aspect Ratio Sub-Micrometer Channels Using Wet Etching: Application to the Dynamics of Red Blood Cell Transiting through Biomimetic Splenic Slits. *Small*, 13(32):1700967–11, June 2017.

[154] Denis English and Burton R Andersen. Single-step separation of red blood cells, granulocytes and mononuclear leukocytes on discontinuous density gradients of ficoll-hypaque. *Journal of immunological methods*, 5(3):249–252, 1974.

[155] Gian Maria D'Amici, Cristiana Mirasole, Angelo D'Alessandro, Tatsuro Yoshida, Larry J Dumont, and Lello Zolla. Red blood cell storage in sagm and as3: a comparison

through the membrane two-dimensional electrophoresis proteome. *Blood Transfusion*, 10(Suppl 2):s46, 2012.

[156] Anne J Ridley, Martin A Schwartz, Keith Burridge, Richard A Firtel, Mark H Ginsberg, Gary Borisy, J Thomas Parsons, and Alan Rick Horwitz. Cell migration: integrating signals from front to back. *Science*, 302(5651):1704–1709, 2003.

[157] Hideki Yamaguchi, Jeffrey Wyckoff, and John Condeelis. Cell migration in tumors. *Current opinion in cell biology*, 17(5):559–564, 2005.

[158] Tim Lämmermann, Bernhard L Bader, Susan J Monkley, Tim Worbs, Roland Wedlich-Söldner, Karin Hirsch, Markus Keller, Reinhold Förster, David R Critchley, Reinhard Fässler, David R. Critchley, Reinhard Fassler, and Michael Sixt. Rapid leukocyte migration by integrin-independent flowing and squeezing. *Nature*, 453(7191):51, 2008.

[159] Peter Friedl. Prespecification and plasticity: shifting mechanisms of cell migration. *Current opinion in cell biology*, 16(1):14–23, 2004.

[160] Denis Wirtz, Konstantinos Konstantopoulos, and Peter C Searson. The physics of cancer: the role of physical interactions and mechanical forces in metastasis. *Nature Reviews Cancer*, 11(7):512, 2011.

[161] Joe Swift and Dennis E Discher. The nuclear lamina is mechano-responsive to ecm elasticity in mature tissue. *J Cell Sci*, 127(14):3005–3015, 2014.

[162] Jerome Irianto, Yuntao Xia, Charlotte R Pfeifer, Avathamsa Athirasala, Jiazheng Ji, Cory Alvey, Manu Tewari, Rachel R Bennett, Shane M Harding, Andrea J Liu, Roger A Greenber, and Dennis Discher. Dna damage follows repair factor depletion and portends genome variation in cancer cells after pore migration. *Current Biology*, 27(2):210–223, 2017.

[163] Steven W Edwards. *Biochemistry and Physiology of the Neutrophil*. Cambridge University Press, 2005.

[164] Ruslan Natanov, Faikah Gueler, Christine S Falk, Christian Kühn, Ulrich Maus, Erin C Boyle, Thierry Siemeni, Ann-Katrin Knoefel, Serghei Cebotari, Axel Haverich, and Nodir Madrahimov. Blood cytokine expression correlates with early multi-organ damage in a mouse model of moderate hypothermia with circulatory arrest using cardiopulmonary bypass. *PloS one*, 13(10):e0205437, 2018.

[165] Rianne M Jongman, Jan G Zijlstra, Wendelinde F Kok, Annemarie E van Harten, Massimo A Mariani, Jill Moser, Michel MRF Struys, Anthony R Absalom, Grietje Molema, Thomas WL Scheeren, and Matijs van Meurs. Off-pump cabg surgery reduces

systemic inflammation compared with on-pump surgery but does not change systemic endothelial responses: a prospective randomized study. *Shock*, 42(2):121–128, 2014.

[166] Warren L Lee and Gregory P Downey. Neutrophil activation and acute lung injury. *Current opinion in critical care*, 7(1):1–7, 2001.

[167] Herbert H Lipowsky. Shear stress in the circulation. In *Flow-dependent regulation of vascular function*, pages 28–45. Springer, 1995.

[168] Leen Vercaemst. Hemolysis in cardiac surgery patients undergoing cardiopulmonary bypass: a review in search of a treatment algorithm. *The Journal of extra-corporeal technology*, 40(4):257, 2008.

[169] Xiaojie Wu, Molly A Newbold, and Christy L Haynes. Recapitulation of in vivo-like neutrophil transendothelial migration using a microfluidic platform. *Analyst*, 140(15):5055–5064, 2015.

[170] Jonathan B Freund. The flow of red blood cells through a narrow spleen-like slit. *Physics of Fluids*, 25(11):110807, 2013.

[171] LG Rigat-Brugarolas, A Elizalde-Torrent, M Bernabeu, M De Niz, L Martin-Jaular, C Fernandez-Becerra, A Homs-Corbera, J Samitier, and HA Del Portillo. A functional microengineered model of the human splenon-on-a-chip. *Lab on a Chip*, 14(10):1715–1724, 2014.

[172] Julien Picot, Papa Alioune Ndour, Sophie D Lefevre, Wassim El Nemer, Harvey Tawfik, Julie Galimand, Lydie Da Costa, Jean-Antoine Ribeil, Mariane de Montalembert, Valentine Brousse, Bruno Le Pioufle, Pierre Buffet, Caroline Le Van Kim, and Olivier Français. A biomimetic microfluidic chip to study the circulation and mechanical retention of red blood cells in the spleen. *American Journal of Hematology*, 90(4):339–345, February 2015.

[173] Detlev Drenckhahn and Joachim Wagner. Stress fibers in the splenic sinus endothelium in situ: molecular structure, relationship to the extracellular matrix, and contractility. *The Journal of cell biology*, 102(5):1738–1747, 1986.

[174] Allison K O'Brien and Christopher N Bowman. Impact of oxygen on photopolymerization kinetics and polymer structure. *Macromolecules*, 39(7):2501–2506, 2006.

[175] Zhigang Wu and Klas Hjort. Surface modification of pdms by gradient-induced migration of embedded pluronic. *Lab on a Chip*, 9(11):1500–1503, 2009.

[176] Bingzhao Xia, Kaspars Krutkramelis, and John Oakey. Oxygen-purged microfluidic device to enhance cell viability in photopolymerized peg hydrogel microparticles. *Biomacromolecules*, 17(7):2459–2465, 2016.

[177] ID Johnston, DK McCluskey, CKL Tan, and MC Tracey. Mechanical characterization of bulk sylgard 184 for microfluidics and microengineering. *Journal of Micromechanics and Microengineering*, 24(3):035017, 2014.

[178] Jeong-Yun Sun, Xuanhe Zhao, Widusha RK Illeperuma, Ovijit Chaudhuri, Kyu Hwan Oh, David J Mooney, Joost J Vlassak, and Zhigang Suo. Highly stretchable and tough hydrogels. *Nature*, 489(7414):133, 2012.

[179] Hyunwoo Yuk, Teng Zhang, Shaoting Lin, German Alberto Parada, and Xuanhe Zhao. Tough bonding of hydrogels to diverse non-porous surfaces. *Nature materials*, 15(2):190, 2016.

[180] Hyunwoo Yuk, Teng Zhang, German Alberto Parada, Xinyue Liu, and Xuanhe Zhao. Skin-inspired hydrogel–elastomer hybrids with robust interfaces and functional microstructures. *Nature communications*, 7:12028, 2016.

[181] Shigeo Tazuke and Hitoshi Kimura. Surface photografting, 2. modification of polypropylene film surface by graft polymerization of acrylamide. *Die Makromolekulare Chemie: Macromolecular Chemistry and Physics*, 179(11):2603–2612, 1978.

[182] Yuli Wang, Hsuan-Hong Lai, Mark Bachman, Christopher E Sims, GP Li, and Nancy L Allbritton. Covalent micropatterning of poly (dimethylsiloxane) by photografting through a mask. *Analytical Chemistry*, 77(23):7539–7546, 2005.

[183] Dhananjay Dendukuri, Priyadarshi Panda, Ramin Haghgooie, Ju Min Kim, T Alan Hatton, and Patrick S Doyle. Modeling of oxygen-inhibited free radical photopolymerization in a pdms microfluidic device. *Macromolecules*, 41(22):8547–8556, 2008.

[184] Dmitry A Markov, Elizabeth M Lillie, Shawn P Garbett, and Lisa J McCawley. Variation in diffusion of gases through pdms due to plasma surface treatment and storage conditions. *Biomedical microdevices*, 16(1):91–96, 2014.

[185] Jinwen Zhou, Amanda Vera Ellis, and Nicolas Hans Voelcker. Recent developments in pdms surface modification for microfluidic devices. *Electrophoresis*, 31(1):2–16, 2010.

[186] Aslihan Gokaltun, Martin L Yarmush, Ayse Asatekin, and O Berk Usta. Recent advances in nonbiofouling pdms surface modification strategies applicable to microfluidic technology. *Technology*, 5(01):1–12, 2017.

[187] Jennifer L Bays, Hannah K Campbell, Christy Heidema, Michael Sebbagh, and Kris A DeMali. Linking e-cadherin mechanotransduction to cell metabolism through force-mediated activation of ampk. *Nature cell biology*, 19(6):724–731, 2017.

[188] Matthias Rübsam, Aaron F Mertz, Akiharu Kubo, Susanna Marg, Christian Jüngst, Gladiola Goranci-Buzhala, Astrid C Schauss, Valerie Horsley, Eric R Dufresne, Markus Moser, Wolfgang Zieglen, Masayuki Amagai, Sara A. Wickstrom, and Carien M. Niessen. E-cadherin integrates mechanotransduction and egfr signaling to control junctional tissue polarization and tight junction positioning. *Nature communications*, 8(1):1–16, 2017.